SYNTHESIS AND CHARACTERIZATION OF UNDOPED AND STRONTIUM-DOPED POTASSIUM SODIUM NIOBATE CERAMICS

Jitka Hreščak

Doctoral Dissertation
Jožef Stefan International Postgraduate School
Ljubljana, Slovenia

Supervisor: Asst. Prof. Dr. Andreja Benčan Golob, Jožef Stefan International Postgraduate School and Jožef Stefan Institute, Ljubljana, Slovenia
Co-Supervisor: Prof. Dr. Barbara Malič, Jožef Stefan International Postgraduate School and Jožef Stefan Institute, Ljubljana, Slovenia

Evaluation Board:
Asst. Prof. Dr. Goran Dražić, Chair, Jožef Stefan International Postgraduate School, Jožef Stefan Institute, and National Institute of Chemistry, Ljubljana, Slovenia
Asst. Prof. Dr. Boštjan Jančar, Member, Jožef Stefan International Postgraduate School, Jožef Stefan Institute, Ljubljana, Slovenia
Dr. Vincenzo Buscaglia, Member, Consiglio Nazionale della Ricerche,
Institute of Condensed Matter Chemistry and Energy Technologies, Genoa, Italy

MEDNARODNA PODIPLOMSKA ŠOLA JOŽEFA STEFANA
JOŽEF STEFAN INTERNATIONAL POSTGRADUATE SCHOOL



Jitka Hreščak

SYNTHESIS AND CHARACTERIZATION OF UNDOPED AND STRONTIUM-DOPED POTASSIUM SODIUM NIOBATE CERAMICS

Doctoral Dissertation

SINTEZA IN KARAKTERIZACIJA NEDOPIRANE IN S STRONCIJEM DOPIRANE KERAMIKE NA OSNOVI KALIJEVEGA NATRIJEVEGA NIOBATA

Doktorska disertacija

Supervisor: Asst. Prof. Dr. Andreja Benčan Golob

Co-Supervisor: Prof. Dr. Barbara Malič

Ljubljana, Slovenia, May 2016

Mamce.

Acknowledgments

Obviously, a doctoral thesis is hardly a work that can be created by a single person. Therefore, here, I would like to make a list – as complete as possible – of people who cooperated with me or in some way contributed to the work of which I am listed as the author.

The greatest influence on this thesis can definitely be attributed to my mentor Asst. Prof. Dr. Andreja Benčan Golob. Let me express at least the main aspects that make me very grateful to be her PhD student: I appreciate her for directing me out of many scientific tunnels without any light at the end, for driving me to improve my starting knowledge about the field in a respectful manner and most of all – for always being there for an effective discussion about Sr-doped KNN and for the fact that after our meetings, I would walk out of her office with huge motivation for further research.

I would also like to thank my co-mentor and department leader Prof. Dr. Barbara Malič for her amazing knowledge, which I admire, and which adds a respectable scientific touch to my work. I appreciate the time she dedicated for a careful critical judgment of this thesis and generally of my work, since every one of her comments taught me a lot.

It might seem too late, but also Prof. Dr. Marija Kosec in those too few discussions we got to have before she passed away in December 2012, she expressed the main ideas which were carved into my head and importantly shaped my future work and interpretation of the results in this thesis.

I highly appreciate the contribution of Asst. Prof. Dr. Goran Dražić for ARM analysis, Dr. Marco Deluca for the Raman analysis, Prof. Dr. Iztok Arčon with Prof. Dr. Alojzij Kodre for the EXAFS analysis and Prof. Dr. Monica Dapiaggi for the synchrotron XRD analysis with Rietveld refinement. Edi Kranjc is gratefully acknowledged for the measurement of countless XRD spectra. Many thanks go to Jena Cilenšek for the thermal analysis measurements, to Silvo Drnovšek for all kinds of support in the laboratory during the solid-state synthesis and to Brigita Kmet for the support during the TEM samples' preparation. Asst. Prof. Dr. Tadej Rojac is gratefully acknowledged for many useful discussions about all the analyses, procedures and results.

Special thanks go to Asst. Prof. Dr. Andreja Benčan Golob, Asst. Prof. Dr. Boštjan Jančar, Asst. Prof. Dr. Sašo Šturm and Asst. Prof. Dr. Goran Dražić for introducing me into the fascinating world of transmission electron microscopes and being always there for discussions.

This work would be done with a much greater delay if I did not have the support of Lucija Juvan and Nika Kurinčič for the samples' preparation. I would also like to thank Maja Makarovič together with Katarina Hočevar (nee Korenčan) who helped me with the samples in the absence of Lucija and Nika.

I would like to thank all my office-mates: first to Sebastjan Glinšek and Gregor Trefalt for answering my first and very basic questions about ceramics, later Tadej Rojac and Jurij Koruza for fruitful discussions on a slightly advanced level and finally Tanja Pečnik, Maja Makarovič and Lovro Fulanović for being inspiring and supporting company in the final stage.

Here, I would also like to thank the whole K5 department and all the people who made hese years here my second home!

I could start thanking my family, this would include thanking my mother, who brought me up with a vision that I will once be very educated, to Marko for struggling to be awake when I needed to order my Sr-doped KNN ideas in the middle of the night, Klara for bringing unconditioned joy into my life regardless of what is happening with the Sr-doped KNN and my grandma for her life wisdom which helps me to stay sane. Here, I will stop, because I will never be able to thank everybody. So I will thank to each and every person who will read this thesis, in case I forgot to mention you in the acknowledgment!

From the financial point of view, this work was supported by the Slovenian Research Agency, under grants P2-0105, P1-0112 and PR-03727. I would also like to acknowledge the European Synchrotron Radiation Facility (ESRF), Grenoble, France, for the provision of synchrotron radiation facilities on ID22 (project MA2315) and BM23 (project LS-2275) with financial support for some of the users.

Abstract

The research in the field of lead-free piezoelectric ceramics in the past two decades has attracted a lot of attention to the materials based on $K_{0.5}Na_{0.5}NbO_3$ (KNN). However, the processing of these materials proved to be difficult, with the unstable outcome of the solid-state synthesis from the point of view of microstructure and phase composition as well as difficult sintering. Despite these generally known issues, relatively few studies actually treat the KNN solid-state synthesis to gain better control over the reproducibility of the synthesis.

One of the methods to improve the sintering of KNN is doping with alkaline earth metals, out of which, doping with strontium (Sr) brought the best densities and most significantly improved the piezoelectric response of the KNN. This thesis therefore addresses the main problems with KNN – the solid-state synthesis reproducibility as well as more detailed research of the material, which was designed to improve the KNN's functional properties.

In the first part, the KNN solid-state synthesis of alkaline carbonates with Nb_2O_5 in its orthorhombic or monoclinic form was studied. The X-ray diffraction and electron microscopy techniques showed, that the choice of the particular Nb_2O_5 influences the course of the reaction, the homogeneity of the resulting $(K_xNa_{1-x})NbO_3$ solid solution and finally the sintering behaviour and microstructure of KNN. The Nb_2O_5 reagent is therefore defined as an important factor that significantly influences the reproducibility of the KNN solid-state synthesis.

In the second part, the effect of the Sr dopant on the solid-state synthesis of KNN is studied by thermal analysis and *in-situ* high-temperature X-ray diffraction. Sr was not found to have a significant influence on the course of the solid-state synthesis. On the other hand, the particle size distribution of the Nb_2O_5 reagent proved to be a crucial factor influencing the temperature interval of the KNN solid-state synthesis.

And finally, in the third part of this work, the influence of the Sr dopant on the KNN's crystal structure and microstructure is described. The combination of the extended X-ray absorption fine-structure analysis and X-ray diffraction techniques with Rietveld refinement, Raman spectroscopy and electron microscopy techniques, brings the following results: the local structure around the Sr atom is determined to be cubic perovskite and Sr is confirmed to substitute the A-site of the perovskite lattice. Sr was confirmed to be homogenously distributed in the KNN. The investigations in the highly doped samples on the atomic level suggest that the system tends to segregate the A-site vacancies in a secondary phase in order to release the chemical pressure. Together with an increasing lattice disorder and microstrain, these effects are correlated with the increasing number of low-angle grain boundaries, which finally limit the grain growth and then lead to a significant grain size decrease.

Povzetek

V zadnjih dvajsetih letih je bilo na področju raziskav piezoelektrične keramike brez svinca veliko pozornosti namenjene materialom na osnovi kalijevega natrijevega niobata ($K_{0.5}Na_{0.5}NbO_3$ - KNN). Vendar je priprava keramike KNN v trdnem stanju eksperimentalno zahtevna in lahko vodi do neželene mikrostrukture ter nastanka sekundarnih faz; problematično je tudi zgoščevanje keramike KNN. Le manjše število raziskav je bilo namenjeno podrobnemu razumevanju sinteze KNN v trdnem stanju ter s tem tudi boljši kontroli priprave KNN.

Ena izmed metod, ki izboljšuje zgoščevanje KNN-ja, je dopiranje z zemljoalkalijskimi kovinami, od katerih dopiranje s stroncijem (Sr) povzroča večje gostote in izboljšan piezoelektrični odziv keramike KNN. Z namenom, da bi bolje obvladali ključne sintezne korake pri pripravi keramike KNN in s tem tudi bolje kontrolirali funkcionalne lastnosti keramike, smo v doktorskem delu študirali sintezo, strukturo in mikrostrukturo tako nedopirane kot s Sr dopirane keramike KNN, obe pripravljeni s sintezo v trdnem stanju.

V prvem delu doktorskega dela smo preučevali potek sinteze KNN v trdnem stanju iz alkalijskih karbonatov in ortorombskega oziroma monoklinskega Nb_2O_5. Z rentgensko praškovno difrakcijo in elektronsko mikroskopijo smo pokazali, da Nb_2O_5 močno vpliva na homogenost trdne raztopine $K_xNa_{1-x}NbO_3$ ter posledično na zgoščevanje in mikrostrukturo keramike KNN. Dokazali smo torej, da kristalna struktura Nb_2O_5, kot reagent za sintezo KNN, pomembno vpliva na potek in s tem na ponovljivost sinteze KNN v trdnem stanju.

V drugem delu doktorskega dela smo s pomočjo metod termične analize in *in-situ* visokotemperaturne rentgenske analize študirali vpliv stroncija na potek sinteze KNN. Pokazali smo, da Sr na potek sinteze KNN v trdnem stanju nima pomembnejšega vpliva. Ključen parameter, ki vpliva na temperaturni režim sinteze KNN, je porazdelitev velikosti delcev reagenta Nb_2O_5.

V tretjem delu doktorata smo preučevali vpliv Sr na kristalno strukturo in mikrostrukturo KNN-ja. Z uporabo komplementarnih analitskih metod, kot so rentgenska absorpcijska metoda, rentgenska difrakcija, dopolnjena z Rietveldovo analizo, Ramanska spektroskopija ter elektronska mikroskopija, smo pokazali, da je lokalna struktura okrog Sr atoma na A mestih perovskitne strukture kubična in da je Sr enakomerno porazdeljen v matrici KNN-ja. S strukturnimi raziskavami na atomskem nivoju smo ugotovili, da se v visoko dopirani keramiki KNN tvori sekundarna faza, v kateri se segregirajo kationske vrzeli, ki nastanejo kot posledica dopiranja KNN s Sr. Prav tako smo pokazali, da v keramiki KNN z naraščanjem količine Sr narašča tudi delež nizkokotnih mej med zrni, kar vpliva na rast zrn in povzroča izrazito zmanjšanje zrn v keramiki KNN.

Contents

1.2.1.1 Reaction mechanism during solid-state synthesis 3
1.2.1.2 Influence of reagents on the solid-state synthesis..... 4
1.2.3.1 Phase transitions 8
1.3.2.1 Doping KNN with Sr 15
4.1.1.1 K_2CO_3 and Na_2CO_3 reagents..... 27
4.1.1.2 Nb_2O_5 reagents 30
4.1.2.1 Reaction curves 35
4.1.2.2 Thermal analysis..... 36
4.1.2.3 Annealing of the homogenized mixtures 38

List of Figures

Figure 1.1: Publications on lead-free materials. 2
Figure 1.2: Reaction scheme. 3
Figure 1.3: Thermal analysis curves. 4
Figure 1.4: DTG curves of the K_2CO_3, Na_2CO_3 and Nb_2O_5 homogenized mixtures with different $d50$. 6
Figure 1.5: Nb_2O_5 polymorphs. 6
Figure 1.6: KNN sintering curve. 7
Figure 1.7: KNN microstructure 7
Figure 1.8: The relationship between orthorhombic and monoclinic $K_xNa_{1-x}NbO_3$ (x = 0.4-0.6) unit cells. 8
Figure 1.9: The phase transitions in KNN. 9
Figure 1.10: Rhombohedral nanoclusters. 9
Figure 1.11: Doping classification. 10
Figure 1.12: Lattice parameters in La-doped $BaTiO_3$. 11
Figure 1.13: Changes of Tc and To/t in doped $BaTiO_3$ 11
Figure 1.14: TEM micrograph of $BaTiO_3$ doped with 1.5 at% La with a typical core-shell structure. 12
Figure 1.15: La/PZT diffusion couple. 13
Figure 1.16: Sr-doped KNN unit cell. 15
Figure 1.17: Effects of Sr on KNN by Malič et al. 16
Figure 3.1: Temperature program for calcination. 20
Figure 3.2: Temperature program for sintering. 21
Figure 3.3: Temperature program for thermal analysis. 22
Figure 4.1: XRD spectra of K_2CO_3 before and after milling. 28
Figure 4.2: XRD spectra of Na_2CO_3 before and after milling. 29
Figure 4.3: K_2CO_3 and Na_2CO_3 powders. 29
Figure 4.4: XRD patterns of the as-received Nb_2O_5 reagents from two different producers. 30
Figure 4.5: The as-received Nb_2O_5 reagents. 31
Figure 4.6: The Nb_2O_5 reagents before and after milling. 31
Figure 4.7: XRD patterns of Nb_2O_5 reagents. 32
Figure 4.8: TEM of the milled Nb_2O_5 reagents. 33
Figure 4.9: HRTEM image of the milled Nb_2O_5-mono. 34
Figure 4.10: Reaction curves. 35
Figure 4.11: TG, DTG and DTA curves of the homogenized KNN-ortho and KNN-mono. 37
Figure 4.12: The XRD patterns of the homogenized KNN-ortho and -mono annealed to 400-700°C. 39
Figure 4.13: XRD patterns of the calcined KNN-ortho and –mono. 39
Figure 4.14: XRD spectra of the calcined KNN-mono annealed at 950°C, 4 h. 40
Figure 4.15: XRD spectra of the milled Nb_2O_5-mono, annealed at 400-850°C. 41
Figure 4.16: Sintering curves. 43
Figure 4.17: SEM micrographs of the sintered samples. 44
Figure 4.18: Calcined KNN-ortho and calcined KNN-mono-950 powders. 45
Figure 4.19: TG and DTG of KNN-ortho, KNN-1% Sr, KNN-2% Sr, KNN-6% Sr and KNN-nm in the temperature interval 200–750°C. 47
Figure 4.20: TG, DTG, DTA and EGA of the KNN-1% Sr in the temperature interval from RT to 750°C. 48

Figure 4.21: Particles morphology and particle size distribution of the homogenized mixtures. 51
Figure 4.22: Particle size distribution of the Nb_2O_5 used for synthesis in the particular sample. 52
Figure 4.23: DTA of the KNN-ortho, KNN-1% Sr, KNN-2% Sr, KNN-6% Sr, KNN-nm. 53
Figure 4.24: In-situ HT-XRD spectra of the KNN-nm, KNN-1% Sr, KNN-2% Sr and KNN-6% Sr. .. 54
Figure 4.25: Enlarged in-situ HT-XRD spectra of the KNN-6% Sr sample. 55
Figure 4.26: XRD of the ceramic powders after the first calcination. 56
Figure 4.27: XRD spectra of the samples. 58
Figure 4.28: Synchrotron XRD spectra of the samples. 59
Figure 4.29: SEM micrographs of the KNN, KNN-0.5% Sr, KNN-1% Sr, KNN-2% Sr, KNN-6% Sr-1140 and KNN-8% Sr-1140. 62
Figure 4.30: TEM micrographs of the KNN, KNN-2% Sr and KNN-6% Sr. 62
Figure 4.31: Structural and microstructural changes in KNN with increasing Sr-content. 63
Figure 4.32: EDXS spectra of the matrix and secondary phase in KNN-6% Sr-1140. 64
Figure 4.33: TEM micrograph of the KNN-6% Sr-1140. 65
Figure 4.34:Raman spectra measured at 80 K for KNN, KNN-0.5% Sr, KNN-2% Sr, KNN-8% Sr. 66
Figure 4.35:Temperature-dependent Raman spectra for KNN, KNN-2% Sr and KNN-8% Sr. 67
Figure 4.36: EXAFS analysis of the KNN, KNN-0.5% Sr and KNN-2% Sr. 69
Figure 4.37: TEM-EDXS of KNN-1% Sr and KNN-2% Sr. 71
Figure 4.38: Line-scan analysis of KNN-6% Sr. 72
Figure 4.39: HRTEM micrographs of the KNN-2% Sr and KNN-6% Sr 73
Figure 4.40: ARM study of a grain boundary in KNN-6% Sr 73
Figure 4.41: TEM study of a grain boundary in KNN-6% Sr-1140 74
Figure 4.42: HAADF-STEM micrograph of a grain boundary in KNN-6% Sr. 74
Figure 4.43: HRTEM micrograph of subgrains in KNN-6% Sr-1140. 75
Figure 4.44: ARM study of a grain boundary in KNN-8% Sr-1140 77

List of Tables

Table 1.1: Literature review on single element KNN dopants. The list is completed with the kind of doping used, based on the reported formula. GS – grain size, AGG – abnormal grain growth, ↑ increase, ↓ decrease, ~ comparable, compared to KNN. TC - ferroelectric Currie temperature, ε - dielectric permittivity, tanδ - dielectric losses, $d33$ – piezoelectric coefficient, planar (kp) and thickness (kt) mechanical coupling factors. 14
Table 3.1: List of chemicals and accessories. A detailed description of the chemicals and accessories mentioned in the Materials and Methods section are listed in alphabetical order according to the item name. 19
Table 4.1: Summary of some TG, DTG and DTA values for homogenized KNN-ortho and homogenized KNN-mono. 38
Table 4.2: Densities of the sintered ceramics. 43
Table 4.3: Theoretical and actual mass losses of KNN-ortho, KNN-1% Sr, KNN-2% Sr, KNN-6% Sr and KNN-nm. 48
Table 4.4: Unit cell parameters of the Sr-doped KNN samples. The values are obtained with the Rietveld refinement of the XRD spectra from Figure 4.27, using the monoclinic unit cell [32]. The Rwp factor marks the quality of the fit. 58
Table 4.5: Rietveld refinement of the synchrotron XRD data. Table sumarizes the used structure and model as well as results of the crystallite size and microstrain, complemented with the Rwp factor describing the quality of the fit. 59
Table 4.6: Results of the EXAFS model. The common parameters of the nearest coordination shells around Sr atom in all KNN-0.5% Sr, KNN-1% Sr and KNN-2% Sr samples: atomic species, coordination number N, distance r and Debye-Waller factor $\sigma 2$. The uncertainty of the last digit of r is given in parentheses. 68
Table 4.7: Results from the SEM-WDXS analysis. 69

Abbreviations

ABF . . . annular bright-field
AGG . . . abnormal grain growth
BSE . . . backscattered electrons retractable detector
C . . . cubic
DTA . . . differential thermal analysis
EDXS . . . energy-dispersive X-ray spectroscopy
EGA . . . evolved-gas analysis
EXAFS . . . extended X-ray absorption fine structure
FFT . . . fast Fourier transform
GS . . . grain size
HAADF . . . high-angle annular dark-field
HRTEM . . . high-resolution TEM
HT-XRD . . . *in-situ* high-temperature X-ray diffraction
KNN . . . $K_{0.5}Na_{0.5}NbO_3$
LEI . . . low-energy secondary electrons in-lens detector
M . . . monoclinic
PZT . . . $PbZr_xTi_{(1-x)}O_3$
R . . . rhombohedral
SEI . . . secondary electrons in-lens detector
SEM . . . scanning electron microscope
SSA . . . specific surface area
STEM . . . scanning transmission electron microscopy
synchrotron XRD . . . synchrotron X-ray diffraction
T . . . tetragonal
TD . . . theoretical density
TEM . . . transmission electron microscopy
TG . . . thermogravimetry
WDXS . . . wavelength-dispersive X-ray spectroscopy
XRD . . . X-ray diffraction

Symbols

CTE ... linear coefficient of thermal expansion
d_{10}, d_{50}, d_{90} ... particle sizes reached by 10 %, 50 %, and 90 % of the particles; obtained from the area particle-size distributions
d_{33} ... piezoelectric coefficient
d_{BET} ... BET equivalent particle diameter
I_{i0} ... experimental intensity
I_{iC} ... calculated intensity
k ... wavevector
k_p ... planar electromechanical coupling factor
k_t ... thickness electromechanical coupling factor
l_{RT} ... initial dimension of the sample at RT
l_T ... dimension of the sample at the selected temperature
M ... molecular weight
m_1 ... mass of the sintered pellet before the measurement
m_2 ... the mass of the pellet in the water
m_3 ... mass of the pellet after it was taken out of water
N ... coordination numbers
r ... radius of the sphere
R ... radius of the shell
RT ... room temperature
R_{wp} ... weighted profile residual factor
S_0^2 ... amplitude reduction factor
S_M ... specific surface area
T ... temperature
$\tan\delta$ ... dielectric losses
T_C ... ferroelectric Currie temperature
T_c ... temperature of the phase transition to cubic phase
T_{FIN} ... end of the reaction
$T_{o/t}$ ... temperature of the phase transition from orthorhombic to tetragonal phase
V_M ... molar volume
$(\Delta l/l)_{tech}$ ... technical shrinkage
ΔE_0 ... photoelectron zero-energy
$\Delta l/l$ ... relative (physical) shrinkage
ε ... dielectric constant
ν_{1-5} ... Raman modes
ρ ... density
ρ_{H2O} ... density of the distilled water at a given temperature
ρ_{abs}^t ... absolute theoretical density
Σ ... the number of lattice points in a unit cell of the lattice being generated sigma
σ^2 ... Debye–Waller factor
ψ_A/ψ_V ... particle shape factor ratio

Chapter 1

Introduction

1.1 Piezoelectric Ceramics

In past decades we have been seeing a fascinating trend towards the miniaturization of electronic devices. This miniaturization could hardly be feasible without special materials, that have the ability to convert mechanical energy into electric energy and *vice versa*, on the nanoscale. Such behaviour is possible thanks to the piezoelectric effect.

The direct piezoelectric effect is that a material subjected to mechanical stress, generates an electric charge proportional to the stress. The converse piezoelectric effect is when the material becomes strained upon the application of an electric field, the strain again being proportional to the applied field.

Piezoelectric materials are used in many applications, the most known being the piezoelectric lighter, but also, for example, the knock sensor or airbag acceleration sensor in automotive applications, position actuator or piezoelectric motor in atomic force and electron microscopes, acoustic transducers used for ultrasonic cleaning, welding or mixing, ultrasonic sensors used in sonar applications for detecting objects [1]. This makes piezoelectric materials important for progress in technology and is reflected in worldwide sales of $18 billion in 2013 [2].

Because of their excellent piezoelectric and ferroelectric properties, the lead-based ceramics such as $PbZr_xTi_{(1-x)}O_3$ (PZT) have been dominating the piezoelectric applications so far [2]. However, due to the high toxicity of the lead present in these materials, in 2003 the European Union included PZT on a list of hazardous substances that would have to be replaced [3, 4]. The increasingly restricting legislation after 2003, has stimulated an intense research on finding a lead-free substitute, as is visible from the graph showing the number of publications on lead-free materials in Figure 1.1 [5].

In 2004, Saito et al. [6] reported on a lead-free piezoelectric ceramic with piezoelectric constants approaching the ones of PZT. This material was a solid-solution of potassium sodium niobate ceramic with $LiNbO_3$, $LiTaO_3$ and $LiSbO_3$. As seen in Figure 1.1, this report caused a steep increase of interest in the alkaline-niobium-based materials. Although there has been a large effort to find a suitable material, after more than 10 years of an intense research, the PZT still overcomes the possible lead-free candidates in performance and ease of preparation. Nevertheless, besides novel and often expensive preparation methods, doping or chemical modification of the already known lead-free materials remains the most convenient way to improve their properties.

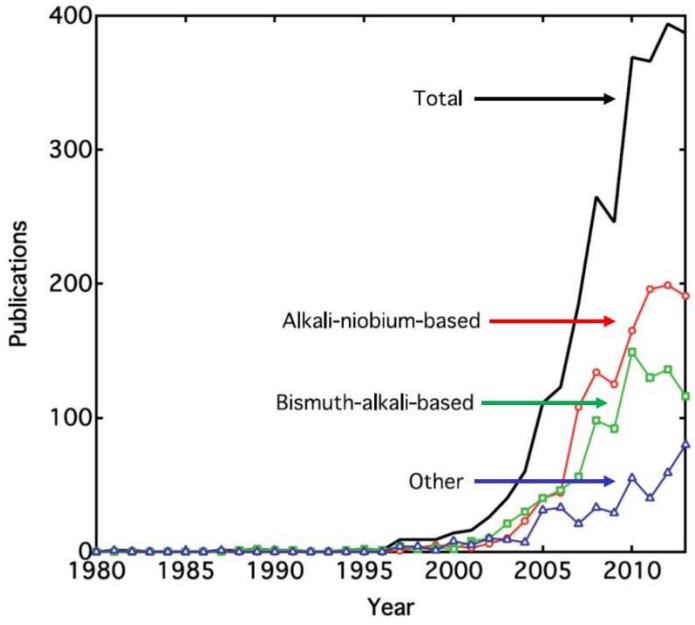


Figure 1.1: Publications on lead-free materials. Increase of the annual refereed publications on lead-free materials during past decades, divided into alkali-niobium-based and bismuth-alkali-based ceramics as well as others. Redrawn after Rödel et al. [5].

1.2 Lead-Free Piezoelectric Ceramics $K_{0.5}Na_{0.5}NbO_3$

Owing to Saito's discovery [6], the potassium sodium niobate solid solution-based materials with a morphotropic phase boundary believed to be around the composition $K_{0.5}Na_{0.5}NbO_3$ (KNN) [7] became one of the most studied lead-free materials. However, KNN was reported to be ferroelectric already in 1954 by Shirane et al. [8] and its remarkable piezoelectric properties attracted attention after the report by Egerton and Dillon in 1959 [9]. KNN has a high Curie temperature (T_C = 420°C) [8, 9], a relatively moderate piezoelectric coefficient d_{33}, usually reported between 100 and 120 pC/N [9-11], a high planar electromechanical coupling factor (k_p = 33–40 %) [9-11] and a low dielectric constant ε = 430–472 [9, 10].

Despite their promising electrical properties, KNN-based piezoelectrics are still not widely used in industrial products. The KNN-based ceramics would be perfectly able to compete with their existing lead counterparts in certain applications; however, PZT still holds the pole position in terms of ease of preparation and engineering. The main drawbacks of KNN are processing related.

The densification of stoichiometric KNN is characterized by the extremely narrow sintering interval, i.e., between 1100 and 1140°C, which is close to the solidus temperature [12]. In addition, the reproducibility of the solid-state synthesis is still an issue, based on different authors reporting a variety of properties and different microstructures for KNN products prepared using comparable procedures [10, 13, 14].

1.2.1 Solid-state synthesis

Solid-state synthesis, being a reaction that leads to the formation of a compound, is dependent on the diffusion rate via the reaction layer that separates the reagents [15].

The following part gives a literature review of the mechanism for KNN solid-state synthesis.

1.2.1.1 Reaction mechanism during solid-state synthesis

KNN is typically formed via the reaction of potassium and sodium carbonates and niobium oxide during the solid-state synthesis. As the carbonates decompose upon heating, the CO_2 gas is evolving from the system as a side product. The reaction of alkali carbonates and niobium oxide is summarized in Equation (1.1). According to the thermogravimetric analyses the reaction occurs between 400 °C and 700 °C [16]. The usually reported calcination temperatures are between 750 °C and 950 °C [13, 14, 17].

$$K_2CO_3(s) + Na_2CO_3(s) + 2\ Nb_2O_5(s) \rightarrow 4\ K_{0.5}Na_{0.5}NbO_3(s) + 2\ CO_2(g) \quad (1.1)$$

A solid-state reaction mechanism of a metal carbonate and a metal oxide to form an ABO_3 perovskite has been already reported for the better-known systems, e.g., $BaTiO_3$. The solid-state reaction from $BaCO_3$ and TiO_2 was studied by Templeton and Pask [18]. They reported that at first, a small amount of $BaTiO_3$ is formed on the contact of the reagents. The subsequent reaction is diffusion controlled and in addition to the $BaTiO_3$, the Ba_2TiO_4 is produced in a prevailing amount until all the $BaCO_3$ is reacted. Finally, $BaTiO_3$ is formed at the expense of the Ba_2TiO_4 intermediate product through a reaction with the residual TiO_2.

Relatively little data are available on the actual reaction mechanism of KNN prepared using the solid-state synthesis, as this material is not so well studied as $BaTiO_3$. Malič et al. [19] investigated the solid-state reaction of KNN from alkaline carbonates and niobium pentoxide by diffusion couples. They found that at 600°C, KNN is formed via an intermediate phase that best corresponds to the solid solution $(K_xNa_{1-x})_2Nb_4O_{11}$. As presented in Figure 1.2, the intermediate phase is formed at the first contact of the carbonates with the niobium pentoxide. The reaction proceeds by the diffusion of K^+, Na^+ and O^{2-} ions through the reaction layer of the intermediate phase and KNN towards Nb_2O_5. The reaction rate is determined by the diffusion of the slower species, i.e., K^+.

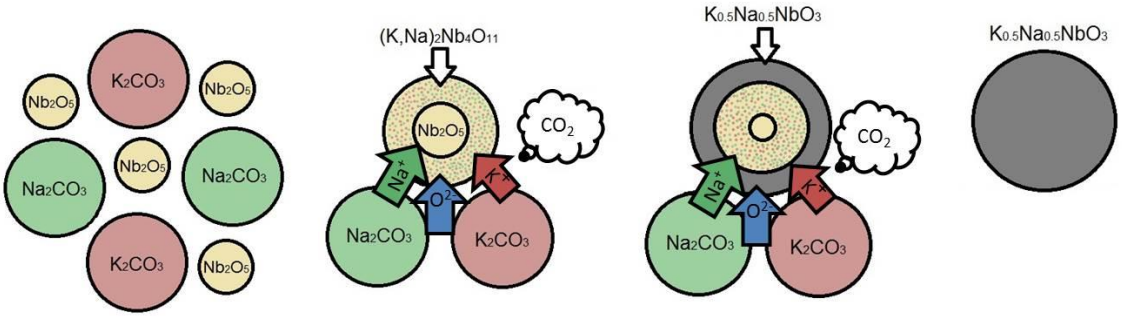


Figure 1.2: KNN reaction scheme. Reaction in a diffusion couple K_2CO_3+Na_2CO_3/Nb_2O_5 at 600°C. Redrawn after[19, 20].

Jenko, in her PhD thesis [20], studied the KNN solid-state synthesis from alkaline carbonates and niobium pentoxide with thermogravimetry (TG), differential thermal analysis (DTA) and evolved-gas analysis (EGA).

In Figure 1.3, we can see that the mass loss during the formation of KNN occurred in two steps accompanied by the two peaks on the DTG curve – the first with the double minimum at 485°C and 507°C and the second peak with the minimum at 600°C. The DTA curve had several endothermic processes with a sharp exothermic peak at 503°C, which was close to the temperature of the first minimum on the DTG curve.

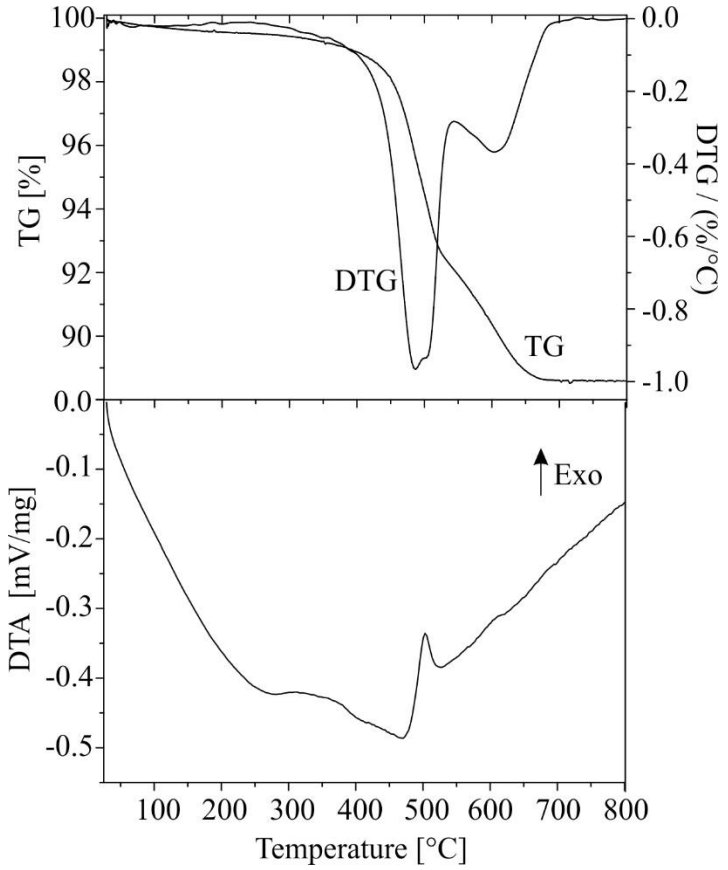


Figure 1.3: Thermal analysis curves. TG-DTG and DTA of the homogenized mixture of potassium and sodium carbonates and niobium pentoxide. Redrawn after Jenko [20].

The EGA analysis by Jenko [20] confirmed that the DTG curve shape corresponds to the EGA curve shape of the evolved CO_2 (see Equation (1.1)).

Jenko also annealed the homogenized reagents mixture to form KNN at different temperatures and recorded the X-ray diffraction spectra, so she could have found the temperature of the perovskite formation. Based on her results, the perovskite is formed at 500°C, which is also a temperature close to the DTA exothermic peak and the DTG first minimum. Jenko therefore suggested that the exothermic peak at 503°C on the DTA curve is connected with the formation of the perovskite phase.

1.2.1.2 Influence of reagents on the solid-state synthesis

As mentioned above, the typical reagents for the solid-state synthesis of KNN are the K_2CO_3, Na_2CO_3 and Nb_2O_5. The following chapter is divided into two parts – first about carbonates and the second dealing with the specifics of the niobium pentoxide.

The first, well-known obstacle to reproducible results of the KNN solid-state synthesis is the hygroscopicity of the potassium and sodium carbonates [19, 21, 22]. The rapid adsorption of water from the air is problematic when trying to achieve a stoichiometric composition. Drying at 200°C and weighing in a dry atmosphere are necessary [20, 22].

Tashiro and Ishii [23] in their study about Ba-doped KNN stress the milling of the carbonates prior to analysis in order to obtain dense ceramics. As is likely from the reaction scheme suggested by Malič et al. [19] (please refer to Figure 1.2), the carbonates should also have a uniform particle size distribution and a small particle size to obtain good homogeneity of the potassium and sodium carbonates and the niobium pentoxide particles in the initial mixture. This idea is theoretically supported by the studies effected on better known $BaTiO_3$. Buscaglia et al. [24] studied the influence of the particle size distribution of $BaCO_3$ on the solid-state synthesis of the $BaTiO_3$. They found that when using nanocrystalline TiO_2 and nanocrystalline $BaCO_3$ as

reagents, a single-phase $BaTiO_3$ was obtained after 10 h of calcination at 800°C, while in the case of the coarse $BaCO_3$ annealing for 4 h at 1000°C was necessary.

In analogy with $BaTiO_3$, the particle size distribution of the starting powders indeed seems to play a crucial role in the synthesis of KNN. The above studies justify the necessity of the pre-milling of carbonates to the particle size smaller than 1 µm as used in KNN solid-state synthesis and such has already been employed by different authors. Pavlič et al. [17] milled carbonates prior to the solid-state synthesis of KNN, Hollenstein et al. [25] milled all the reagents prior to synthesis, including the Nb_2O_5.

Based on the work of Malič et al. [19] on diffusion couples (Figure 1.2), the particle-size distribution of the Nb_2O_5 will determine the rate of the overall diffusion-controlled reaction since at the usual calcination temperature the diffusion of Nb^{5+} is negligible and only the diffusion of K^+, Na^+ and O^{2-} takes place. Therefore, the Nb_2O_5 used for the solid-state synthesis with carbonates should also have a uniform particle-size distribution with particles below 1 µm.

Jenko [20] in her PhD thesis compared the thermal decompositions of the carbonates, i.e., the courses of the solid-state reaction, of the three stoichiometric KNN homogenized mixtures with different particle-size distributions. The first mixture with d_{50} = 0.58 µm was prepared by the homogenization of the non-milled carbonates with non-milled fine Nb_2O_5 in the attritor mill. The mixture with d_{50} = 0.85 µm was prepared by mixing the non-milled carbonates with the non-milled fine Nb_2O_5 in a planetary mill and finally, the third mixture with d_{50} = 5.76 µm was prepared by manual mixing of non-milled carbonates with sintered Nb_2O_5 chunks in an agate mortar. Figure 1.4 shows the DTG curves of the three powders.

Jenko concluded that with the increasing particle size of the homogenized mixtures, the temperature of the carbonates' decomposition increases and the temperature interval of the decomposition becomes broader. At the same time, the end of the decomposition shifts towards higher temperatures [20].

Another specific of the Nb_2O_5, which is the most commonly used source of Nb in potassium sodium niobate solid-state synthesis, is the fact that it exists in different polymorphic forms. The formation of a polymorph is dependent on the production route and possible contamination [26]. The most common polymorphs are the orthorhombic γ-phase and the high-temperature-stable monoclinic α-phase. Literature on phase transformations reports significant differences in transition temperatures, and demonstrates the dependence on the Nb_2O_5's degree of purity and method of production. The reported transformation temperatures for Nb_2O_5 are the following: amorphous to orthorhombic around 450°C, orthorhombic to monoclinic around 900°C. Different monoclinic unit cells were found and they are denoted as $n, \alpha, \alpha_1, \alpha_2$ or β. Other nomenclature uses the signs T, B or H, and this is used in Figure 1.5, which summarizes the phase transformations between the Nb_2O_5 polymorphic forms. The phase transformations were reported to be irreversible [26]. The phase composition is not specified in the commercially available Nb_2O_5, nor in the scientific articles where Nb_2O_5 was used for the synthesis.

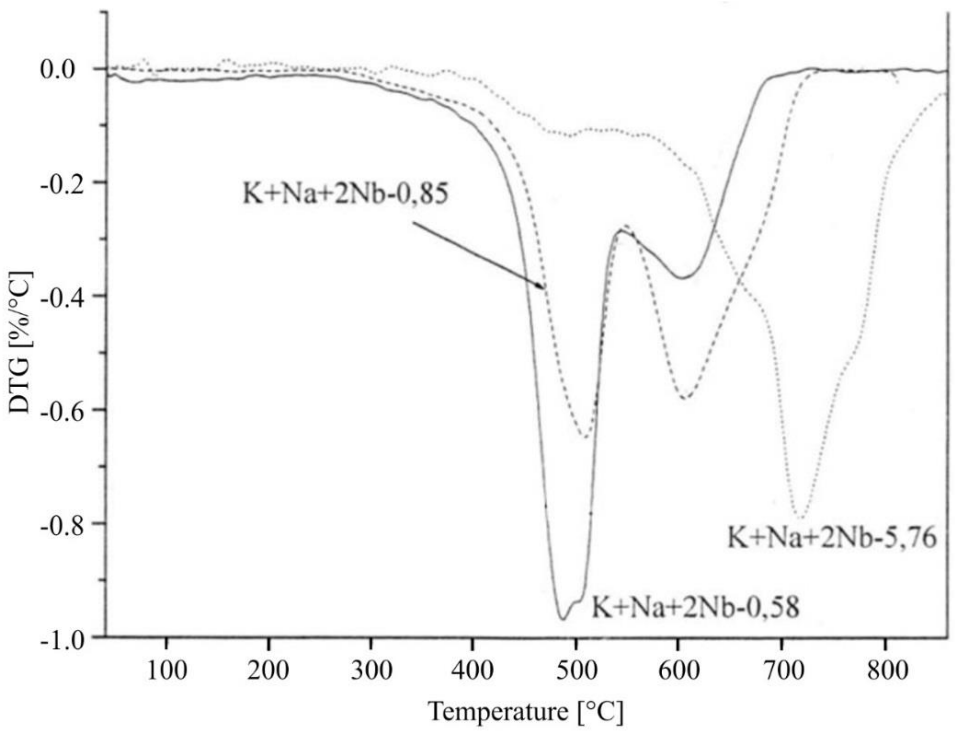


Figure 1.4: DTG curves of the K_2CO_3, Na_2CO_3 and Nb_2O_5 homogenized mixtures with different d_{50}. Redrawn after Jenko [20].

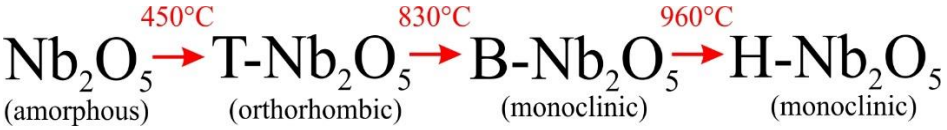


Figure 1.5: Nb_2O_5 polymorphs. Phase-transformation temperatures of different Nb_2O_5 polymorphic forms [27].

Very limited literature is available on the possible influence of the Nb_2O_5 phase composition on the solid-state reaction in niobates. Kuznetsova et al. [28] studied the samples of three commercial batches of Nb_2O_5. Each of the batches had a different ratio of monoclinic α and η polymorphs. They prepared $(Na_{1-x}Li_x)NbO_3$ ceramics from these Nb_2O_5. They reported that the polymorphous modifications of the Nb_2O_5 markedly affected the properties of the ceramics [28].

1.2.2 Sintering and microstructure

There is a general difficulty with obtaining dense, phase-pure KNN ceramics with a uniform microstructure. Already the early report on KNN by Kosec and Kolar [12] describes its typical, narrow sintering interval, with shrinking between 1000 °C and the solidus temperature at 1140°C. (see Figure 1.6). Such sintering behaviour typically results in maximum densities around 95 %TD, if solid-state sintering is used.

The example of a dense KNN microstructure consisting of cuboidal grains with comparable size after sintering at 1115°C, 2 h, in O_2, is shown in Figure 1.7a. However, KNN's tendency towards a bimodal microstructure with the large grains possessing intragranular pores, has been repeatedly reported, as a consequence of the abnormal grain growth [10, 29, 30]. As reported by Jenko et al. [29], the ceramics sintered at 1110°C, 2 h had grains of ~20 µm in a fine-grained matrix (see Figure 1.7b). The reported ceramics also contained a secondary phase, which was rich in Nb and poor in Na (see Figure 1.7c, bright phase marked with red arrow).

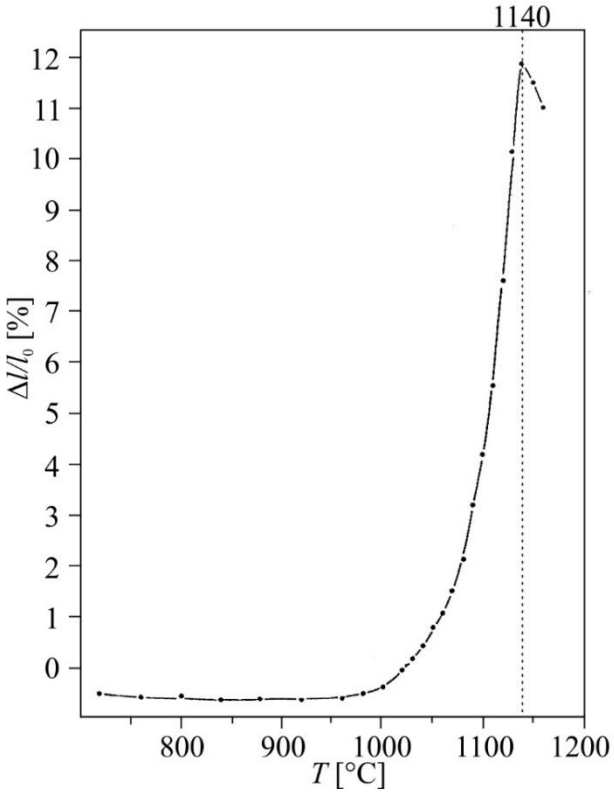


Figure 1.6: KNN sintering curve. Dotted line marks the melting point at 1140°C. Redrawn after [12].

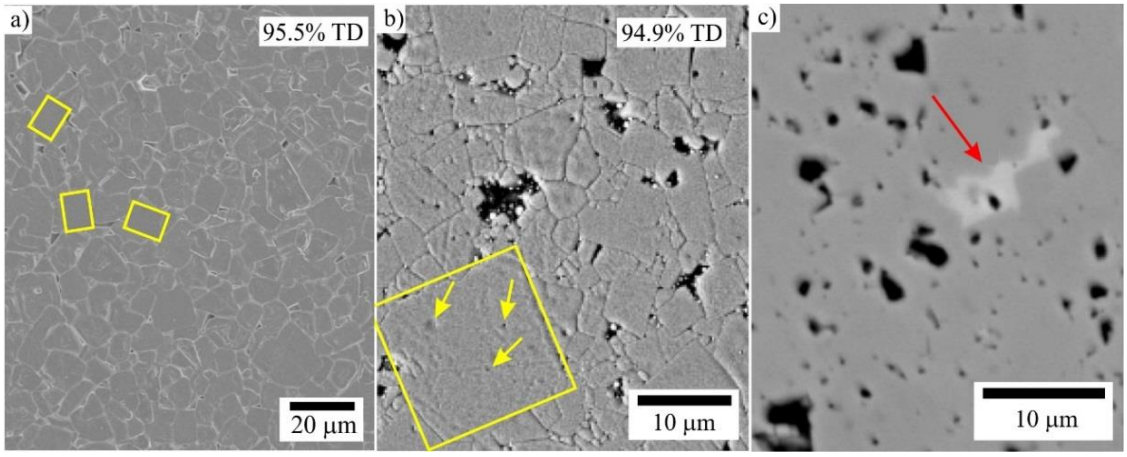


Figure 1.7: KNN microstructure with marked ceramics' densities and grains in yellow. a) dense microstructure with normal grain growth, sintered at 1115, 2 h, in O_2. Redrawn after [14] b) KNN ceramics with abnormal grain growth, arrows mark the intragranular pores and c) secondary phase poor in Na and rich in Nb with white contrast marked with red arrow. b) and c) prepared by sintering at 1110°C, 2 h, air, redrawn after [29].

1.2.3 Crystal structure

KNN belongs to the perovskite group with the general formula ABO_3, with K^+ and Na^+ being the A-site ions and Nb^{5+} being the B-site ion. In their first report about KNN in 1954, Shirane et al. [8] characterized the crystal structure of $K_xNa_{1-x}NbO_3$ for x = 0.1–0.5 as orthorhombic at room

temperature based on the X-ray diffraction (XRD) analysis. However, a later study of potassium sodium niobates with neutron diffraction by Ahtee and Hewat in 1975, stressed that refinement of the composition $K_{0.1}Na_{0.9}NbO_3$ would be more precise with a monoclinic unit cell, although the difference between the orthorhombic and monoclinic unit cells was very small. Shiratori et al. [31], then 30 years later used a monoclinic unit cell to index the crystal structure of KNN in a XRD study combined with Raman spectroscopy.

In 2009, Tellier et al. studied the crystal structure and phase transitions of the $K_xNa_{1-x}NbO_3$ perovskites from x = 0.4–0.6. She used the monoclinic unit cell and the *Pm* space group (SG no. 6) for the refinement of the unit-cell parameters and described the correlation between the orthorhombic unit cell and its monoclinic subcell of KNN, as shown in Figure 1.8 [32].

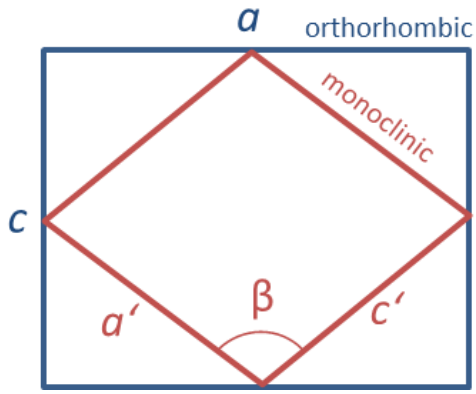


Figure 1.8: The relationship between orthorhombic and monoclinic $K_xNa_{1-x}NbO_3$ (x = 0.4-0.6) unit cells [32]. a and c are the cell parameters of the orthorhombic unit cell, while a', c' and β of the monoclinic unit cell. $a = a' \sin(\beta/2) + c' \sin(\beta/2)$, $b = 2b'$ and $c = c' \cos(\beta/2) + a' \cos(\beta/2)$.

Benčan et al. [33] in their study of a KNN single crystal by transmission electron microscopy (TEM) with the selected-area electron diffraction technique show the splitting of the 180°domains viewed in the [010] zone axis. This splitting can be best explained by taking into account the monoclinic β angle, which was measured to be ~90.3°.

Rafiq et al. [34] supported the KNN monoclinic unit-cell assignment by studying the monodomains in a KNN single crystal using polarized Raman spectroscopy. The complete assignment of the Raman modes was possible only when considering the monoclinic unit cell.

In this thesis the monoclinic unit cell with the *Pm* space group is going to be used for the crystal structure refinement, despite the majority of the scientific publications still refining the KNN as orthorhombic [35-37].

1.2.3.1 **Phase transitions**

KNN undergoes a series of phase transitions upon heating from the low-temperature rhombohedral phase (R) via the monoclinic/orthorhombic (M/O) phase existing at room temperature, a subsequent tetragonal phase (T) and finally to the paraelectric cubic phase (C). The temperatures of the phase transitions are: R→M at around 130 K [38, 39] M→T at around 470 K [9, 32, 38, 39] and T→C at around 685 K [32, 38, 39], as shown in Figure 1.9.

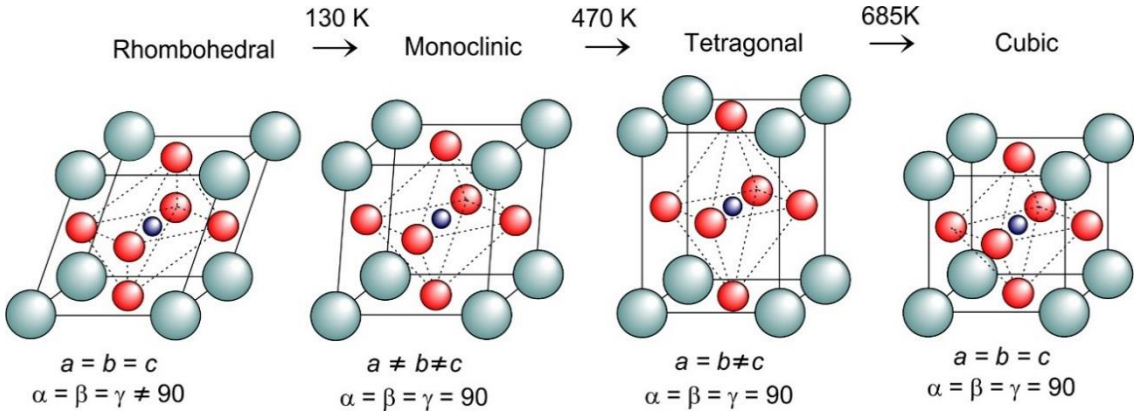


Figure 1.9: The phase transitions in KNN. Temperatures are averages based on the reports from different authors [9, 32, 38, 39].

When cooling down the KNN in the monoclinic/orthorhombic phase, rhombohedral nanoclusters within the M/O matrix appear and grow with the decreasing temperature, as shown in the scheme in Figure 1.10 [38].

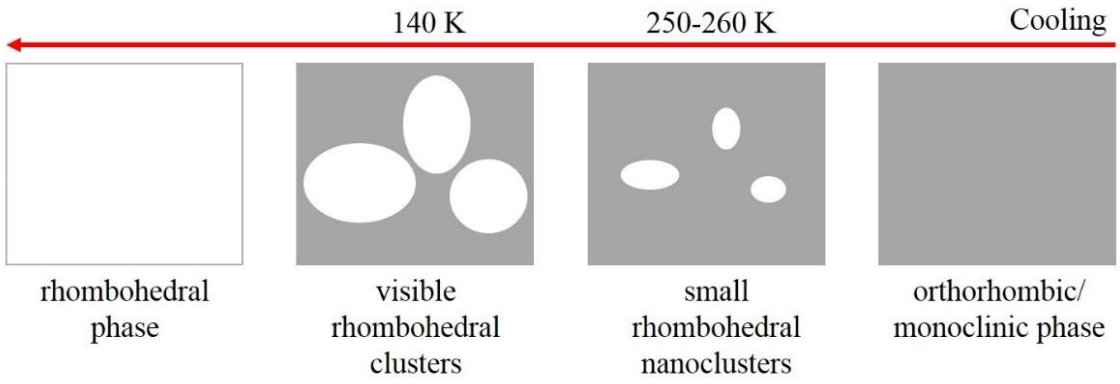


Figure 1.10: Rhombohedral nanoclusters. Appearance and growth of the rhombohedral nanoclusters in the matrix of the room-temperature phase (M/O) upon cooling [38].

1.3 Doping of Perovskites

Doping is a method often used for materials engineering. Let us focus on the perovskites with the general formula ABO_3 since they are the subject of this thesis. Figure 1.11 presents the classification of doping in a diagram. The basic classification can be based on the three criteria: First, according to which atom is replaced, we recognize i) A-site or ii) B-site doping. Second, based on the valence of the dopant, we may divide the doping into two categories: i) isovalent substitution, when the dopant has the same charge as the replaced atom ii) aliovalent substitution, which can be further divided into a) donor and b) acceptor doping. The donor dopant has more positive charge than the atom we wish to modify, while the acceptor dopant has more negative charge than the atom to be replaced. The third criterion is how the dopant is added – there are different ways for the dopant's introduction with regard to the stoichiometry a) the substitution, when the dopant is introduced with taking into account maintaining the neutral charge of the system or b) addition, when the dopant is added to the stoichiometric matrix composition [40, 41].

If the concentration of the dopant exceeds the concentration of the intrinsic defects in the matrix material, the introduced impurity gives rise to a compensating defect [40]. The charge-

compensation mechanism of the introduced donor or acceptor dopant is therefore strongly dependent on all of the criteria above as well as on other factors like the dopant concentration.

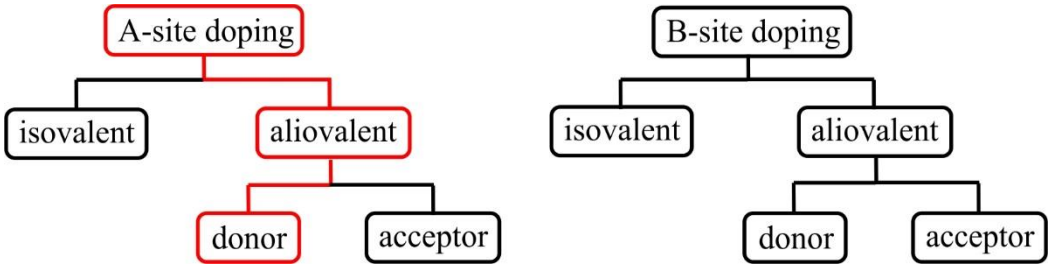


Figure 1.11: Doping classification. The red path marks the way of doping used in this thesis.

Although materials engineering usually aims for the optimization of the functional properties, there are also other effects of doping. Such secondary effects are commonly found in the literature on doped perovskite ceramics and might complicate the engineering of the materials, if they are not intended from the start.

In the following chapters, the A-site donor doping of the ABO_3 perovskites is discussed in general (see Figure 1.11, red path) from the point of view of the secondary effects, i.e., structural and microstructural changes upon doping. The lead-based materials as well as the lead-free representative $BaTiO_3$ are taken as examples, since they are well studied and at the same time, structurally related to KNN.

1.3.1 Structural and microstructural changes upon A-site donor doping of ABO_3

In this section, the effect of the A-site donor doping, first on the structure, then the microstructure and finally both effects together are discussed, since the two effects appear to be related.

To start with the effect on the structure, in their study of $BaTiO_3$ donor-doped with La^{3+} according to the formula $Ba_{1-x}La_xTi_{1-x/4}O_3$, which was prepared by the solid-state reaction of oxide mixtures, Morrison et al. [42] reported, that the degree of tetragonality c/a strongly depends on the La content (see Figure 1.12a). While the XRD pattern for the undoped $BaTiO_3$ can be indexed with the $BaTiO_3$ tetragonal unit cell having parameters a = 3.9951(6) Å and c = 4.0303(9) Å, the lattice parameters change with the increasing x in three regions. First, a decreasing degree of tetragonality is observed up to x = 0.05, which has a cubic symmetry with a = 4.0022(4) Å. Second, the cubic symmetry is retained with the decreasing a down to a = 3.9963(3) for x = 0.10. Finally, the third region is where the increasing x does not significantly influence the cell parameters until x = 0.20.

A similar effect has been reported in other studies on the La-doped $BaTiO_3$ as well [43, 44]. For example, Itoh et al. [45] observed this effect of the increasing La content in $(BaLa_x)(Ti_{1+x})O_{3+\delta}$ prepared by ball milling of the commercial $BaTiO_3$ powder and La_2O_3, as a decrease of the (002) and (200) peak splitting (see Figure 1.12b, peaks close to 45°2θ).

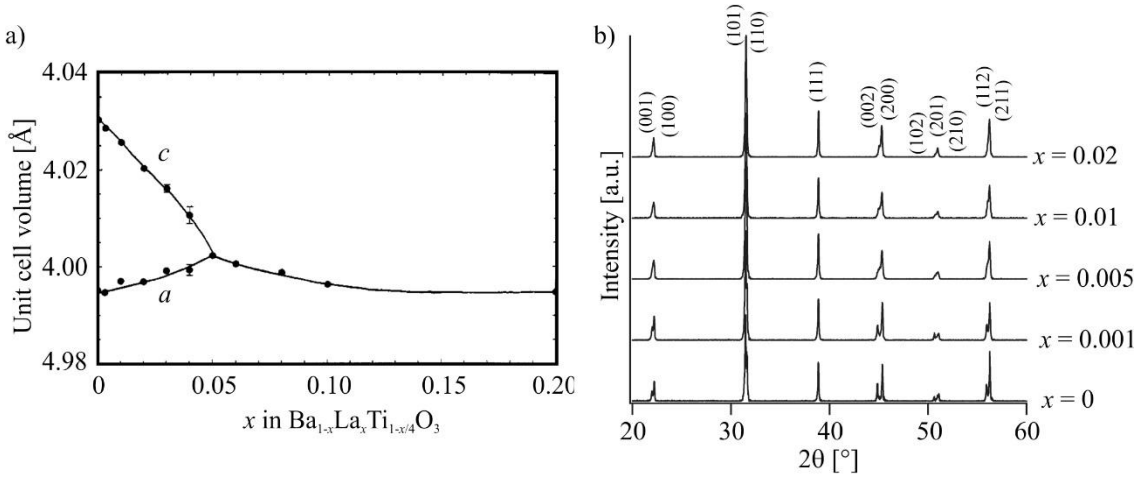


Figure 1.12: Lattice parameters in La-doped $BaTiO_3$. a) variation of unit-cell parameters and cell volume with *x*, in $Ba_{1-x}La_xTi_{1-x/4}O_3$ at room temperature. Redrawn after [42] b) XRD patterns of $(BaLa_x)(Ti_{1+x})O_{3+\delta}$. Redrawn after [45].

Morrison et al. in their study [42] also describe the effect of different dopants on the $BaTiO_3$ structural phase transitions. As shown in Figure 1.13a, the La-doping in $BaTiO_3$ results in a decreasing effect on the T_c and $T_{o/t}$, which is in comparison with other dopants really significant (Figure 1.13b).

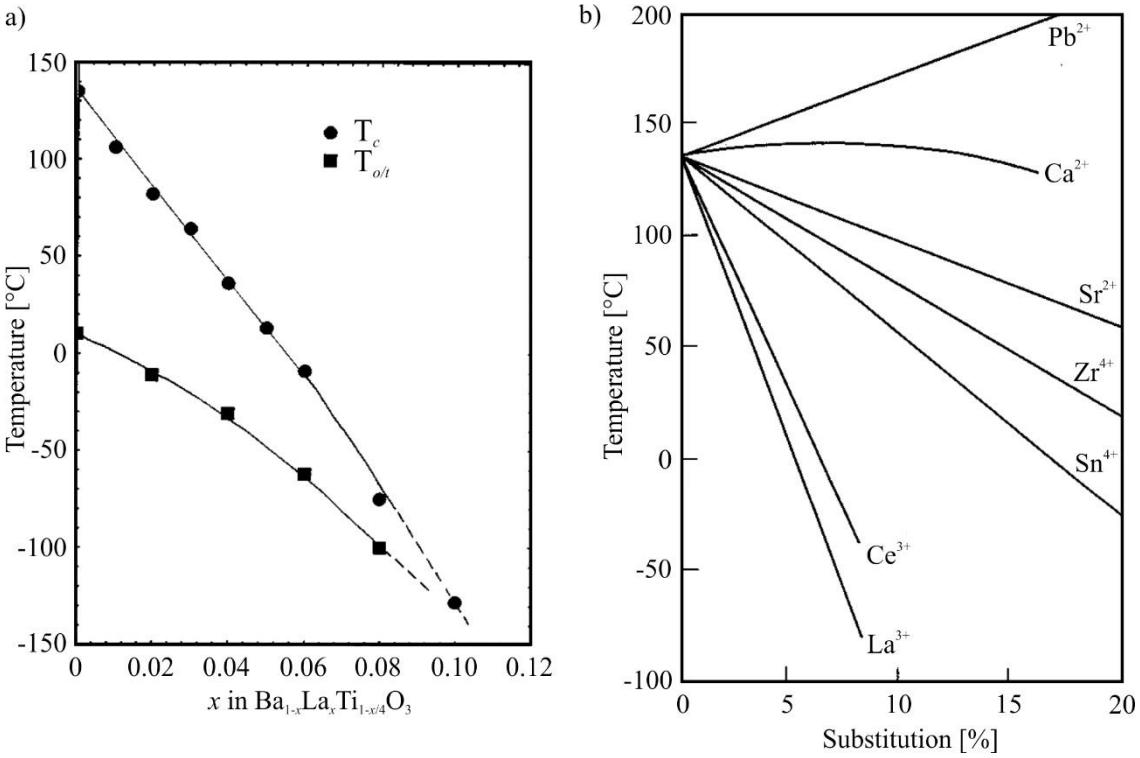


Figure 1.13: Changes of T_c and $T_{o/t}$ in doped $BaTiO_3$ a) in La-doped $BaTiO_3$ b) in $BaTiO_3$ doped with different dopants: Pb^{2+}, Ca^{2+}, Sr^{2+} as isovalent A-site dopants, Zr^{4+} and Sn^{4+} as isovalent B-site dopants and Ce^{3+} and La^{3+} as aliovalent A-site dopants. Redrawn after [42].

Regarding the changes in microstructure, the most visible effect of the A-site donor doping is the change in the grain size.

Rahaman and Manalert [41] describe a so-called “doping threshold” in $BaTiO_3$, which determines the grain growth behaviour based on the dopant concentration. In donor-doped $BaTiO_3$, below a doping level of a few tenths of 1 at%, the sintered material has a coarse-grained microstructure. Above this threshold, the microstructure is fine-grained. Donor dopants are therefore effective in inhibiting the grain growth.

Smyth [40] in his textbook relates the abrupt grain growth change in donor-doped $BaTiO_3$ at room temperature with the dopant-compensation mode. For the dopant levels up to 1 at% the electronic compensation resulting in a conductive, dark-coloured material is likely, while for the higher donor-dopant concentrations, the dopant is rather compensated ionically (by cation vacancies) and the material becomes a light-coloured insulator.

The grain growth inhibition with the increasing dopant concentration is often perceived as the segregation or gradient of the dopant near the grain boundaries or the core-shell structure (see a typical core-shell structure in Figure 1.14).

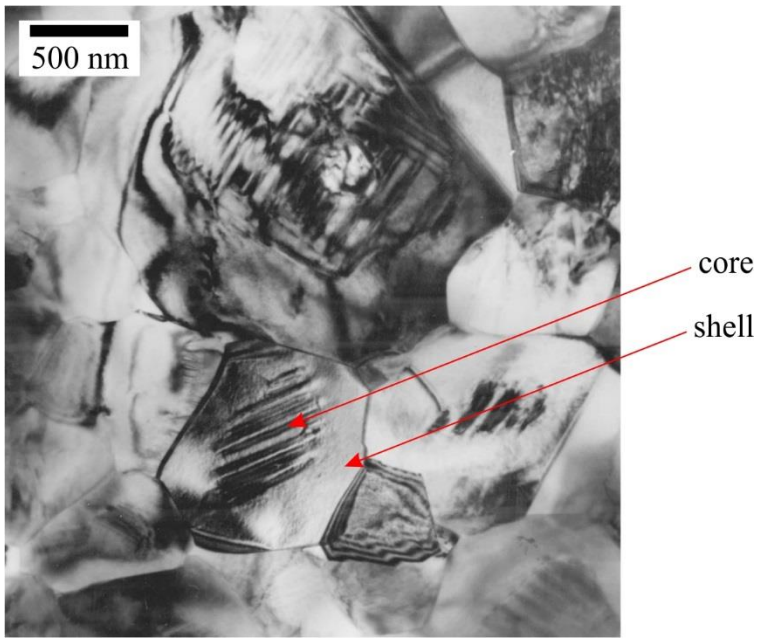


Figure 1.14: TEM micrograph of $BaTiO_3$ doped with 1.5 at% La with a typical core-shell structure. The image was taken at ~90°C. Redrawn after [46].

Figure 1.14 presents a typical core-shell structure of the La-doped $BaTiO_3$, which is easy to recognize due to the cores having ferroelectric domains and shells without them. The absence of the ferroelectric domains in the shell is due to the presence of La in the shell and not in the core, since the La decreases the T_C, at 90°C, the doped shell is already cubic, while the core remains tetragonal, therefore ferroelectric.

In the number of studies performed on the doped $BaTiO_3$ [46-48], the dopant core-shell structure was connected to the decrease of the grain-boundary mobility. However, the compositional inhomogeneity within the grains might be related to the fact that the dopant in these studies is introduced by sintering of the already formed $BaTiO_3$ powder together with the dopant and incorporates mainly during the grain growth [46]. The diffusion rate of the dopant in the perovskite lattice is then not sufficient for the dopant to distribute homogenously.

The issue of the insufficient diffusion rate of the dopant in the perovskite lattice to distribute homogenously was verified by the diffusion-couple study by Hammer and Hoffmann [49] in their paper on La-doped PZT. The couple was prepared by cold isostatic pressing and sintering together two PZT parts with different Zr/Ti ratios and 2% of La. It was found that La preferably diffuses on the Ti-rich side of the diffusion couple, while there is a La-depletion on the Zr-rich side of the couple (Figure 1.15).

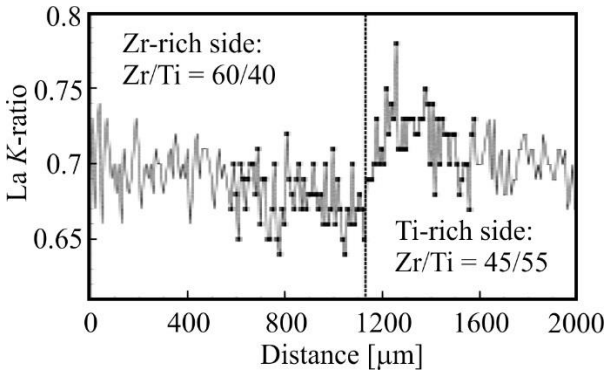


Figure 1.15: La/PZT diffusion couple. WDXS line scan of microprobe analysis through the interface (marked with the dashed vertical line) of the diffusion couple revealing a preferred La diffusion into the Ti-rich PZT composition. Redrawn after [49].

Furthermore, Hammer and Hoffman [49] found the grain size in $Pb_{1-(3/2x)}La_x(Zr_{0.53}Ti_{0.47})O_3$ to be drastically decreasing with the increasing amount of the A-site donor dopant La^{3+}. The following compositional inhomogeneities were found: La- and Ti-rich cores of the grains, the film of PbO-rich secondary phase on the grain boundaries and in the triple junctions and finally the Pb-vacancy gradient within the PZT grains. The Ti-rich grain cores and Zr-rich grain-boundary regions were found already in the undoped PZT, which was explained as a consequence of the PZT ceramics reaction. According to the authors, the grain-growth inhibition in the studied samples originates from the chemical inhomogeneities and not from the La-segregation at the grain boundaries. This means that the hypotheses that the core-shell structure is a consequence of the dopant and thus the dopant is the reason for the decreased grain size, were not confirmed in the study of La-doped PZT made by Hammer and Hoffmann.

1.3.2 Doping of KNN

In order to improve the densification or the optical properties, an increase in the Curie temperature T_C or the piezoelectric coefficient d_{33}, lower dielectric losses $\tan\delta$ or improved planar mechanical coupling factor k_p, KNN has been doped by different dopants. Table 1.1 summarizes the single element dopants of the KNN's composition and their effect on the KNN's properties, as well as their eventually reported effects on the KNN's structure, grain growth, or phase composition, with regard to the kind of doping (A-site, B-site, donor, acceptor). Therefore only results from the reports using single element doping with a clearly stated formula are presented in Table 1.1.

Besides the combining of the dopants in Table 1.1, KNN was reported to be co-doped with, e.g., Zn and Sn [50] or by Li, W and Bi [51].

A common chemical modification of KNN is adding different ABO_3 solid solutions. The most often reported are the KNN solid solutions with $LiNbO_3$, $LiTaO_3$ and $LiSbO_3$, among which the so-called Toyota composition is one of the best performing and therefore most studied KNN-based materials [6, 52-59]. Another interesting solid solution with KNN is formed with $SrTiO_3$ [60-63], which induces a relaxor-like behaviour in KNN [64].

In addition to the undoped or doped KNN, the composition is often modified so that the dopants are added to the stoichiometric matrix as additives or sintering aids, such as CuO [65-69], ZnO [70-72], MnO_2 [69, 70] or SnO_2 [66, 72].

As was emphasized by Rödel et al. [5] in his latest review on lead-free piezoelectric materials in applications, the further improvement of the properties of lead-free materials is conditioned by a deeper understanding of the doping mechanism at the atomic level.

Table 1.1: Literature review on single element KNN dopants. The list is completed with the kind of doping used, based on the reported formula. GS – grain size, AGG – abnormal grain growth, ↑ increase, ↓ decrease, ~ comparable, compared to KNN. T_C - ferroelectric Currie temperature, ε - dielectric permittivity, $\tan\delta$ - dielectric losses, d_{33} – piezoelectric coefficient, planar (k_p) and thickness (k_t) mechanical coupling factors.

Dopant	Dopant concentr. *x*	Formula	A-site/ B-site	Acceptor/ donor/ isovalent	Density	Sintering cond.	Grain size	Secondary phase	Structural changes	Properties	Ref.
Zr^{4+}	0.005	$K_{0.5}Na_{0.5}Nb_{1-x}M_xO_3$	B-site	acceptor	↑	1125°C, 2 h	↓GS, ↓AGG	no	–	$\downarrow T_C$, $\downarrow\varepsilon$, $\downarrow\tan\delta$, $\uparrow d_{33}$, $\uparrow k_p$	[73]
Ti^{4+}	0.005	$K_{0.5}Na_{0.5}Nb_{1-x}M_xO_3$	B-site	acceptor	↑	1125°C, 2 h	↓GS, ↓AGG	no	–	$\downarrow T_C$, $\downarrow\varepsilon$,, $\downarrow\tan\delta$, $\uparrow d_{33}$, $\uparrow k_p$	[73]
Mo^{6+}	0.02, 0.04, 0.06, 0.08	$K_{0.5}Na_{0.5}Nb_{1-x}Mo_xO_3$	B-site	donor	–	–	~GS	*x* = 0.08 impurity phase	pseudocubic tendency	induced photolum. $\sim T_C$, $\downarrow\varepsilon$,, $\sim\tan\delta$	[74]
Li^{+}	0.05, 0.06, 0.065, 0.07	$Li_x(Na_{0.5}K_{0.5})_{1-x}NbO_3$	A-site	isovalent	~	1065-1135°C, 10-60 min	–	–	orthorhombic to tetragonal	$\uparrow T_C$, $\uparrow\varepsilon$, $\downarrow\tan\delta$	[25]
	Up to 0.70				–	–				$\uparrow d_{33}$ & $\uparrow k_p$ up to *x* = 0.10, $\uparrow k_t$ until *x* = 0.07	[75]
Mn^{4+}	0.02	$K_{0.5}Na_{0.5}Nb_{0.98}Mn_{0.02}O_3$	B-site	acceptor	↓	1160°C, 1 h	~GS	no	~ unit cell	$\sim T_C$, $\sim\varepsilon$, $\downarrow\tan\delta$, $\uparrow d_{33}$	[59]
Mg^{2+}	0.005	$K_{0.495}Na_{0.495}Mg_{0.005}NbO_3$	A-site	donor	↑	1125°C, 24 h	↓GS	no	–	$\downarrow\varepsilon$, $\downarrow\tan\delta$, $\downarrow k_p$	[12]
	0.005	$K_{0.495}Na_{0.495}Mg_{0.005}NbO_3$	A-site	donor	↓	1115°C, 2 h	–	no	pseudocubic tendency	–	[76]
Ca^{2+}	0.005	$K_{0.495}Na_{0.495}Ca_{0.005}NbO_3$	A-site	donor	~	1115°C, 2 h	–	no	pseudocubic tendency	$\uparrow\varepsilon$, $\uparrow\tan\delta$, $\uparrow d_{33}$	[76]
Ba^{2+}	0.005	$K_{0.495}Na_{0.495}Ba_{0.005}NbO_3$	A-site	donor	↓	1115°C, 2 h	–	$(NaK)Nb_8O_{21}$	pseudocubic tendency	–	[76]
Sr^{2+}	0.005, 0.02, 0.05, 0.10	$(K_{0.5}Na_{0.5})_{1+2y}Sr_yNbO_3$	A-site	donor	↑ for *x* = 0.005	1115°C, 2 h	↓GS	*x* = 0.10, polyniobate compounds	pseudocubic tendency	$\downarrow T_C$, $\uparrow\varepsilon$, $\downarrow\tan\delta$, $\uparrow d_{33}$ for *x* = 0.005	[76, 77]

1.3.2.1 **Doping KNN with Sr**

As was explained in the Section 1.2.2, the densification of KNN is peculiar. However, it is known that the presence of A-site vacancies in an ABO_3 perovskite results in an enhanced diffusion and subsequently an improved densification [7]. In the case of KNN, the alkaline earth metals are promising candidates for the A-site donor doping that can be compensated by the formation of A-site vacancies [7]. The most suitable dopants for KNN would be the ones that have a similar ionic radius to K^+ (0.164 nm for CN = 12) [78] and Na^+ (0.139 nm for CN = 12) [78]. Sr^{2+} has an atomic radius right between the radii of K^+ and Na^+, i.e., 0.144 nm for CN = 12 (see Figure 1.16) [78].

Malič et al. [76, 77] in their studies indeed confirmed that Sr doping improves the density and electrical properties of KNN when 0.5 or 1% Sr are added. Doping of KNN with 0.5% of Sr^{2+} resulted in a density of 96 %TD, if sintered at 1115 °C, higher ε = 500, and d_{33} = 95 pC/N and lower $\tan\delta$ = 0.04, as compared to 94.4 %TD, 450, 80 pC/N and 0.06, respectively, for the undoped KNN prepared within the same study [76].

In their subsequent study [77], Malič et al. prepared KNN ceramics according to the formula $(K_{0.5}Na_{0.5})_{1-2y}Sr_y\square_yNbO_3$, where $\square$ means A-site vacancy, with y = 0, 0.5, 2, 5 and 10% of Sr^{2+}. Figure 1.16 shows the intended structure with Sr^{2+} occupying the A-site, and the associated A-site vacancy. While the dielectric constant ε kept increasing and $\tan\delta$ decreasing with the Sr content, there was a negative effect on the density (see Figure 1.17c) and d_{33} above 0.5% Sr.

On the other hand, Maeder et al. [79] reported the increase of ε to 500 for the KNN doped with 1% Sr, while the 0.5% Sr resulted in decreased ε = 330, as compared to the ε = 400 for undoped KNN. The d_{33} however increased for both 0.5 and 1% Sr, 90 and 110 pC/N, respectively, compared to only 70 pC/N for the undoped KNN. Neither the densities nor the sintering conditions for the Sr-doped KNN were reported by Maeder et al.

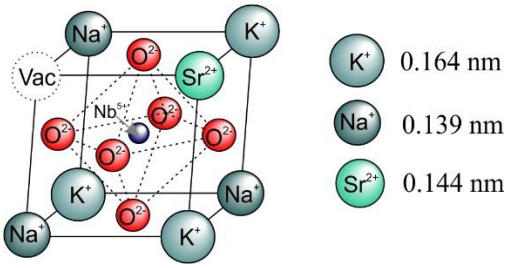


Figure 1.16: Sr-doped KNN unit cell. Image showing the intended unit cell with A-site vacancies based on the formula $(K_{0.5}Na_{0.5})_{1-2y}Sr_y\square_yNbO_3$.

Besides the improved density, lower tanδ and increase in ε and d_{33}, for 0.5% Sr dopant, there were other effects of Sr on KNN: with the increasing Sr content, Malič et al. [77] reported a decrease of the orthorhombic distortion evident as a decrease of the XRD peak splitting in Figure 1.17a. The Rietveld refinement of the unit cell parameters of the XRD spectra in Figure 1.17a confirmed a tendency towards pseudocubic syngony. This indicated that Sr ions actually incorporated into the perovskite lattice. In the spectrum of the KNN-10% Sr the additional diffraction peaks (marked * in Figure 1.17a) could be fitted to the following potassium polyniobate compounds: $K_2Nb_4O_{11}$, $K_2Nb_8O_{21}$, $K_{5.75}Nb_{10.85}O_{30}$ or $K_6Nb_{10.88}O_{30}$; however, the possibility that one of these phases contained sodium and/or strontium could not be excluded and would have required further analysis.

Furthermore, Sr doping caused the decrease of T_C (Figure 1.17b) as is visible on the temperature dependence of dielectric constant for KNN and KNN-5% Sr.

And finally, despite identical sintering conditions, i.e., 1115°C, 2 h, there was a dramatic decrease in the grain size, as seen in Figure 1.17c. The densities are marked on the images of the fractured ceramics. However, adding as little as 0.5% Sr resulted in a significant grain-size decrease, although the density was as high as 95.8 %TD.

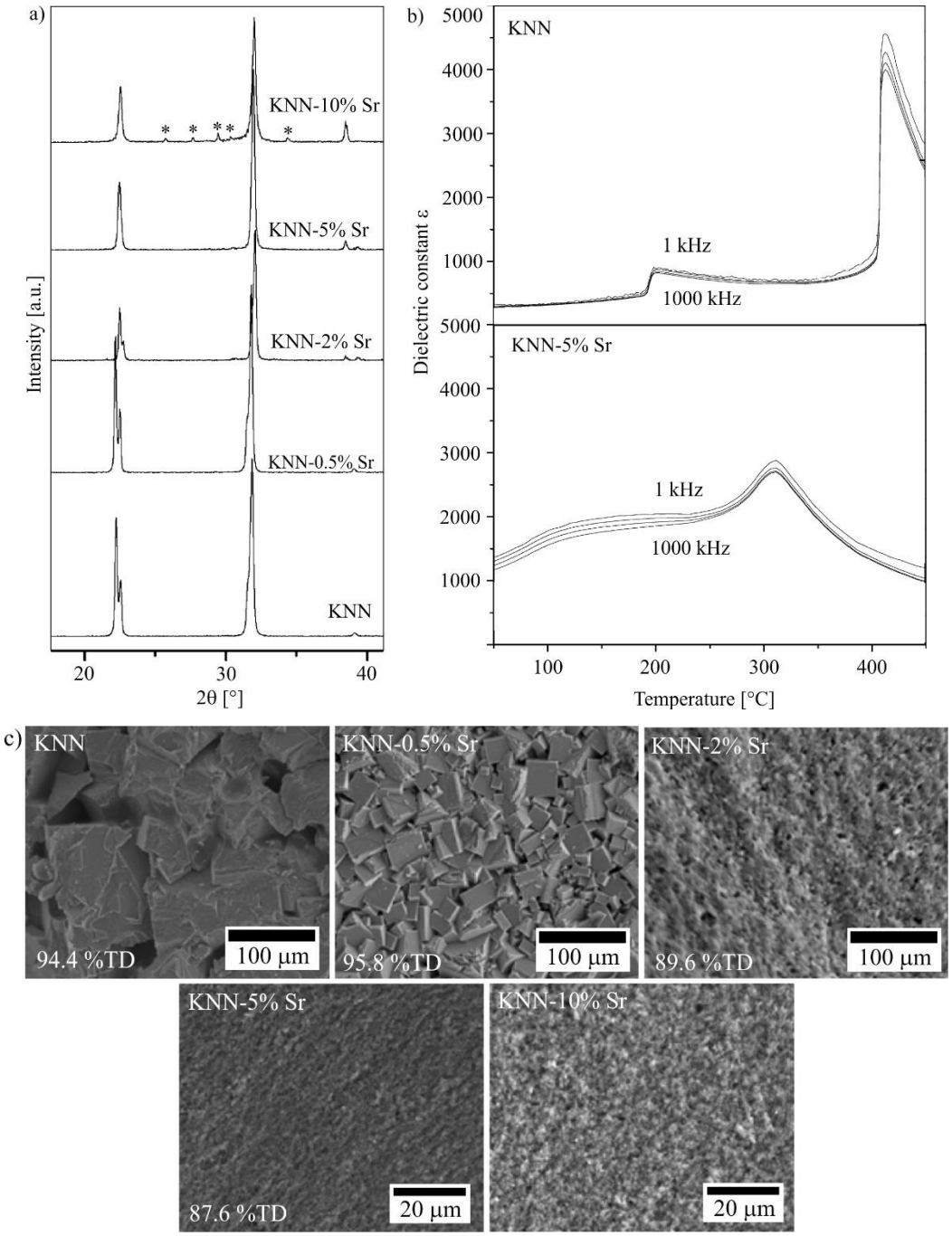


Figure 1.17: Effects of Sr on KNN by Malič et al. a) XRD spectra of the KNN and Sr-doped KNN sintered ceramics, * mark the peaks of a secondary phase b) Temperature dependence of the dielectric constant at 1, 10, 100 and 1000 kHz for sintered KNN and KNN-5% Sr c) SEM micrographs of the fracture surfaces of sintered KNN and Sr-doped KNN ceramics with marked densities, the density of KNN-10% Sr was not evaluated. Redrawn after [77].

Chapter 2

Aims and Hypotheses

Based on the topics, this thesis is divided into three main parts. In the first part, the undoped KNN solid-state synthesis is studied, while the second and third parts investigate KNN doped with Sr with reference to the undoped KNN.

The aim of the first part is to investigate the influence of the polymorphic form of Nb_2O_5 on the solid-state synthesis and sintering of KNN. Two batches of KNN are prepared using identical procedures from two different Nb_2O_5 polymorphs, i.e., orthorhombic and monoclinic. The reactions of the two homogenized mixtures are studied. The possible reasons for the Nb_2O_5 polymorphs' different reactivity with the alkaline carbonates during the synthesis of KNN are discussed.

The second part of the thesis is designed to better understand the course of the solid-state reaction KNN doped with Sr using the thermal analysis and *in situ* high-temperature X-ray diffraction, the latter providing information about phase composition changes during the solid-state synthesis.

In the last part of the dissertation, the effects of Sr on the KNN ceramics' structure and microstructure are studied using advanced, modern analytical methods. The compositional homogeneity of the Sr-doped KNN samples is verified. The grain boundaries of the Sr-doped KNN are investigated at the atomic level in order to provide an explanation for the observed dopant effects.

For this dissertation, the following hypotheses were formed:

- The niobium pentoxide polymorphic form and its particle size distribution are important factors influencing both the course and the reproducibility of the solid-state synthesis of KNN ceramics
- The donor doping of KNN with Sr influences the local perovskite structure, which subsequently has an impact on the microstructure and phase composition of the ceramics

Chapter 3

Materials and Methods

3.1 List of Chemicals and Accessories

Table 3.1: List of chemicals and accessories. A detailed description of the chemicals and accessories mentioned in the Materials and Methods section are listed in alphabetical order according to the item name.

Chemical	Product and producer
2-propanol	Carlo Erba Reagents, Val de Reuil, France
acetone	Carlo Erba Reagents, Val de Reuil, France
diamond pastes	¼ and 3 μ m DP paste, Struers, Ballerup, Denmark
K_2CO_3	anhydrous, 99.9+ %, ChemPur, Karlsruhe, Germany
Na_2CO_3	anhydrous, 99.9+ %, ChemPur, Karlsruhe, Germany
Nb_2O_5 Sigma- Aldrich	325 mesh, 99.9 %, Sigma-Aldrich, Steinheim, Germany
Nb_2O_5 Alfa Aesar	99.9985 %, Alfa Aesar, Karlsruhe, Germany
$SrCO_3$	99.994%, Alfa Aesar, Karlsruhe, Germany
stearic acid	97 %, Acros Organics, Geel, Belgium

Accessories	Product and producer
milling balls ϕ 10 mm and ϕ 3 mm ZrO_2-Y_2O_3	Tosoh Corporation, Tokyo, Japan
milling vial 125 ml, ZrO_2-Y_2O_3	Retsch, Haan, Germany
milling vial 150 ml or 50 ml, polyethylene	custom-made
mounting epoxy	VersoCit-2 Kit, Struers, Ballerup, Denmark
SiC grinding papers	Struers, Ballerup, Denmark

3.2 Solid-State Synthesis and Sintering of KNN and Sr-Doped KNN

Ceramic powders with the nominal formula $(K_{0.5}Na_{0.5})_{1-2y}Sr_yNbO_3$, for y = 0, 0.005, 0.01, 0.02, 0.06 and 0.08, subsequently referred to as KNN, KNN-0.5% Sr, KNN-1% Sr, KNN-2% Sr, KNN-6% Sr and KNN-8% Sr, were prepared by solid-state synthesis from the following starting powders: K_2CO_3, Na_2CO_3, $SrCO_3$ and Nb_2O_5 from Sigma-Aldrich or from Alfa Aesar.

3.2.1 Preparation of the reagents prior to synthesis

Each of the reagents was dried for 6 h at 200°C and then ball milled in a planetary mill (Retsch PM 400, Haan, Germany). The Na_2CO_3 and K_2CO_3 were milled in a 250 ml polyethylene vial with 370 g of ϕ3 mm and 23 ϕ10 mm ZrO_2-Y_2O_3 milling balls. The $SrCO_3$ was milled in a 50 ml polyethylene vial with 50 g of ϕ3 mm and 5 ϕ10 mm ZrO_2-Y_2O_3 milling balls. The Nb_2O_5 was milled using a 125 ml ZrO_2-Y_2O_3 milling vial with 150 g of ϕ3 mm milling balls only.

The milling conditions for all the powders were as follows: 175 rpm for 4 h and 12 ml of acetone as a milling medium per 10 g of powder, except for the $SrCO_3$ where 5 ml of acetone was used per 10 g of the powder. After the milling, the slurries were dried for 1 h at 105°C and 2 h at 200°C and subsequently sieved through a 300 µm mesh. All the powders were stored in a desiccator to avoid the adsorption of atmospheric humidity.

3.2.2 Solid-state synthesis

The milled and dried reagents were weighed in a stoichiometric ratio in a dry box in a protective Ar atmosphere, to prepare KNN from two different Nb_2O_5 and Sr-doped KNN with different Sr concentrations.

The mixtures were then homogenized in a planetary mill using the 125 ml ZrO_2-Y_2O_3 milling vials with 150 g of ϕ3 mm ZrO_2-Y_2O_3 milling balls. The milling conditions were 175 rpm for 4 h and 12 ml of acetone as a milling medium per 10 g of the powder. After the milling, the slurries were dried for 1 h at 105°C and 2 h at 200°C and subsequently sieved through a 300 µm mesh.

The homogenized mixtures were compacted into pellets of ϕ22 mm with a uniaxial press (PW10, Paul-Otto Weber Laborpresstechnik, Remshalden, Germany) at 50 MPa using stearic acid as a lubricant for the pressing model. The compacts were then placed in a covered alumina crucible on a Pt-foil and calcined two times in a chamber furnace (Custom-made, Terna d.o.o., Ljubljana, Slovenia) with the temperature program as in Figure 3.1.

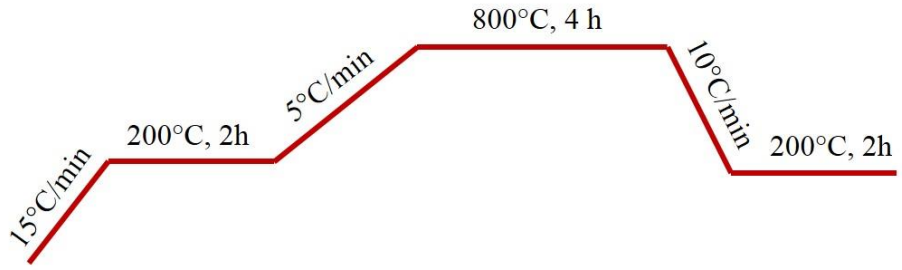


Figure 3.1: Temperature program for calcination.

After each calcination the calcined pellets were crushed into powder and planetary milled under the same conditions as for the homogenisation.

3.2.3 Sintering of the powder compacts

In order to prepare green pellets, 0.6 g of the calcined powder was compacted with a uniaxial press at 100 MPa into a cylindrical sample of ϕ = 8 mm using stearic acid to lubricate the pressing model. The samples were further cold isostatically pressed at 200 MPa (401C-0063, Autoclave Engineers, Erie, Pennsylvania, USA) and placed in a covered alumina crucible on a Pt foil. The samples were sintered at 1120°C and 1140°C for 2 h, according to the temperature program in Figure 3.2, in a tube furnace (PTF 16/75/450, Protherm, Ankara, Turkey).

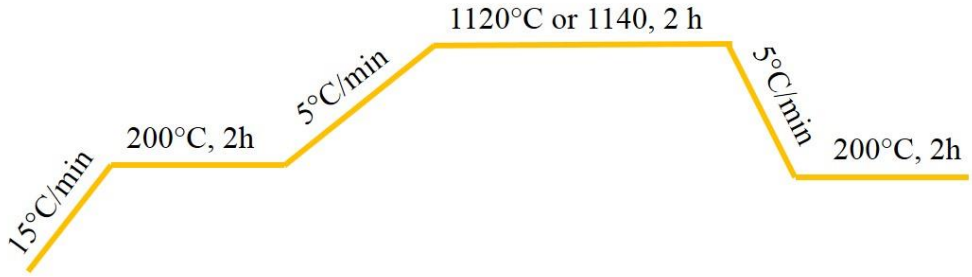


Figure 3.2: Temperature program for sintering.

3.3 Characterization of KNN and Sr-Doped KNN

3.3.1 Granulometric analysis

The granulometric analysis was performed in order to determine the particle size distribution of the reagents, homogenized mixtures and calcined powders.

The static, light-scattering granulometer (Microtrac S3500 Particle Size Analyzer, Montgomeryville, PA, USA) was employed for the measurements of the particle-size distribution of powders in 2-propanol. The particle-size area distributions are described with the d_{90} being the 90 % particle size limit, d_{50} being the median value or 50 % particle size limit and d_{10} being the 10 % particle size limit or with a graphical representation of the particle-size area distribution.

3.3.2 Powder specific surface area analysis (BET)

In addition to the granulometric analysis, the particle size distribution was complemented with the values of the specific surface area (SSA) for the milled Nb_2O_5 reagents.

The SSAs were analysed using the N_2 adsorption BET method (NOVA 2200E Quantachrome Instruments, Boynton Beach, FL, USA). Prior to the measurements the powder samples were degassed in a vacuum at 200 °C for 2 h in order to remove the adsorbed gases from the particle surfaces.

The BET equivalent particle diameters (d_{BET}) were calculated using the following equation:

$$d_{BET} = \frac{\Psi_A/\Psi_V}{s_M \cdot \rho_{abs}^t} \tag{3.1}$$

where S_M is the specific surface area, ρ_{abs}^t is the theoretical density of the measured powder, and ψ_A/ψ_V is the shape-factor ratio, for which a value of 6 was assumed [80].

3.3.3 Thermal analysis

Thermal analysis was used to determine the loss of ignition of the milled reagents to ensure the exact stoichiometric weighing. In case of the homogenized mixtures, the thermal analysis was used to study the solid-state reaction.

Thermogravimetry (TG), derivative thermogravimetry (DTG), differential thermal analysis (DTA) and evolved-gas analysis (EGA) were conducted on a Netzsch STA 409 C/CD (NETZSCH, Selb, Germany) coupled to a Balzers Quadstar 422 quadrupole mass spectrometer (Balzers, Balzers, Switzerland). Around 50 mg of the homogenized mixture was placed in Pt/Rh crucibles and TG, DTA and EGA were recorded with the following temperature program (please refer also to Figure 3.3): first, the sample was heated to 200°C with a 10°C/min heating rate and held for 3h in order to remove the water from the hygroscopic carbonate reagents. Then the sample was heated up to 750°C with a heating rate of 10°C/min to observe the reaction.

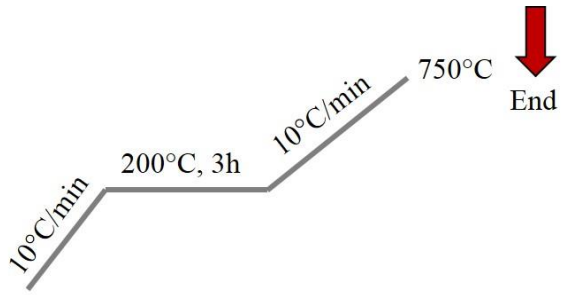


Figure 3.3: Temperature program for thermal analysis.

3.3.4 Dimensional changes during heating

All the samples were analysed by the optical dilatometer in the stage of the homogenized mixture in order to obtain the reaction curves, as well as after the second calcination, to obtain the sintering curves. For the reaction curve, 0.15 g of a powder was compacted with a uniaxial press at 50 MPa into a cylindrical sample of ϕ = 5 mm and for the sintering curve the 0.2 g of powder was compacted with a uniaxial press at 100 MPa into a cylindrical sample of ϕ = 6 mm and then with a cold isostatic press at 200 MPa, both using stearic acid to lubricate the pressing model.

The dimensional changes of the powder compacts during heating were recorded with an optical dilatometer (Leitz Version 1A, Leitz, Wetzlar, Germany) at a heating rate of 10 K/min. The dimensions of the samples were continuously measured from the digitalized images and the relative shrinkage ($\Delta l/l$) and the technical shrinkage ($(\Delta l/l)_{tech}$) were calculated with the following equations:

$$\frac{\Delta l}{l} = \frac{l_{RT} - l_T}{l_{RT}}.100 \tag{3.2}$$

$$\left(\frac{\Delta l}{l}\right)_{tech} = \left(\frac{\Delta l}{l}\right) + CTE.100.(T - RT) \tag{3.3}$$

where l_{RT} is the initial dimension of the sample at *RT*, l_T is the dimension of the sample at the selected temperature, CTE is the linear coefficient of thermal expansion, T is the selected temperature and RT is room temperature.

3.3.5 Density measurement

After the sintering, the relative densities of at least three pellets of each sample were calculated from the dimensions of the pellets and their masses, as well as measured by the Archimedes method.

The Archimedes density was calculated using the following equation:

$$\rho = \frac{m_1.\rho_{H2O}}{m_3 - m_2} \tag{3.4}$$

where the ρ is the measured density of the ceramic pellet, ρ_{H2O} is the density of the deionized water at the given temperature and masses m_1, m_2 and m_3 refer to the mass of the sintered pellet before the measurement, the mass of the pellet in the water and the mass of the pellet after it was taken out of water, respectively.

For the calculation of the relative density, the theoretical density of $K_{0.5}Na_{0.5}NbO_3$ = 4.51 g/cm^3 was used. This value was obtained from the Rietveld refinement of the monoclinic KNN unit cell [32].

3.3.6 X-ray diffraction

The phase composition and the structure of the as-received and milled reagents, the homogenized mixtures annealed to different temperatures, i.e., to 400, 450, 500, 550, 600, 650, 700, 750, 800, 850, and 950°C in a chamber furnace with a heating rate of 5 °C/min and the ceramic powders after calcinations and sintering, were determined by X-ray diffraction (XRD) analysis.

The XRD measurements were performed on a PANalytical X'Pert PRO diffractometer with a Cu Kα_1 radiation source and a Ge monochromator (PANalytical, Almelo, The Netherlands). The data were collected in the 2θ range from 10° to 90° with a step of 0.016°/100 s.

3.3.7 In situ high-temperature X-ray diffraction

The phase composition and structural changes of the homogenized mixtures upon heating were determined by *in-situ* high-temperature X-ray diffraction (HT-XRD) to complement the thermal analysis.

The HT-XRD was recorded at room temperature, 300, 400, 450, 500, 550, 600, 650, 700°C and once more at room temperature after cooling down. The measurements were performed on a PANalytical X'Pert PRO MPD diffractometer with a Cu Kα radiation source and a Ni-Kβ filter (PANalytical, Almelo, The Netherlands). The data were collected in the 2θ range from 20° to 40° with a step of 0.026°/100 s.

3.3.8 Synchrotron X-ray diffraction

The sintered ceramics pellets crushed into powders were also analysed by the synchrotron X-ray diffraction (synchrotron XRD).

The data was collected at the beam line ID22 in the European Synchrotron Radiation Facility, experiment MA2315, with a wavelength of 0.29501 Å. The wavelength was calibrated against a NIST 640c standard Si at room temperature. The beam was monochromated with a cryogenically cooled Si (111) double-crystal monochromator. The first monochromator crystal was side cooled by copper blocks, through which liquid nitrogen flowed. The second crystal was cooled by thermally conducting braids that linked to the first crystal, and had electrical heaters to maintain a stable temperature at –60 ± 0.05°C. A piezoelectric feedback system compensated for the changes in the Bragg angle of the second crystal caused by changes in the heat load on its supporting mechanics. Water-cooled slits defined the size of the incident beam on the monochromator, and of the monochromatic beam transmitted to the sample, with dimensions typically in the range 0.5–2.5 mm (horizontal) by 0.1–1.5 mm (vertical). A bank of nine detectors was scanned vertically to measure the diffracted intensity as a function of 2θ. Each detector was preceded by a Si (111) analyser crystal and the detector channels were approximately 2° apart. The powders were placed in a boron-glass capillary.

3.3.9 Rietveld refinement

A Rietveld refinement of the conventional XRD data was performed for all the sintered KNN and Sr-doped KNN samples to determine the changing unit cell parameters upon increasing Sr content.

The cell parameters were refined using JANA2006 software [81]. This software performs a full-pattern matching using the Rietveld method. The unit-cell parameters a, b, c and β were refined. A shift correction was made in order to obtain the correct zero position. The background was modelled using the Legendre polynom and the peaks' profiles were refined using a pseudo-Voigt function. The chosen space group for these refinements was monoclinic *P1m1* [32]. The weighed profile residual factor R_{wp} was used to express the quality of the fit. The factor is calculated according to Equations (3.5) and (3.6).

$$R_{wp} = \sqrt{\frac{\sum w_i (I_{i0} - I_{iC})^2}{\sum {w_i I_{i0}}^2}} \tag{3.5}$$

$$w_i = \frac{1}{I_{i0}} \tag{3.6}$$

where I_{i0} is the experimental intensity and I_{iC} is the calculated intensity.

The Rietveld refinement of the XRD data was also used to estimate the phase ratio of the Nb_2O_5 reagents after milling, which was used for the synthesis of KNN. This refinement was carried out using the Topas program. The scale factor and cell parameters were refined. The correction of the zero was performed. The background was modelled using the Legendre polynom. The peaks' profiles were fitted using the pseudo-Voigt function.

Rietveld refinement of the synchrotron XRD data was performed with a material analysis using diffraction (MAUD) code [82]. This software allows a Rietveld refinement, together with microstructure refinements. In this work, the microstructural features of the samples were evaluated with a simple isotropic model or the anisotropic Popa model for the strain, allowing a determination of the crystallite size and the root-mean-square (RMS) microstrain. The quality of the fit was evaluated with the weighted profile residual factor R_{wp}. The instrumental function was established by means of a defect-free standard SRM 660a, LaB_6.

3.3.10 Raman spectroscopy

The structural and phase analysis of the sintered KNN and Sr-doped KNN pellets was studied by Raman spectroscopy. The same samples were also studied by *in-situ* high-temperature Raman spectroscopy.

Composition-dependent Raman measurements were performed with a Horiba Jobin Yvon T64000 spectrometer (Horiba, Villeneuve d'Ascq, France) in the double subtractive configuration, adjusting the first intermediate slit so that the lowest measurable Raman shift value was ~25 cm^{-1}. Excitation was provided by a 514.5-nm Ar-ion laser Coherent Innova 400 (Coherent, Santa Clara, CA, USA). The laser light was focused on the sample surface by means of a long-working-distance, 50x objective lens with the numerical aperture NA = 0.5 (Olympus, Tokyo, Japan). Measurements were performed at room temperature and at 80 K in a liquid-nitrogen-cooled Linkam THMS600 stage (Linkam, Tadworth, UK).

Temperature-dependent measurements were performed in a high-intensity single-spectrograph Horiba Jobin Yvon LabRAM 300 (Horiba, Villeneuve d'Ascq, France) using a solid-state Nd:YAG laser working at 532.02 nm and a long-working-distance, 100x objective lens with NA = 0.8 (Olympus, Tokyo, Japan). The use of an edge filter allowed this equipment to reach Raman shift values as low as 80 cm^{-1}, but with a much higher throughput, thus enabling quicker measurements. The stage used here was a Linkam MDS600 heating-cooling unit (Linkam, Tadworth, UK). For both measurements the laser power was set to 3 mW at the sample surface. Spectra were collected using a multichannel, charge-coupled-device detector, which was liquid-nitrogen cooled in the case of the T64000, and Peltier-cooled in the case of the LabRAM 300.

3.3.11 Extended X-ray absorption fine structure

To investigate the local structure around the Sr dopant, the Sr K-edge extended X-ray absorption fine structure (EXAFS) spectra were recorded for the KNN, KNN-0.5% Sr, KNN-1% Sr and KNN-2% Sr.

The EXAFS of the thinned bulk ceramic samples were measured in transmission detection mode at the BM23 beamline of the European Synchrotron Radiation Facility (ESRF) in Grenoble, equipped with a Si (111) double-crystal monochromator with an approximately 2-eV resolution at 16 keV. The harmonics were effectively eliminated by using a flat, rhodium-coated mirror. The intensity of the incident and transmitted monochromatic beams was measured by three 30-cm-long ionization detectors filled with an Ar and He mixture at 2 bar, with the partial pressure of Ar being 220 mbar, 750 mbar, and 1600 mbar, respectively. The samples with a total absorption thickness of about 2 above the Sr K-edge were mounted between the first and second ionization detectors. The X-ray absorptions were measured within the interval from –250 eV to +1000 eV relative to the Sr K-edge (16111 eV) with equidistant k-steps of 0.03 Å−1 in the EXAFS region, and an integration time of 1 s/step. The Sr K-edge jump was between 0.04 and 0.14, depending on the relative amount of Sr in the samples. The exact energy calibration was established with

simultaneous absorption measurements on the $SrTiO_3$ reference sample placed between the second and third ionization chambers.

The EXAFS spectra were analysed with the IIFFEFIT [83] and FEFF6 [84] program codes.

3.3.12 Microstructural analysis by scanning electron microscopy

The powder morphology of the reagents before and after milling and of the calcined powders, were analysed with the scanning electron microscope (SEM). The microstructures together with the chemical compositions of the polished pellets of the sintered ceramic pellets were analysed with SEM with energy-dispersive X-ray spectroscopy (EDXS) and wavelength-dispersive X-ray spectroscopy (WDXS). Samples of the sintered ceramic pellets were also fractured and thermally etched and imaged by SEM.

The samples were analysed using a Jeol JSM-7600F field-emission SEM (Jeol, Tokyo, Japan) equipped with INCA Oxford 350 EDS SDD (20 mm^2) EDXS and INCA Wave 500 spectrometer WDXS detectors (Oxford Instruments, Abingdon, United Kingdom). The standard conditions for EDXS and WDXS quantitative analyses were at WD = 15 mm and an accelerating voltage of 15 keV. Imaging was performed with the secondary electrons in-lens detector (SEI), the low-energy secondary electrons in-lens detector (LEI) or the backscattered-electrons retractable detector (BSE).

For the SEM analysis of the powders, the powders were applied on an adhesive carbon-tape and coated with carbon using a Balzers SCD 050 sputter coater (Balzers, Balzers, Liechtenstein). In the case of the sintered ceramics, the samples were cut with a diamond wire saw (Precision wire saw 3241, Well Diamond Wire Saws, Inc., Norcross, Georgia, USA), mounted in epoxy, ground on the SiC papers with a gradation of 800, 1200, 2400 and 4000 and then polished with diamond pastes with 3-µm- and 0.25-µm-sized particles. Thermal etching of the ceramics was carried out at a temperature that was 100°C lower than the sintering temperature. Prior to the analysis, the samples were coated with a 4-nm-thick carbon layer in a precision etching coating system PECS 682 (Gatan, Pleasanton, CA, USA).

The grain-size evaluation was performed for the KNN, KNN-0.5% Sr, KNN-1% Sr, KNN-2% Sr samples from SEM micrographs of the microstructures, which were digitalized and processed with the Image Tool software [85] and the grain size was evaluated on more than 500 grains and expressed as the mean Feret diameter.

3.3.13 Structural analysis with transmission electron microscopy

The morphology, local crystal structure and/or phase and chemical composition, of the Nb_2O_5 reagent powders, calcined powders and sintered ceramics pellets, were investigated using transmission electron microscopy (TEM) techniques.

Two microscopes were used for the analysis: Jeol 2010F (Jeol, Tokyo, Japan) equipped with ISIS 300 EDS (Oxford Instruments, Abingdon, United Kingdom) EDXS detector, further denoted as TEM and the Cs-corrected Jeol ARM 200 CF STEM (Jeol, Tokyo, Japan), further denoted as ARM, equipped with high-angle annular dark-field (HAADF) and annular bright-field (ABF) detectors used simultaneously at 68–180 and 10–16 mrad collection semi-angles, respectively. The TEM was used for the imaging and EDXS, while the ARM was used for the imaging on the atomic level, atom spacing measurements and the EDXS analysis, performed with the Jeol EDXS Centurio 100 mm^2 SDD detector. Both microscopes were operated at 200 kV.

The samples for the TEM analysis in the form of a ceramic pellet were cut into discs of 600-µm thickness on the precision wire saw and then a disc of 3 mm diameter was cut out on a Sonicut™ ultrasonic cutter (Model 380, Southbay technology, San Clemente, CA, USA). The 3-mm-disc was ground to a 100-µm thickness with the disc grinder (Model 623, Gatan, Pleasanton, CA, USA) on the grinding SiC papers with gradations of 800, 1200, 2400 and 4000 and then polished with diamond pastes with 3-µm- and 0.25-µm-sized particles. The resulting polished discs were then dimple ground on a dimple grinder, model 656 (Gatan, Pleasanton, CA, USA) to a 15–20-µm thickness and ion milled with Ar on the Gatan PIPS 691 (Gatan, Pleasanton, CA, USA) using accelerating voltages of 3.5 kV for etching until a hole appeared, and then 0.5 kV for cleaning.

The samples in the form of a powder were viewed on a copper grid (SPI Supplies, West Chester PA, USA).

The micrographs made with the TEM were used for the grain size evaluation of the KNN-6% Sr and KNN-8% Sr. The micrographs were digitized and processed with the ImageTool software [85], and the grain-size was analysed based on about 50 grains and expressed as the mean Feret diameter.

Chapter 4

Results and Discussion

4.1 The Influence of the Niobium Pentoxide Reagent on the KNN Solid-State Synthesis and Sintering

In the first part of this dissertation, the influence of the polymorphic form of Nb_2O_5 on the solid-state synthesis of KNN is studied. Two KNN batches are prepared by identical procedures using two different polymorphic forms of Nb_2O_5. The course of the reaction of the two corresponding homogenized mixtures is investigated. The reasons for the different reactivity of the two Nb_2O_5 polymorphs with the alkaline carbonates during solid-state synthesis and the sintering behaviour of the resulting ceramics are discussed.

4.1.1 Reagents preparation

All the reagents were dried, ball milled for 4 h in a planetary mill at 175 rpm in acetone dried, sieved and dried before weighing (for detailed conditions, please refer to Materials and Methods), to decrease the particle size of the powder and to improve the uniformity of the particle size distribution. Below, the reagents are characterized before and after the milling procedure.

4.1.1.1 K_2CO_3 and Na_2CO_3 reagents

Figure 4.1 shows the XRD spectra of the as-received K_2CO_3 and the K_2CO_3 after milling. The whole XRD patterns of both the K_2CO_3 before and after milling can be indexed with two phases: $K_2CO_3.1.5H_2O$ (ICDD, PDF: 01-073-0470) and $KHCO_3.1.5H_2O$ (ICDD, PDF: 00-020-0886).

The milling of the K_2CO_3 powder results in peak broadening. The K_2CO_3 as milled and as received also have different content of the two phases, please refer to the peak at 31.7 °2θ (marked with a blue arrow in Figure 4.1), which is one of the most intense peaks of the $KHCO_3.1.5H_2O$ phase, and its intensity is ~30% higher in the K_2CO_3 – milled, compared to the K_2CO_3 – as received.

According to the reference pattern for $K_2CO_3.1.5H_2O$, the three most intense peaks, i.e., the ones at 32.198, 32.356 and 32.627 °2θ, have the following intensities: 73 %, 92 % and 100 %, respectively. The intensities of these peaks in the spectrum of K_2CO_3–milled are roughly comparable with the reference pattern, while the K_2CO_3 – as received has a significantly different intensity profile. This could be attributed to the preferential orientation due to the large crystals of the order of hundreds of μm before the powder was milled (see Figure 4.3, granulometric analysis of K_2CO_3 – as received).

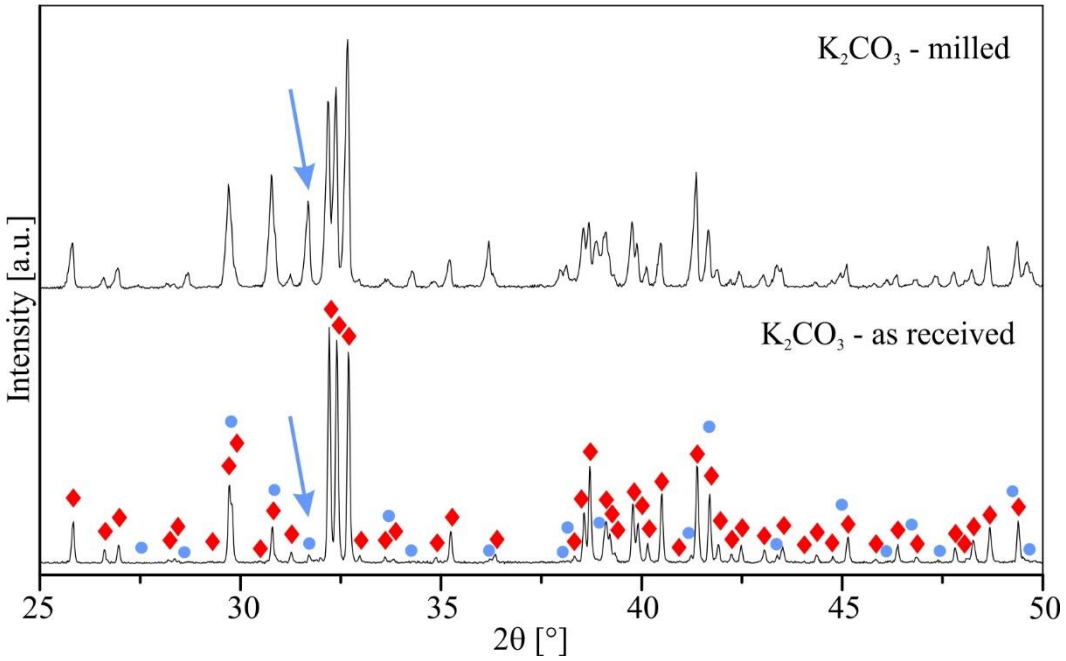


Figure 4.1: XRD spectra of K_2CO_3 before and after milling. ♦ marks the peaks of $K_2CO_3.1.5H_2O$ (ICDD, PDF: 01-073-0470), • marks the peaks of the $KHCO_3.1.5H_2O$ (ICDD, PDF: 00-020-0886).

The above results suggest that during the measurement part of the K_2CO_3 powder reacted with the atmospheric H_2O and CO_2 to form the $KHCO_3$ and the K_2CO_3 and $KHCO_3$ readily formed hydrates with the atmospheric humidity. The fraction of $KHCO_3.1.5H_2O$ increases after the milling procedure (see Figure 4.1, blue arrows). The reason might be due to the increased surface area of the powder after milling, which allows more K_2CO_3 to form the $KHCO_3.1.5H_2O$.

Figure 4.2 shows the XRD spectra of the as-received Na_2CO_3 and the Na_2CO_3 after milling. The main peaks correspond to the Na_2CO_3 (ICDD, PDF: 00-019-1130) in both powders. Also, the $Na_2CO_3.H_2O$ (ICDD, PDF: 00-008-0448) peaks can be identified in the as-received Na_2CO_3 powder. The milling of the as-received Na_2CO_3 powder results in a decrease of the peaks' intensity together with the peak broadening and the peaks of $Na_2CO_3.H_2O$ become barely identifiable.

The XRD spectra of the Na_2CO_3 before and after milling show that the milling results mainly in the peak broadening, which might be due to the decrease of the crystallite size and/or the increase of the microstrain due to the mechanical impact during milling. However, the degree of hydration does not seem to undergo any significant change after milling and more than the milling is related to the specific conditions during the XRD measurement, like atmospheric humidity or time of exposure to the laboratory air.

Overall, Na_2CO_3 seems to be less sensitive to humidity than K_2CO_3.

Figure 4.3, on the left, presents the granulometric analysis of K_2CO_3 and Na_2CO_3 before and after milling. Milling of both powders results in a decreased particle size and eliminating the particles above 20 µm. The d_{50} values are 4.40 µm and 2.58 µm, for K_2CO_3 and Na_2CO_3, respectively. The SEM micrographs (Figure 4.3, on the right) show milled K_2CO_3 and Na_2CO_3 powders. For both powders, the particles have comparable sizes, as determined by the granulometric analysis.

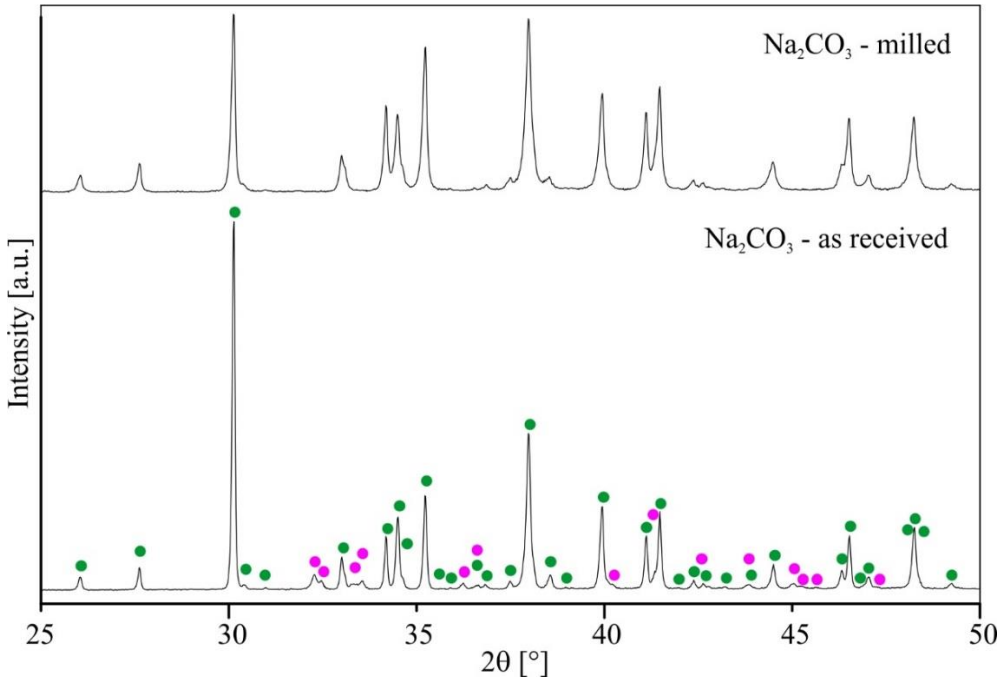


Figure 4.2: XRD spectra of Na_2CO_3 before and after milling. • marks the peaks of Na_2CO_3 (ICDD, PDF: 00-019-1130), • marks the peaks of the $Na_2CO_3.H_2O$ (ICDD, PDF: 00-008-0448).

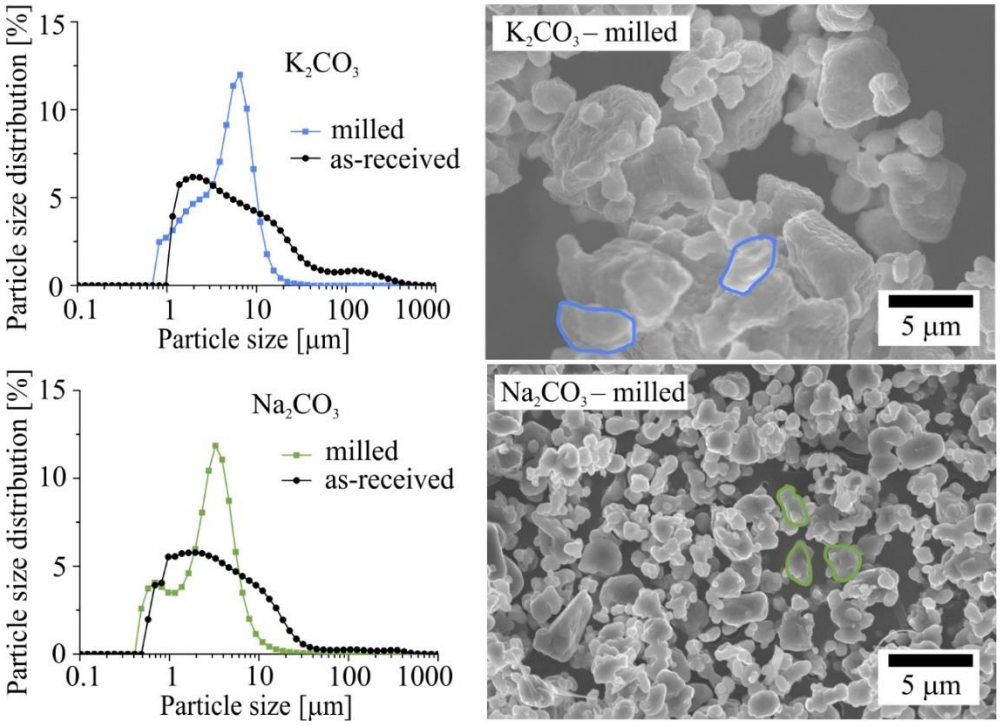


Figure 4.3: K_2CO_3 and Na_2CO_3 powders. Granulometric analysis of the K_2CO_3 and Na_2CO_3 before and after the milling and SEM SEI micrographs of the milled K_2CO_3 and Na_2CO_3 powders. Examples of particles corresponding to the d_{50} values are marked on the SEM micrographs.

4.1.1.2 **Nb_2O_5 reagents**

Two different Nb_2O_5 were used for the synthesis of two batches of KNN. One was from Sigma Aldrich and the other was from Alfa Aesar, as explained in Materials and Methods. Figure 4.4 shows the XRD pattern of the as-received Nb_2O_5 reagents.

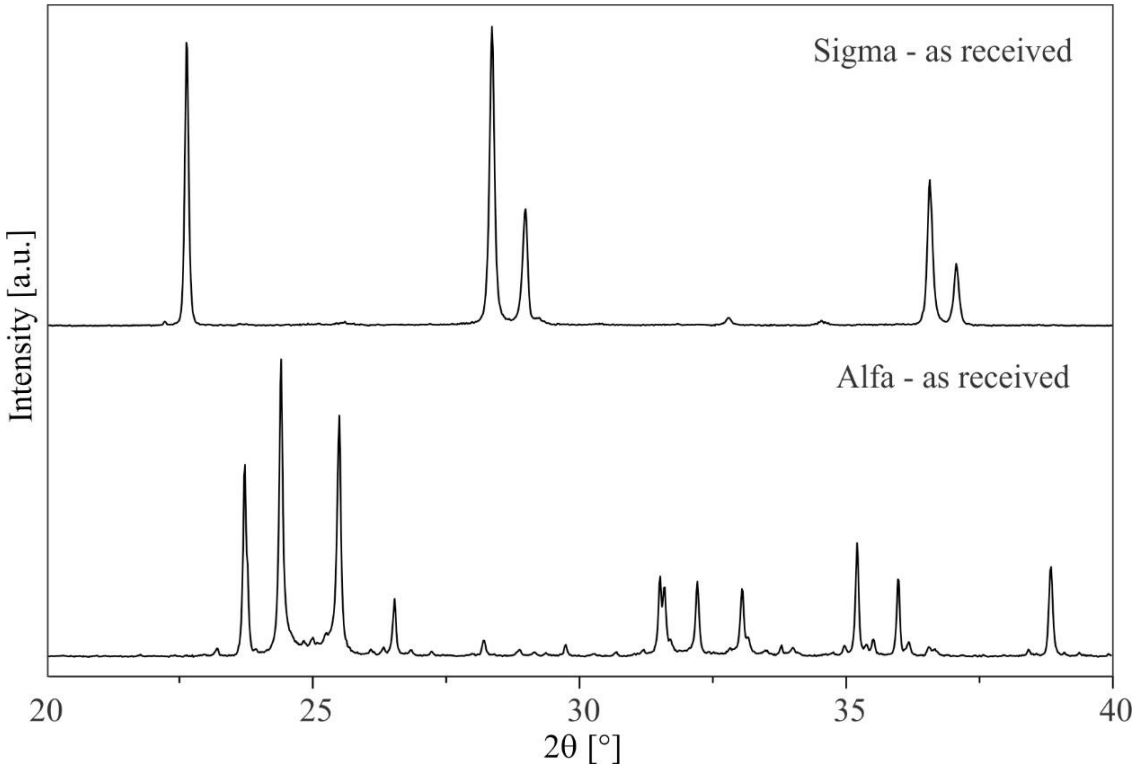


Figure 4.4: XRD patterns of the as-received Nb_2O_5 reagents from two different producers.

As it is evident from Figure 4.4, each of the Nb_2O_5 has a different crystalline phase, i.e., a crystal polymorph. The XRD pattern of the Nb_2O_5 from Sigma can be indexed to the orthorhombic unit cell (ICDD, PDF: 01-071-0336) and is further referred to as Nb_2O_5-ortho, while the other Nb_2O_5 can be indexed to the monoclinic unit cell (ICDD, PDF: 00-037-1468) and is further referred to as Nb_2O_5-mono.

Besides the phase composition, the two Nb_2O_5 also had different particle size distribution: as it is seen in Figure 4.5, the as-received Nb_2O_5-ortho consists of very fine particles (d_{50} = 0.48 µm) with a small quantity of larger particles sized between 1 and 10 µm, while the as-received Nb_2O_5-mono contains large particles of a size of several microns and overall has a bimodal distribution and a larger median particle size (d_{50} = 0.70 µm), compared to the Nb_2O_5-ortho.

To obtain a similar and narrower particle size distribution of the two different Nb_2O_5 reagents, both powders were milled in a planetary mill. As is visible in Figure 4.6, milling of the Nb_2O_5-ortho results in the elimination of the larger particles and a decreased mean particle diameter (d_{50} = 0.33 µm). Milling of the Nb_2O_5-mono successfully eliminated the larger particles and also decreased the mean particle size to d_{50} = 0.40 µm. The particle morphology of both Nb_2O_5 powders, as seen on the SEM micrographs in Figure 4.6, confirmed the results of the granulometric analysis and showed comparable particle size distributions for the two Nb_2O_5 after milling.

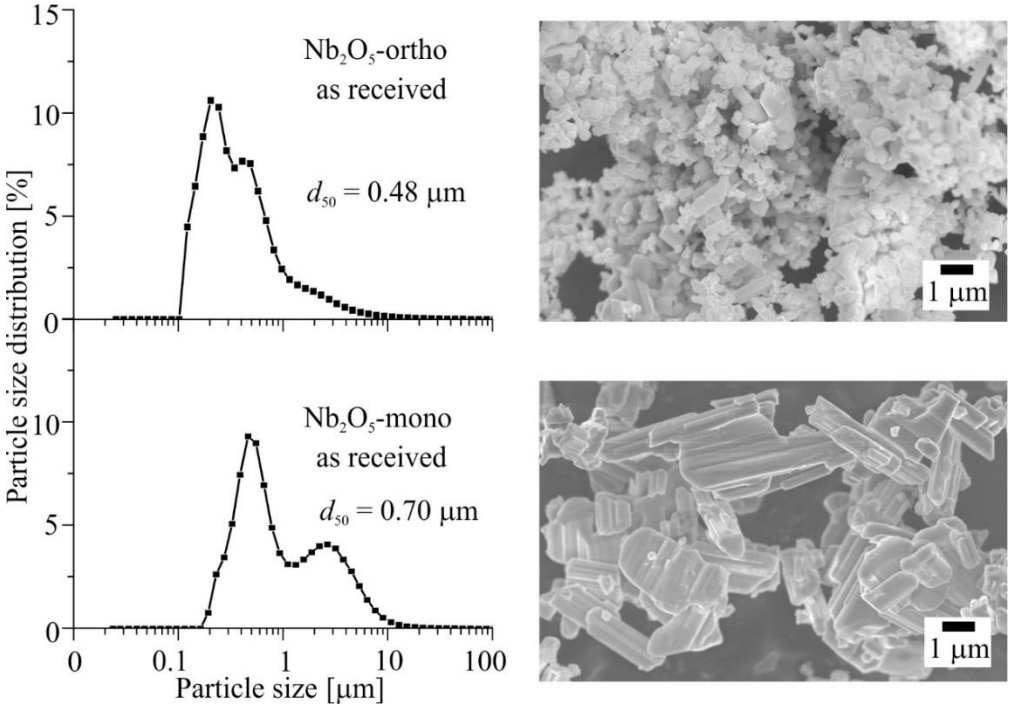


Figure 4.5: The as-received Nb_2O_5 reagents. Granulometric analysis and SEM SEI micrographs of the as-received Nb_2O_5-ortho and -mono powders.

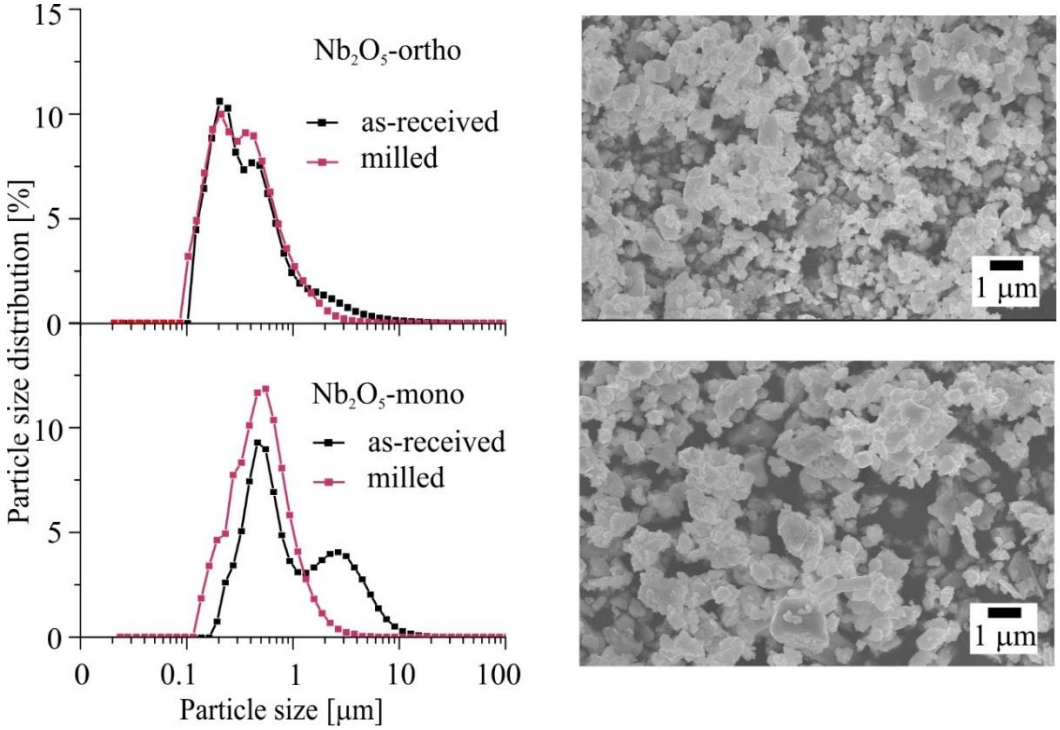


Figure 4.6: The Nb_2O_5 reagents before and after milling. Granulometric analysis of the milled Nb_2O_5-ortho and -mono after milling compared to the as-received powders and SEM SEI micrographs of the milled Nb_2O_5-ortho and –mono. The particle size distributions from Figure 4.5 are shown for easier comparison.

Figure 4.7 presents the XRD patterns of the Nb_2O_5 powders before and after milling. Milling of the Nb_2O_5 results in a broadening of the peaks in both Nb_2O_5-ortho and -mono powders (see Figure 4.7). The broadening is probably caused by micro-strains introduced by the mechanical stress during milling and/or by a crystallite-size decrease to the nanometre range. Also, in the milled Nb_2O_5-mono, new broad peaks are observed at 22.6, 28.5 and 36.7 °2θ. These peaks can be indexed according to the orthorhombic Nb_2O_5 unit cell (ICDD, PDF: 01-071-0336).

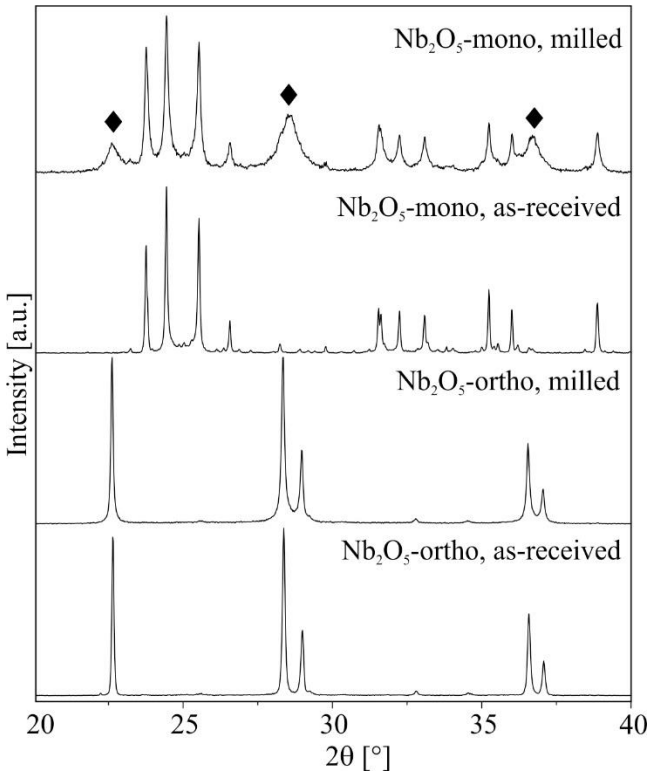


Figure 4.7: XRD patterns of Nb_2O_5 reagents. From bottom: Nb_2O_5-ortho as-received and milled, Nb_2O_5-mono as-received and milled. Peaks marked with ♦ denote the newly introduced orthorhombic phase.

The presence of both orthorhombic and monoclinic phases in the milled Nb_2O_5-mono was confirmed by the XRD spectra Rietveld refinement. Orthorhombic (ICSD 1840) and monoclinic (ICSD 16605) Nb_2O_5 were used as model structures for the refinement. The milled Nb_2O_5-mono contained 47% of the orthorhombic and 53% of the monoclinic phase.

In their study of the Nb_2O_5 polymorphs, Frevel and Rinn [86] reported a new Nb_2O_5 phase with a high surface area, which they described as pseudo-hexagonal. This phase converted to the orthorhombic phase after annealing at 700°C for 16 h. Later, Holtzberg et al. [26] confirmed that this phase was actually an orthorhombic phase with poor crystallinity. This is in agreement with our results (Figure 4.7: Nb_2O_5-mono, milled).

As reported in the study by Holtzberg et al. [26], the phase transformation of the orthorhombic Nb_2O_5 to its high-temperature-stable monoclinic polymorph at 830°C is not reversible. Rojac in his PhD thesis [87] confirmed the orthorhombic-to-monoclinic phase transition's irreversibility: cooling of the monoclinic Nb_2O_5 to room temperature did not result in its transformation back to the orthorhombic form. In any case, Rojac [87] observed a complete transformation of the monoclinic Nb_2O_5 to the orthorhombic polymorph after high-energy milling a sample for 10 hours. This is consistent with what is described in Figure 4.7. Rojac [87] explained the Nb_2O_5 monoclinic-to-orthorhombic transformation by the increased pressures of the collisions during the high-energy milling. Senna and Kuno [88] achieved a mechanochemical polymorphic transformation of PbO in the form of massicot to litharge by isothermal, wet ball-milling. They also explained the transformation in terms of the mechanical effects. It can therefore be assumed that similar mechanical effects during wet planetary milling caused the partial phase transformation of the Nb_2O_5-mono to orthorhombic.

Additional experiments were performed to understand the differences between the milled Nb_2O_5-ortho and Nb_2O_5-mono powders. Both powders were investigated using the N_2 adsorption BET method. The specific surface areas (SSA) were 8.0(2) m^2/g and 7.2(2) m^2/g, for the Nb_2O_5-ortho and Nb_2O_5-mono, respectively. Based on Equation (3.1) and the theoretical densities for Nb_2O_5-ortho being 5.2 g/cm^3 as for ICDD, PDF: 01-071-0336 and Nb_2O_5-mono being 4.6 g/cm^3 as for ICDD, PDF: 00-037-1468, the SSA values correspond to a d_{BET} particle size of about 145 nm and 180 nm for the Nb_2O_5-ortho and –mono, respectively.

To investigate the morphology of the particles of the milled Nb_2O_5 reagents, a TEM analysis was performed. The TEM micrographs in Figure 4.8, show differences in the morphology of the Nb_2O_5-ortho and Nb_2O_5-mono particles.

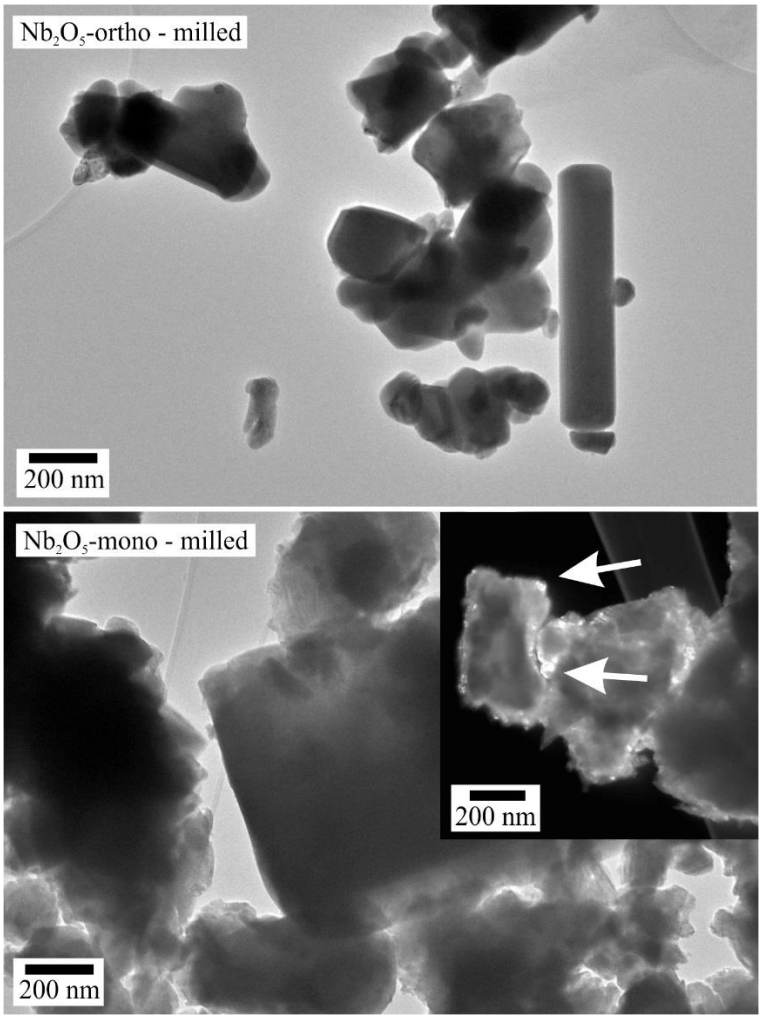


Figure 4.8: TEM of the milled Nb_2O_5 reagents. Bright-field TEM image of the Nb_2O_5-ortho and Nb_2O_5-mono powders after milling; inset of Nb_2O_5-mono showing dark-field image, arrows pointing at the small crystals on the surface.

The milled Nb_2O_5-ortho particles appear to be smooth and regular, while the milled Nb_2O_5-mono have a ripped-like and rough, surface. A dark-field TEM micrograph in the inset of Figure 4.8, Nb_2O_5-mono - milled, shows the presence of tiny crystals on the surface of the larger particles of the milled Nb_2O_5-mono.

A detailed investigation of the milled Nb_2O_5-mono powder was performed with high-resolution TEM (HRTEM) (Figure 4.9). The micrograph shows a relatively large particle with tens-of-nm-sized nanocrystals on its surface. The insets in Figure 4.9 present the diffraction spots obtained with a fast Fourier transform (FFT) for the nanocrystals (Figure 4.9 – inset on the left) corresponding to the orthorhombic (001) plane reflections (ICDD, PDF: 01-071-0336) and the

diffraction spots from the large particle (inset on the right) corresponding to the monoclinic (-101) plane reflections (ICDD, PDF: 00-037-1468).

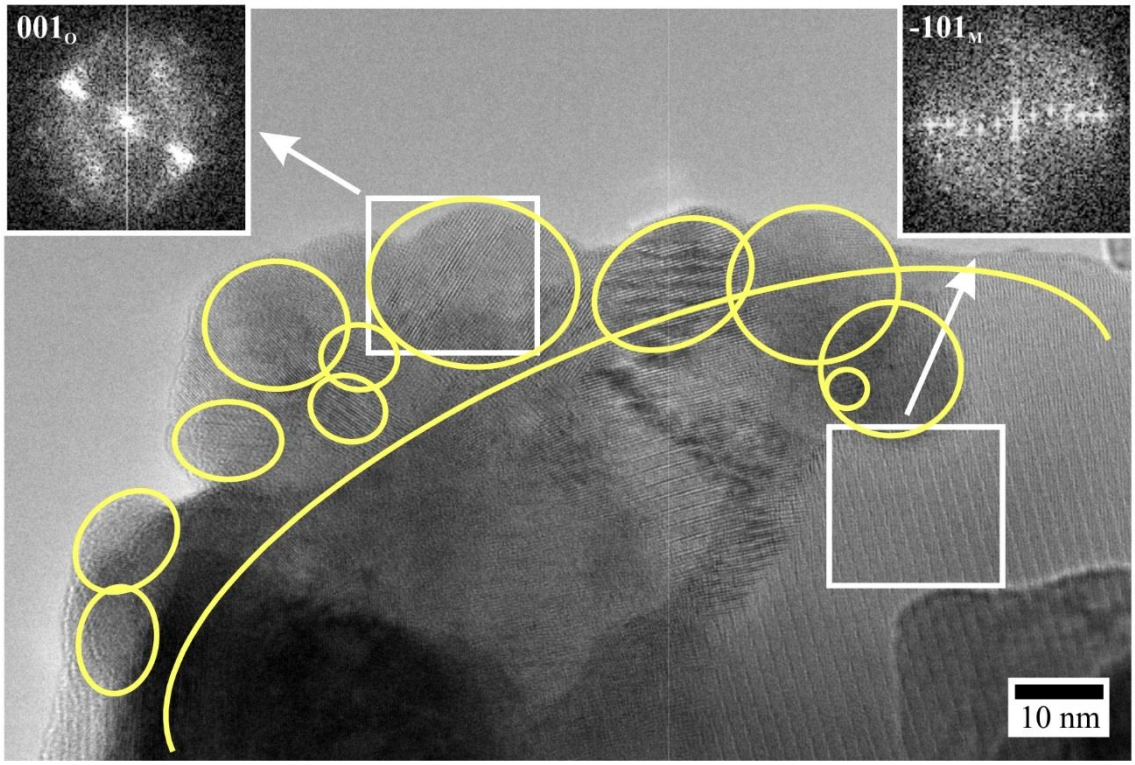


Figure 4.9: HRTEM image of the milled Nb_2O_5-mono. The nanoparticles on the surface of a larger particle are marked yellow. Insets show FFTs of the selected areas.

The TEM analysis results confirm the presence of two phases in the milled Nb_2O_5-mono powder, i.e., monoclinic and orthorhombic. This result supports the findings from the XRD analysis in Figure 4.7, Nb_2O_5.mono, milled. The TEM analysis further revealed, that the broader XRD peaks of the orthorhombic phase introduced by milling belong to the nanocrystals with orthorhombic syngony, which are attached to the surface of the relatively larger monoclinic crystals.

4.1.2 Synthesis of KNN

In the subsequent text, the homogenized mixtures to form KNN are discussed. The mixture prepared from the milled Nb_2O_5-ortho and the milled potassium and sodium carbonates is denoted as homogenized KNN-ortho, while the mixture prepared from the milled Nb_2O_5-mono and the milled potassium and sodium carbonates is denoted as homogenized KNN-mono. The powders after both calcinations are denoted as calcined KNN-ortho and calcined KNN-mono.

4.1.2.1 Reaction curves

The changes in the diameter of a pellet made from the homogenized KNN-ortho and -mono powders with increasing temperature were recorded with the optical dilatometer, to study the reaction curves of the two powder compacts.

As is visible in Figure 4.10a, blue curve, the homogenized KNN-ortho pellet starts expanding at 400°C with the expansion rate starting to increase at 490°C to reach a maximum expansion of 15.5% at 620°C. The shrinkage occurs in two steps that are divided by a plateau, i.e., the first shrinkage step is between 900 to 950°C and the second is between 1050°C and 1140°C. At 1140°C, the expansion of the pellet is observed on the curve, which is attributed to the pellet melting. The observed melting temperature is in agreement with the one typically reported for KNN, i.e., 1140°C [7, 12].

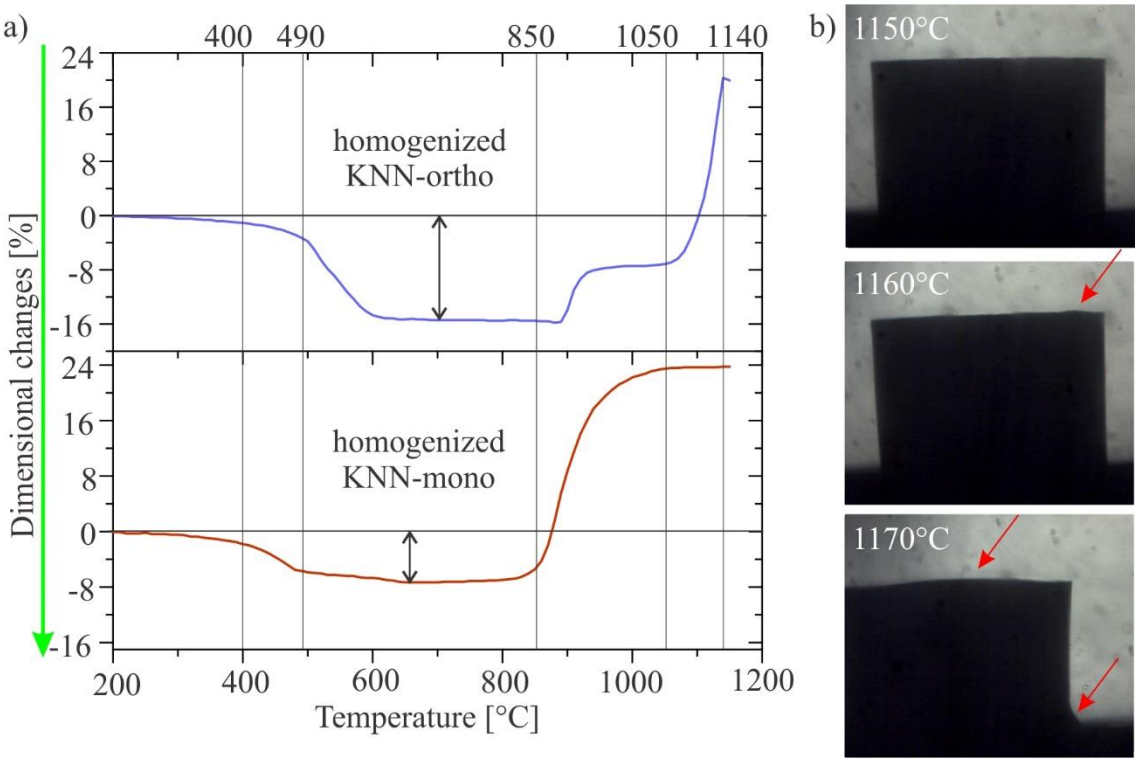


Figure 4.10: Reaction curves. a) dimensional changes with temperature of the homogenized KNN-ortho and homogenized KNN-mono powder compact, green arrow marks the direction of expansion b) images of the homogenized KNN-mono powder compact near the melting point, arrows mark the shape deformations due to melting.

The homogenized KNN-mono pellet (Figure 4.10a, red curve) starts expanding below 400°C with a relatively high rate. At 490°C the rate of expansion diminishes and the maximum expansion of 7.3% is reached at 640°C. The homogenized KNN-mono therefore expands less during the reaction than the homogenized KNN-ortho. The homogenized KNN-mono pellet shrinks in the temperature interval between 850°C and 1080°C. After 1080°C, a plateau is observed. However, emerging bubbles on the pellet's surface (Figure 4.10b, 1160°C) and spilling

pellet bottom (Figure 4.10b, 1170°C) are observed with the optical dilatometer after 1150°C, which is attributed to the start of the pellet melting at 1160°C.

The results in Figure 4.10 show that the homogenized KNN-mono expands less during the reaction compared to the homogenized KNN-ortho. The shrinking starts at a 50°C and finishes at a 60°C lower temperature than for the homogenized KNN-ortho. And finally, the homogenized KNN-mono melts at a 20°C higher temperature than KNN [7, 12].

As known from the literature, the reaction of the $K_2CO_3/Na_2CO_3/Nb_2O_5$ system proceeds by carbonates decomposition, which is accompanied by the evolution of CO_2 [19, 20]. The solid-state synthesis of a material is accompanied by the volume changes due to the formation of a reaction-shell-like layer of a product on the particle surface, as described by Chandratreya et al. in a study of the $PbTiO_3$ reaction [89], into which the other reactants diffuse, as previously reported for the $BaTiO_3$ system [18].

Considering a perfectly round, dense Nb_2O_5 particle, which reacts completely to form $K_{0.5}Na_{0.5}NbO_3$ and if it is taken that the reaction of 1 mole of Nb_2O_5 forms 2 moles of $K_{0.5}Na_{0.5}NbO_3$, the theoretical expansion during the reaction is calculated based on Equations (4.1) and (4.2):

$$\frac{\Delta r}{r} = \sqrt[3]{\frac{V(\mathrm{K_{0.5}Na_{0.5}NbO_3})}{V(\mathrm{Nb_2O_5})}} - 1 = \sqrt[3]{\frac{2V_{M(\mathrm{K_{0.5}Na_{0.5}NbO_3})}}{V_M(\mathrm{Nb_2O_5})}} - 1 \tag{4.1}$$

$$V_M = \frac{M}{\rho} \tag{4.2}$$

where V_M is the molar volume [cm^3/mol], M is the molecular weight [g/mol], ρ is the density [g/cm^3], and r is the radius of the sphere

ρ (Nb_2O_5-ortho) = 5.2 g/cm^3 (JCPDS: 01-071-0336), ρ (Nb_2O_5-mono) = 4.6 g/cm^3 (JCPDS: 00-037-1468), ρ ($K_{0.5}Na_{0.5}NbO_3$) = 4.51 g/cm^3

The KNN-ortho should theoretically expand by 14.5%. If we take into account the ratio of the orthorhombic and monoclinic phases in the milled Nb_2O_5-mono reagent, which were obtained by Rietveld refinement, the expansion for the KNN-mono should be 11.9%. The experimentally observed maximum expansions are 15.5% and 7.3% for the homogenized KNN-ortho and the homogenized KNN-mono, respectively. The slight difference in the theoretical and measured maximum expansion values for KNN-ortho can be justified by the gas evolution and because the compact is not perfectly dense. However, the actual expansion of the homogenized KNN-mono is significantly lower than its theoretical value. This suggests the formation of phases other than the stoichiometric $K_{0.5}Na_{0.5}NbO_3$, like $NaNbO_3$, which has a theoretical expansion of 7.6%. Based on the $KNbO_3$-$NaNbO_3$ phase diagram [7], the presence of such a phase also contributes to the higher melting point of the homogenized KNN-mono, as was observed in Figure 4.10.

4.1.2.2 **Thermal analysis**

The results from the TG, DTG and DTA analyses of the homogenized KNN-ortho and -mono are presented in Figure 4.11.

The KNN-ortho (Figure 4.11, KNN-ortho) loses 11.48 % of its mass between room temperature and 630°C in two steps, which is evident from the two DTG peaks, i.e., at 485°C and at 565°C. The mass loss is accompanied by a remarkable exothermic peak on the DTA curve at 500°C.

The KNN-mono (Figure 4.11: KNN-mono) loses 11.47 % of its mass also in two steps between the room temperature and 690°C. The first DTG is at 465°C and the second at 625°C. Similar to the KNN-ortho, a DTA exothermic peak appears at 500°C.

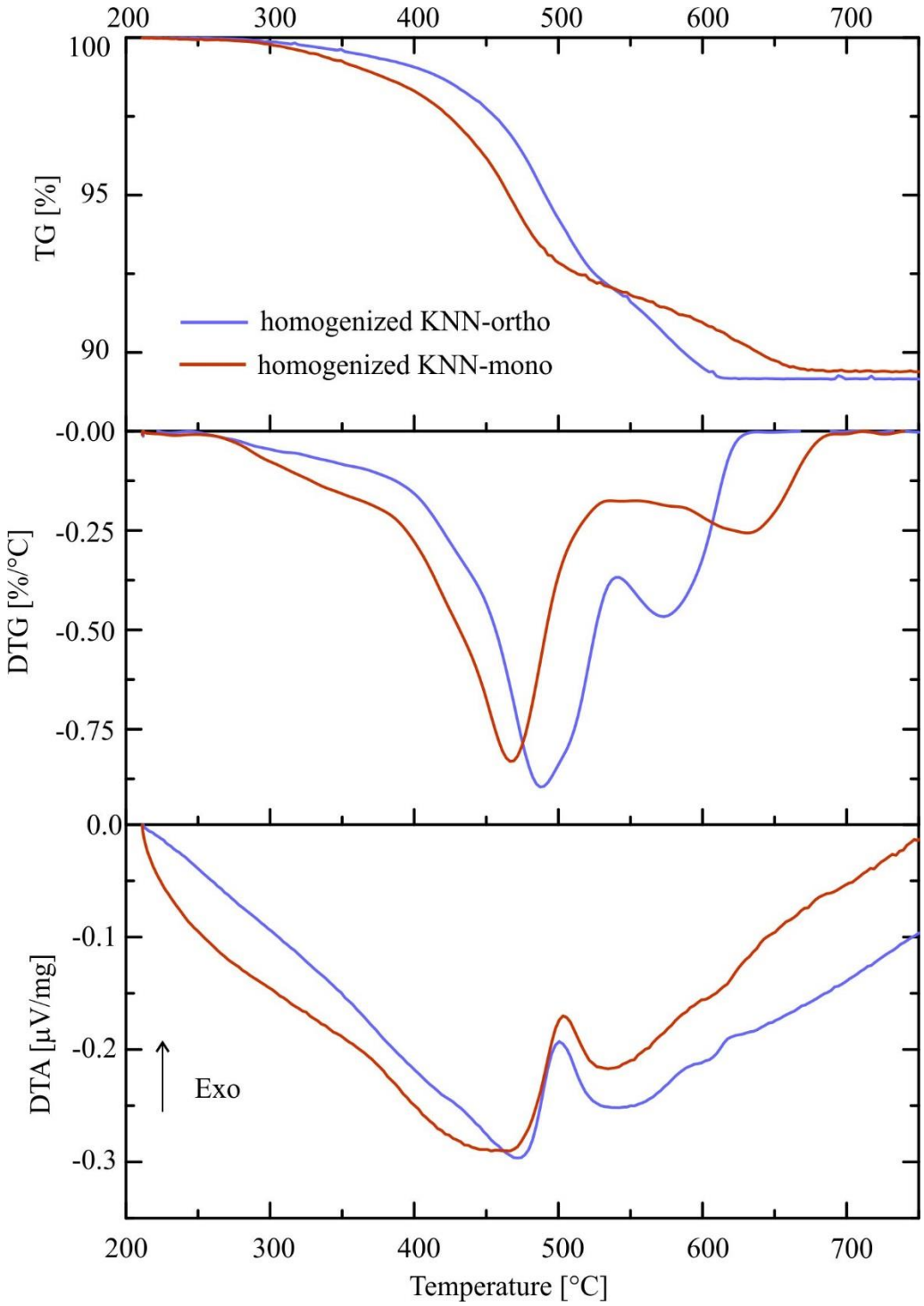


Figure 4.11: TG, DTG and DTA curves of the homogenized KNN-ortho and KNN-mono.

Table 4.1: Summary of some TG, DTG and DTA values for the homogenized KNN-ortho and homogenized KNN-mono.

	TG		DTG		DTA
	Total mass loss [%]	End of mass loss [°C]	1st DTG peak [°C]	2nd DTG peak [°C]	Exothermic peak [°C]
KNN-ortho	11.48	630	485	565	500
KNN-mono	11.47	690	465	625	500

The theoretical mass loss of the evolved CO_2 during the KNN solid-state synthesis is 11.34 %. The observed total mass losses presented in Table 4.1 are comparable to the theoretical one for both studied powders. The mass-loss temperature interval observed for the homogenized KNN-mono (see Figure 4.11), i.e., 250–690°C, is broader compared to the homogenized KNN-ortho, which is 250–630°C. The start of the mass loss for the homogenized KNN-mono is identical, but the course is different: the first KNN-mono DTG peak is observed at a 20°C lower and the second DTG peak at a 60°C higher temperature than for the homogenized KNN-ortho.

4.1.2.3 Annealing of the homogenized mixtures

To analyse the phases forming during the reaction, homogenized KNN-ortho and -mono were annealed at different temperatures and their XRD patterns were recorded (see Figure 4.12). The XRD patterns at 400°C for both homogenized KNN-ortho and – mono show the unreacted, homogenized mixtures of K_2CO_3, Na_2CO_3 and the corresponding Nb_2O_5.

Most of the visible peaks in Figure 4.12, homogenized KNN-ortho, 400°C, can be indexed as the orthorhombic Nb_2O_5 (JCPDS: 01-071-0336). At 450°C, the perovskite phase appears and then grows at the expense of the Nb_2O_5, which is demonstrated as the increasing intensity of the perovskite peaks and the decreasing intensity of the orthorhombic Nb_2O_5 peaks with the increasing temperature, until there is no more Nb_2O_5 left at 650°C. The positions of the XRD peaks correspond to the A-site homogeneous KNN [32].

In the case of the unreacted homogenized KNN-mono (Figure 4.12, homogenized KNN-mono, 400°C), the monoclinic Nb_2O_5 peaks (JCPDS: 00-037-1468) and the broad orthorhombic Nb_2O_5 peaks (JCPDS: 01-071-0336) can be identified. Although the perovskite phase appears at 450°C, as well as in the homogenized KNN-ortho, at 500°C, besides the main perovskite peak at 32°2θ, additional peaks are detected in the KNN-mono. The peak shapes change with the increasing temperature and at 650°C there is a clear shoulder on the main perovskite peak.

The Figure 4.13 shows the XRD patterns of the calcined KNN-ortho and –mono. The calcined KNN-ortho spectra (Figure 4.13a, calcined KNN-ortho) correspond to the KNN monoclinic perovskite unit cell [32]. However, in the XRD spectra of the calcined KNN-mono, additional shoulders at higher °2θ are seen on the XRD pattern (Figure 4.13, calcined KNN-mono, marked with arrows) in addition to the expected $K_{0.5}Na_{0.5}NbO_3$ perovskite peaks. The resulting shoulders are consistent with the peak shape at 32°2θ observed in Figure 4.12, homogenized KNN-mono, 650°C.

The additional shoulders can be indexed with the $NaNbO_3$ unit cell (Figure 4.13b), e.g., ICCD, PDF: 01-077-0873. Once the presence of the $NaNbO_3$ perovskite is assumed in the stoichiometric mixture of $K_{0.5}Na_{0.5}NbO_3$, the presence of a phase rich in potassium becomes probable as well. The $KNbO_3$ peaks, e.g., ICDD, PDF: 01-071-0947, overlap with the KNN peaks. Finally, the XRD pattern of the calcined KNN-mono can be completely indexed with a range of perovskite solid solutions of $(K_xNa_{1-x})NbO_3$ with varying potassium and sodium ratios throughout the material (Figure 4.13b). The latter would result in the A-site inhomogeneities.

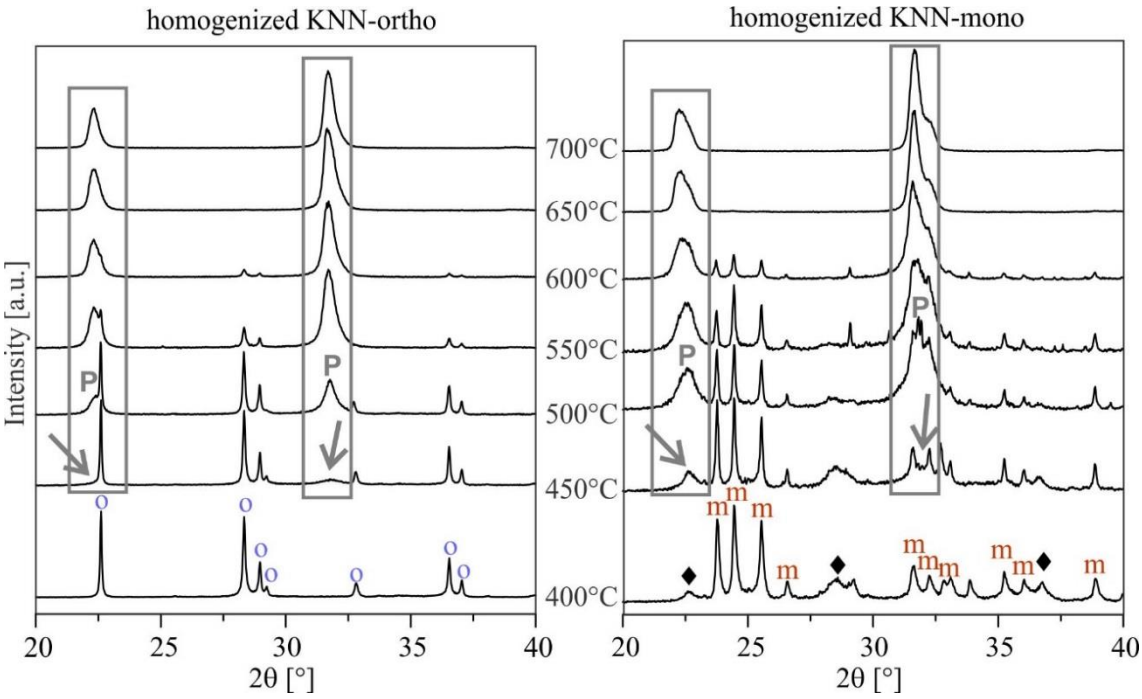


Figure 4.12: The XRD patterns of the homogenized KNN-ortho and -mono annealed to 400-700°C. **o** is the orthorhombic Nb_2O_5, **m** is the monoclinic Nb_2O_5, ♦ is the newly introduced Nb_2O_5 phase and P is the perovskite phase. The arrows mark the emerging perovskite phase peaks.

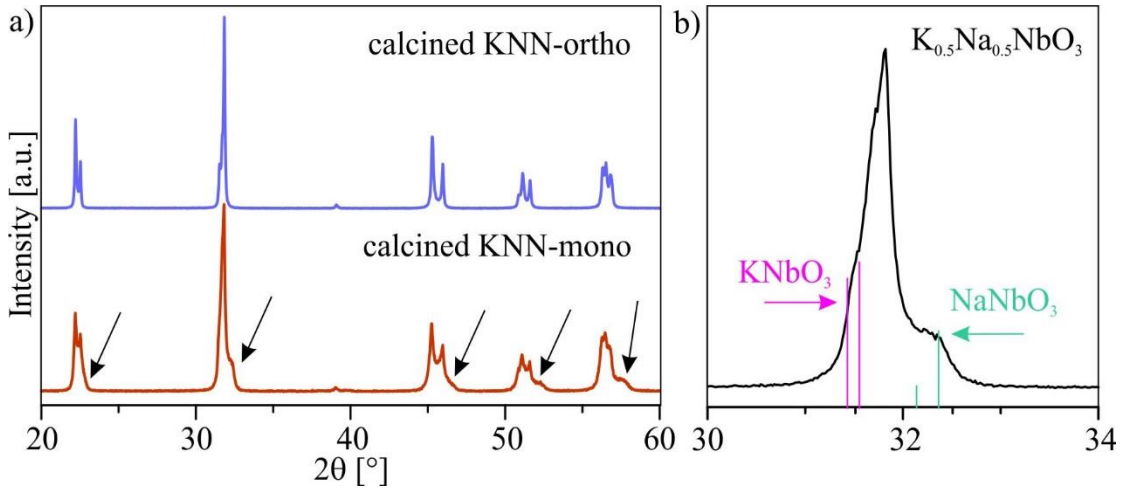


Figure 4.13: XRD patterns of the calcined KNN-ortho and –mono. a) XRD spectra of the calcined KNN-ortho and KNN-mono, arrows mark the shoulders in the XRD spectra of the calcined KNN-mono. b) enlarged view of the {110} peaks of the calcined KNN-mono with the marked XRD patterns of $KNbO_3$ (ICCD, PDF: 01-071-0947) and $NaNbO_3$ (ICCD, PDF: 01-077-0873).

Besides the typical solid-state synthesis of carbonates with niobium pentoxide, KNN can be prepared by the so-called perovskite route from an equimolar mixture of $KNbO_3$ and $NaNbO_3$ [32, 90]. The homogeneous KNN is formed only when annealed at temperatures as high as 950°C. The calcined KNN-mono was additionally annealed to 950°C for 4 h and milled in the planetary mill for 4 h. With this additional annealing step of the A-site inhomogeneous calcined KNN-mono (Figure 4.13, calcined KNN-mono), a homogeneous KNN was obtained. The XRD pattern of the calcined KNN-mono, annealed at 950°C, is consistent with the XRD pattern of the calcined KNN-ortho (Figure 4.12a: calcined KNN-ortho and Figure 4.14).

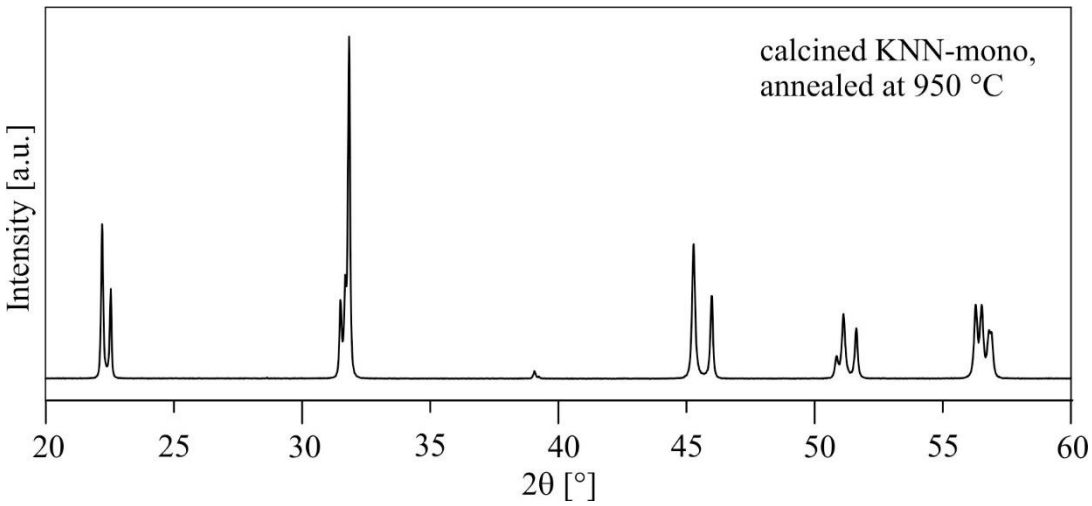


Figure 4.14: XRD spectra of the calcined KNN-mono annealed at 950°C, 4 h.

There are more ways to explain the differences in the course of the reaction of the homogenized KNN-ortho and mono. Besides the effect of the Nb_2O_5 particle size, also the effect of two different Nb_2O_5 polymorphs on the reaction rate, needs to be considered. Actually, once a phase transition occurs in one of the reactants or in the reaction product, the disorder during the phase transition permits the rapid diffusion of ions. The latter then lowers the temperature of the solid-state synthesis. This effect has been previously reported in different oxide systems and is referred to as the Hedvall effect [91-93].

Since the solid-state reaction seems to start at lower temperatures in the homogenized KNN-mono (refer to Figure 4.10 and Figure 4.11), the hypothesis of the Hedvall effect for the homogenized KNN-mono was verified. The milled Nb_2O_5-mono was investigated for possible phase transitions of the orthorhombic nanocrystals (refer to Figure 4.9). The milled Nb_2O_5-mono was annealed at different temperatures and the XRD patterns of the annealed powders were recorded. As is evident from Figure 4.15, no change occurs in the nanocrystalline orthorhombic phase until 700°C. At 750°C, the splitting of the broad peaks of the nanocrystalline Nb_2O_5 is visible, which is probably due to the crystal growth and/or structural ordering of the nanocrystalline Nb_2O_5 [86]. When heating up to 850°C, the orthorhombic peaks are not anymore detectable and the whole XRD pattern corresponds to the monoclinic Nb_2O_5 (JCPDS: 00-037-1468). This means, that the phase transition of the orthorhombic Nb_2O_5 to its monoclinic polymorph occurs between 800 and 850°C.

Based on the literature [91-93], the Hedvall effect requires that the temperature range at which the reaction happens matches with the temperature of the phase transition. Since the Nb_2O_5 phase transition from orthorhombic to monoclinic happens at 800 to 850°C (Figure 4.15) and since the reaction in the homogenized KNN-mono ends at 700°C (Figure 4.10 and Figure 4.11), the Hedvall effect does not apply here as an explanation for the different reactivity of the milled Nb_2O_5-mono with carbonates, when compared to the milled Nb_2O_5-ortho.

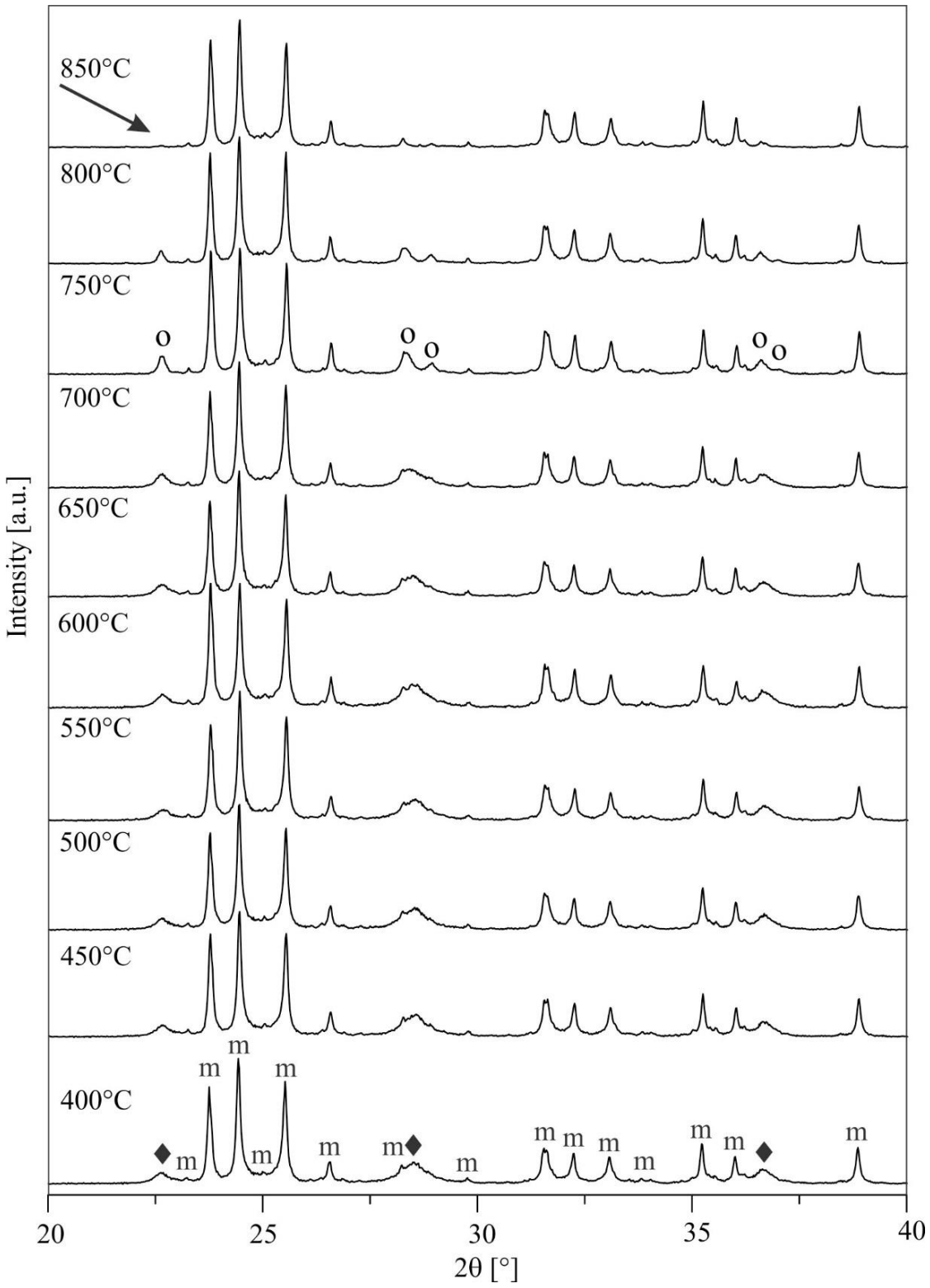


Figure 4.15: XRD spectra of the milled Nb_2O_5-mono, annealed at 400-850°C. ♦ is the nanocrystalline orthorhombic phase, **o** is the orthorhombic phase and **m** is the monoclinic phase.

The different reactivity of the KNN when using milled Nb_2O_5-ortho or -mono is more probably caused by the presence of the orthorhombic Nb_2O_5 nanocrystals in the milled Nb_2O_5-mono. In their diffusion-couples study of KNN reported by Malič et al. [19], the reaction in the

Na_2CO_3/Nb_2O_5 diffusion couple starts at 500°C, while in the K_2CO_3/Nb_2O_5 diffusion couple the reaction starts only at higher temperature, i.e., at 600°C. Also, the parabolic rate constant at 600°C for the Na_2CO_3/Nb_2O_5 diffusion couple happens to be ten times higher than to the K_2CO_3/Nb_2O_5 diffusion couple, i.e., $1x10^{-14}$ m^2/s and $3x10^{-15}$ m^2/s, respectively. Therefore, Na_2CO_3 starts reacting at a lower temperature, and at 600°C the Na^+ diffusion rate into the Nb_2O_5 is faster compared to the K^+.

Beside that, the Nb_2O_5 nanoparticles probably exhibit a higher reactivity, because of the high surface free energy and the high curvature of the crystals with size in the nanorange [94]. In addition, these nanocrystals are attached to the Nb_2O_5 particles' surface, as is visible in Figure 4.9, so they are the first in contact with the K_2CO_3 and Na_2CO_3. As discussed above, the Na_2CO_3 starts reacting with the Nb_2O_5 nanocrystals at lower temperatures and since the diffusion paths in the nanocrystalline Nb_2O_5 are only of the order of tens of nm, i.e., relatively short, the Nb_2O_5 nanocrystals are likely to predominantly react with the Na_2CO_3 to form the $NaNbO_3$. The K_2CO_3 together with the remaining, yet unreacted, part of Na_2CO_3 would then react later, at higher temperatures during heating with the submicron-sized monoclinic Nb_2O_5 crystals (see Figure 4.9). Since the diffusion paths through the relatively large submicron Nb_2O_5 particles are longer than in the Nb_2O_5 nanocrystals, the diffusion-controlled reaction is expected to be slower, and because of the K_2CO_3 reacting in the majority, it would also take place only at higher temperatures (Figure 4.11). The consequence of such a course of the reaction is likely to be the coexistence of $NaNbO_3$ and $KNbO_3$ phases and/or inhomogeneous $(K_xNa_{1-x})NbO_3$ solid solutions, at the end of the solid-state synthesis. This is in agreement with the XRD pattern of the calcined KNN-mono in Figure 4.13. The inter-diffusion of Na and K ions, which is necessary to obtain a homogeneous KNN, is possible only at temperatures as high as 950°C [90], as shown in Figure 4.14, in the XRD spectra of the calcined KNN-mono additionally annealed at 950°C for 4 h.

4.1.3 Sintering of KNN

In the following section, the calcined powders from the previous study of the solid-state synthesis are investigated for densification behaviour and the properties of the sintered ceramic pellets are studied. In the study of the densification process, the samples are denoted as: calcined KNN-ortho pellet, calcined KNN-mono pellet and calcined KNN-mono-950 pellet. After sintering the samples are denoted as sintered KNN-ortho, sintered KNN-mono and sintered KNN-mono-950.

The sintering curves of the three calcined powders, which were pressed into pellets with comparable green densities, i.e., 2.8 g/cm^3, are presented in Figure 4.16.

The shrinkage for the calcined KNN-ortho starts slowly at 1000°C, with the rapid shrinkage rate occurring between 1100 and 1140°C. As discussed in the results from the reaction curves in Figure 4.10, 1140°C is the KNN melting point [7, 12]. The densification behaviour with the narrow densification interval observed for the calcined KNN-ortho is in agreement with the results reported by Kosec and Kolar [12].

On the other hand, the calcined KNN-mono starts shrinking already at 900°C, with a rapid shrinkage rate until 1000°C, after which a plateau in dimensional changes occurs. Although it is not visible on the curve, the deformation of the pellet, which is attributed to the melting, can be observed with an optical dilatometer at 1160°C as a spilling bottom of the pellet (Figure 4.16b).

The sintering curve of the calcined KNN-mono-950 (Figure 4.16a) shrinks with a relatively less steep shrinkage rate between 950 and 1150°C. The dilatation of the pellet attributed to the melting is seen on the curve at 1160°C.

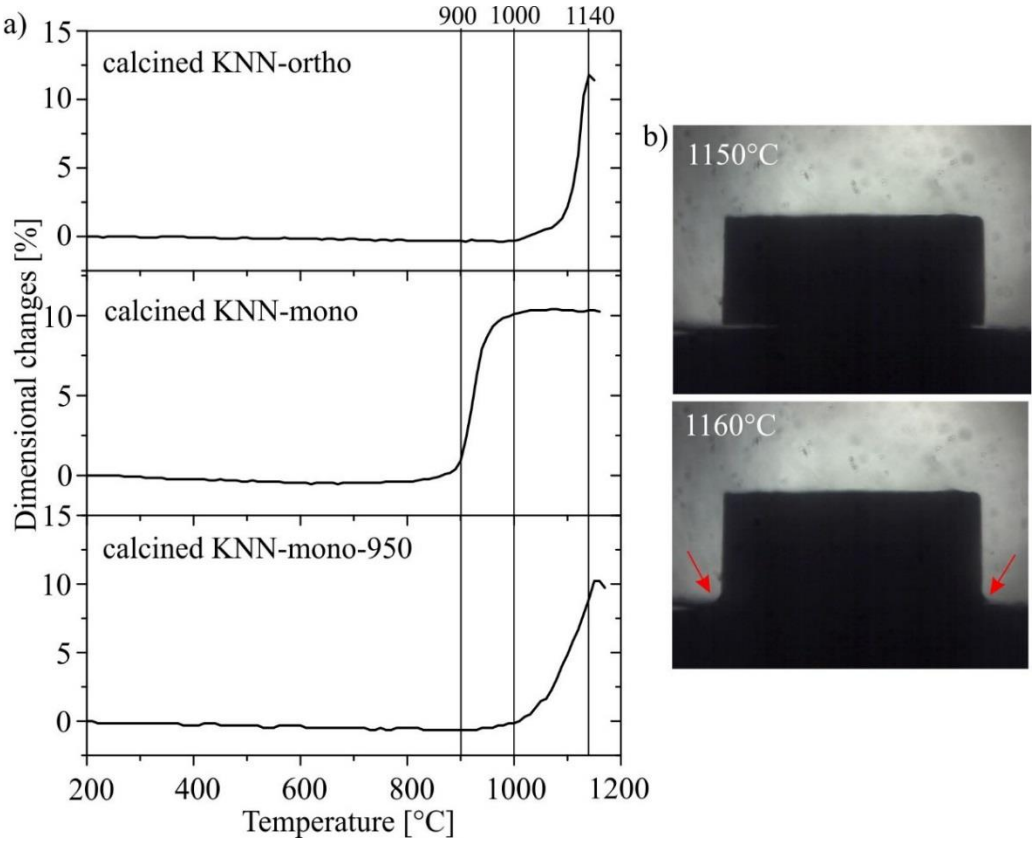


Figure 4.16: Sintering curves. a) dimensional changes with the increasing temperature of the calcined KNN-ortho, calcined KNN-mono and calcined KNN-mono additionally annealed at 950°C, 4 h powder compacts b) images of the homogenized KNN-mono powder compact near the melting point, arrows mark the shape deformations due to melting.

Therefore, each of the powders has a different densification behaviour. The calcined KNN-mono starts shrinking at a 200°C lower temperature than the calcined KNN-ortho, as was already observed in Figure 4.10.

The calcined KNN-mono-950 exhibits a shrinkage that is not as steep as usually reported for KNN [12] and as was observed for the calcined KNN-ortho, and yet, the shrinkage observed in Figure 4.16a, calcined KNN-mono-950 is different from the curve observed for the calcined KNN-mono without the annealing step. The results in Figure 4.16 suggest, that although the calcined KNN-mono powder is additionally annealed to become A-site homogeneous, the effect of the Nb_2O_5-mono reagent is not completely removed and still influences the densification behaviour.

Table 4.2: Densities of the sintered ceramics.

Powder	Sintering temperature [°C]	Density [g/cm^3]	Relative density [%]
KNN-ortho	1120	4.17(2)	92.4(4)
KNN-mono	1120	4.21(3)	93.4(7)
KNN-mono-950	1120	3.91(1)†	86.6(1)†

† measured as geometric density

The different densification behaviour resulted in different densities after sintering under identical conditions (see Table 4.2), i.e., 1120°C, 2 h. The highest density, i.e., 93.4 %TD, was for the sintered KNN-mono, however, the ceramic became mechanically unstable once it was taken out from the distilled water after the Archimedes density measurement and dried at 200°C. On the other hand, the sintered KNN-ortho had a density of 92.4 % TD and remained mechanically

stable. The sintered KNN-mono-950 was mechanically stable as well, but had a very low density, i.e., 86.6 % TD.

Figure 4.17 presents the SEM micrographs of the sintered ceramics. Polishing and etching of the sintered KNN-ortho reveals angular grains, ranging mostly from 3 µm to 10 µm. Round pores of 1 to 2 µm in size can be seen trapped in the larger grains. The visible pull-outs and lines are due to the sample preparation.

The sintered KNN-mono has significantly larger grains compared to the sintered KNN-ortho, i.e., of the order of several tens of µm. The large grains are divided by cracks, which is probably the reason for the mechanical instability of the sintered KNN-mono ceramics.

On the other hand, the microstructure of the sintered KNN-mono-950 shows grains similar in size and shape to the ones of the sintered KNN-ortho, with no cracks. Anyway, in addition to the intragranular pores, also large, 5- µm sized intergranular pores are visible, which is in agreement with the low density of the sintered KNN-mono-950 ceramics (see Table 4.2, KNN-mono-950).

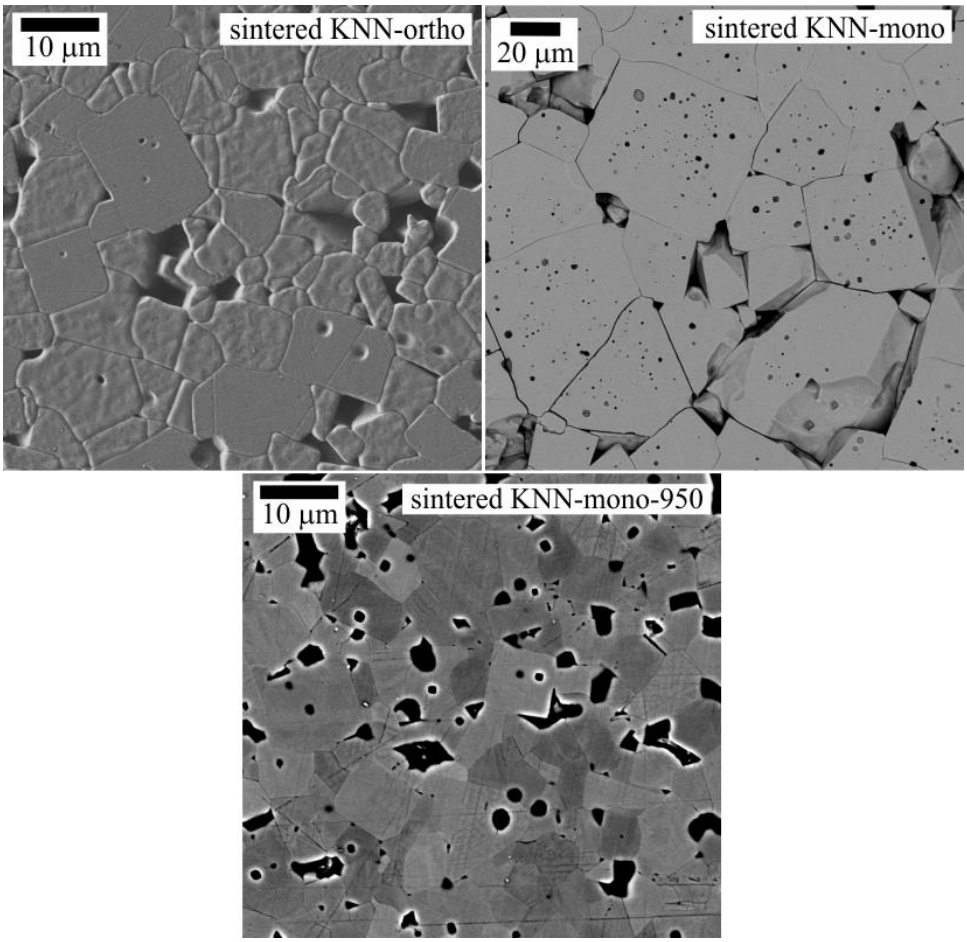


Figure 4.17: SEM micrographs of the sintered samples. Sintered KNN-ortho (polished and thermally etched, SEI mode), sintered KNN-mono (polished, BSE mode) and sintered KNN-mono-950 (polished and thermally etched, BSE mode).

The starting A-site inhomogeneity of the calcined KNN-mono appears to be the reason for the difference between the densification behaviour (Figure 4.16) and the microstructure (Figure 4.17) of the KNN-ortho and –mono. It is likely that the grain growth and densification of the $(K_xNa_{1-x})NbO_3$ solid solution, which is rich in potassium, occurs at different rates and lower temperatures than if the solid solution is rich in sodium, since the melting point of $KNbO_3$ is 1040°C and for $NaNbO_3$ it is 1420°C [95]. As a result, certain grains of the calcined KNN-mono then exhibit abnormal grain growth. That is why the abnormal grain growth is not present in the KNN-mono-950 that was homogenized with an additional annealing step. However, sintering of

the calcined KNN-mono-950 results in a much lower density compared to the sintered KNN-ortho (Figure 4.17 and Table 4.2, KNN-mono-950).

Figure 4.18 presents the particle size distribution and SEM micrographs of the calcined KNN-ortho in comparison with the calcined KNN-mono-950. As is clear from Figure 4.18a, a significant portion of the particles of the calcined KNN-mono-950 powder are of a size over 1 µm, while the calcined KNN-ortho contains finer particles, mostly under 1 µm. The morphologies of the two powders are different as well (see Figure 4.18b). The particles of the calcined KNN-ortho possess an irregular surface, while the calcined KNN-mono-950 powder not only contains a large portion of the particles above 1 µm, but also the particles appear to have relatively flat surfaces and are cracked (Figure 4.18b, red arrow).

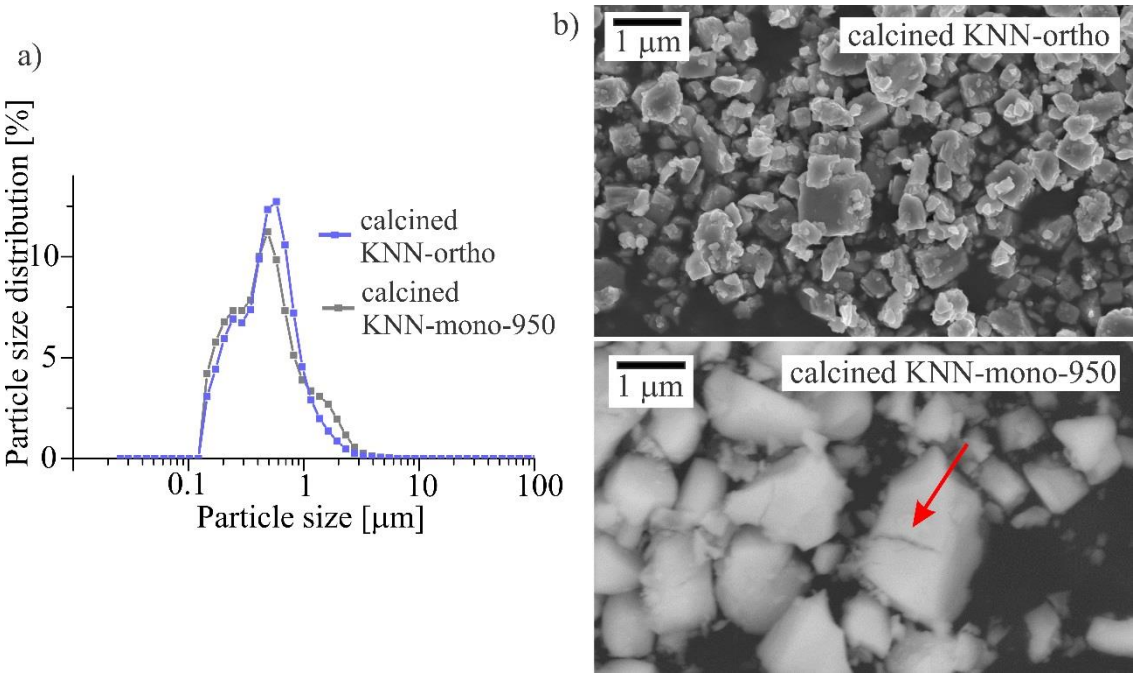


Figure 4.18: Calcined KNN-ortho and calcined KNN-mono-950 powders. a) particle size distribution of the calcined KNN-ortho and calcined KNN-mono-950 b) SEM micrographs of the calcined KNN-ortho (SEI mode) and calcined KNN-mono-950 (BSE mode), red arrow marking a crack.

The poor densification of the calcined KNN-mono-950 is therefore most probably related to the particle coarsening due to the high temperature of the annealing, i.e., 950°C. In spite of the subsequent planetary-milling step, it was not possible to obtain powder as fine as the calcined KNN-ortho (Figure 4.18).

4.2 Study of the Solid-State Synthesis of KNN Doped with Strontium

Based on the results in Section 4.1, the Nb_2O_5-ortho was used as a reagent in the solid-state synthesis of the samples in the subsequent sections.

To investigate the influence of the Sr-doping on the KNN reaction mechanism, the KNN samples doped with Sr were studied by thermal analysis and *in-situ* high-temperature X-ray diffraction and the reaction of the KNN-ortho studied in the previous section was used as a reference. The samples were in the form of homogenized mixtures of the milled potassium, sodium and strontium (in the case of the Sr-doped samples) carbonates with milled niobium pentoxide, which was prepared based on the formula determined in the Materials and Methods section. In the following section, the studied homogenized mixtures are further denoted as: KNN-ortho, KNN-1% Sr, KNN-2% Sr and KNN-6% Sr. Additionally, KNN was once more prepared from the orthorhombic Nb_2O_5, which was not milled before the homogenization. This sample is used for a comparison and is denoted as KNN-nm.

4.2.1 Study of the reaction by thermal analysis

Figure 4.19 presents the TG and DTG curves for KNN-ortho, KNN-1% Sr, KNN-2% Sr, KNN-6% Sr and KNN-nm in the temperature interval between 200 and 750°C. Similar to the KNN-ortho (see Figure 4.11), the mass loss happens in two steps, which is visible as the typical two DTG peaks between 400°C and 540°C and between 540°C and the end of the reaction (further denoted as T_{FIN}). The reaction is finished at T_{FIN} = 630, 660, 630, 660 and 675°C for KNN-ortho, KNN-1% Sr, KNN-2% Sr, KNN-6% Sr and KNN-nm, respectively (see Figure 4.19, red dotted lines).

The theoretical mass losses were calculated according to Equations (4.3), (4.4) and (4.5).

$$0.49K_2CO_3 + 0.49Na_2CO_3 + 0.02SrCO_3 + Nb_2O_5 \rightarrow 2K_{0.49}Na_{0.49}Sr_{0.01}NbO_3 + CO_2 \quad (4.3)$$

$$0.48K_2CO_3 + 0.48Na_2CO_3 + 0.04SrCO_3 + Nb_2O_5 \rightarrow 2K_{0.48}Na_{0.48}Sr_{0.02}NbO_3 + CO_2 \quad (4.4)$$

$$0.44K_2CO_3 + 0.44Na_2CO_3 + 0.12SrCO_3 + Nb_2O_5 \rightarrow 2K_{0.44}Na_{0.44}Sr_{0.06}NbO_3 + CO_2 \quad (4.5)$$

Table 4.3 gives a comparison of the theoretical mass losses and the mass losses measured experimentally for all the discussed samples, between 200 and 750°C. The experimentally determined mass losses in this interval are lower than they should be theoretically. On the other hand, the total mass losses measured between room temperature and 750°C, are systematically higher than the theoretical values.

In order to explain this discrepancy, Figure 4.20 presents the TG, DTG, DTA and EGA of a KNN-1% Sr that were recorded between room temperature and 750°C. Below 200°C, the H_2O and CO_2 (Figure 4.20, EGA) are being simultaneously released from the system and are obviously accompanied by a certain mass loss, as seen from the TG/DTG curves. According to the DTA curve, this process is endothermic, with peaks at 121°C and 194°C.

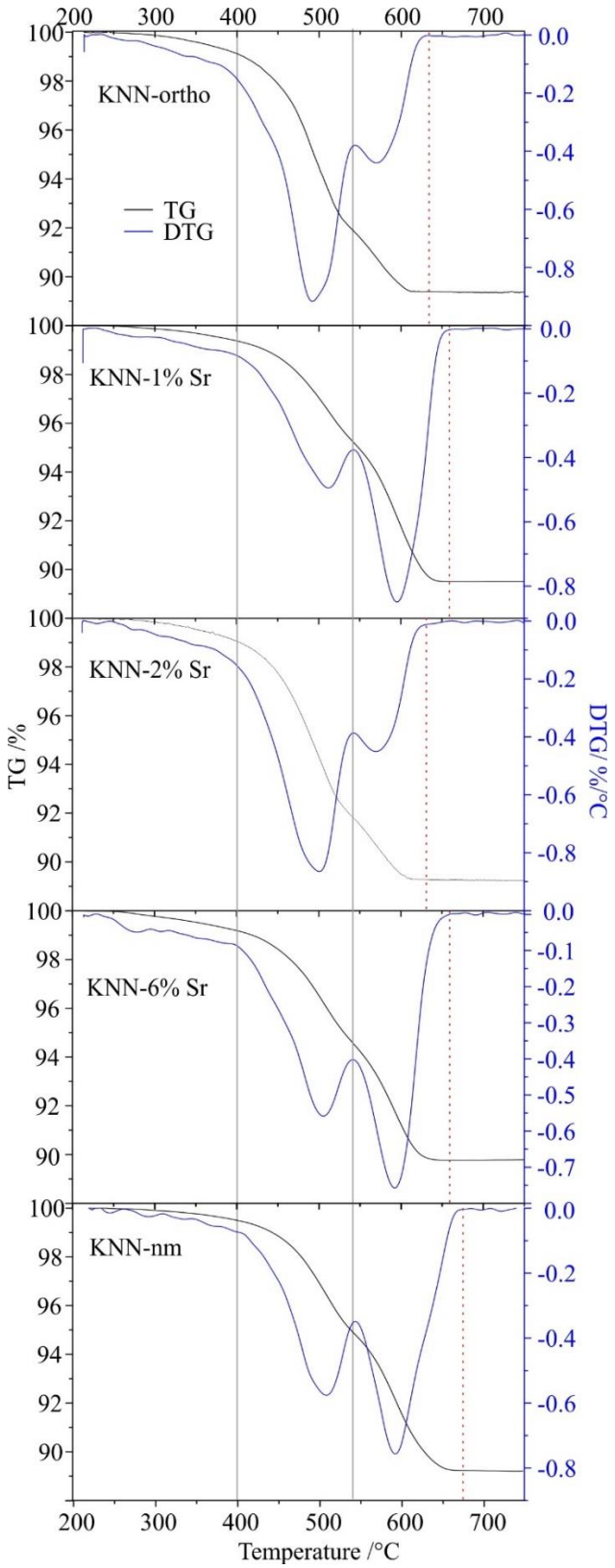


Figure 4.19: TG and DTG of KNN-ortho, KNN-1% Sr, KNN-2% Sr, KNN-6% Sr and KNN-nm in the temperature interval 200–750°C. The full grey lines mark the peaks onset, the dotted red lines mark the end of the reaction.

Table 4.3: Theoretical and actual mass losses of KNN-ortho, KNN-1% Sr, KNN-2% Sr, KNN-6% Sr and KNN-nm.

	Theoretical mass loss [%]	Mass loss 25–750°C [%]	Mass loss 200–750°C [%]
KNN-ortho	11.34	11.48	10.83
KNN-1% Sr	11.33	13.66	10.49
KNN-2% Sr	11.32	11.77	10.75
KNN-6% Sr	11.26	14.40	10.22
KNN-nm	11.35	12.53	10.83

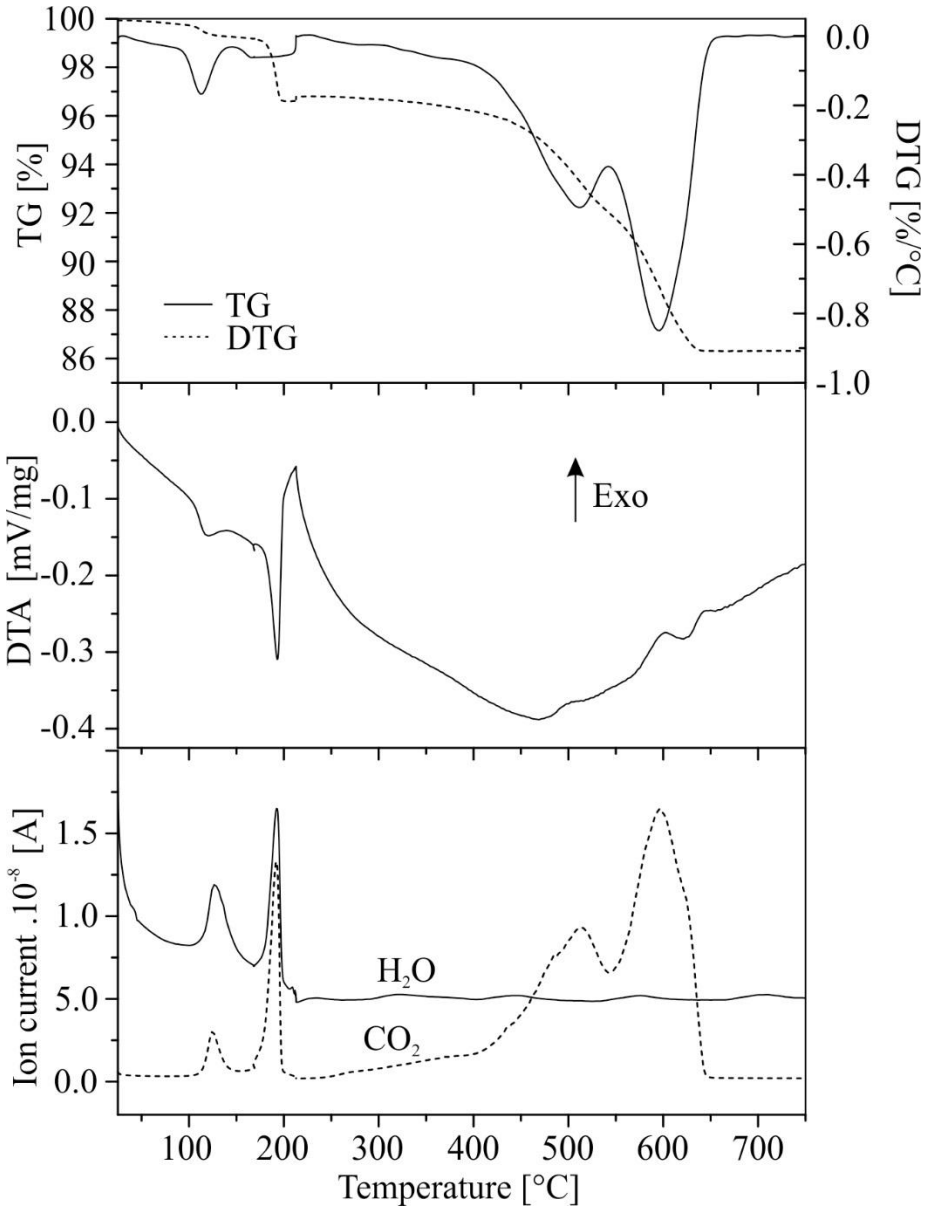


Figure 4.20: TG, DTG, DTA and EGA of the KNN-1% Sr in the temperature interval from RT to 750°C.

As was already introduced in the Section 4.1.2.2, the KNN solid-state synthesis is usually observed between 200 and 750 °C, where the CO_2 is released in two steps as a result of the

carbonates decomposition [20]. Based on the Atlas of thermoanalytical curves [96], the endothermic process happening before the solid-state synthesis takes place, can be attributed to the $NaHCO_3$ and $KHCO_3$ decompositions, which happen below 200 °C according to Equation (4.6) and (4.7).

$$2\ \mathrm{NaHCO_3} \rightarrow \mathrm{Na_2CO_3} + \mathrm{H_2O} + \mathrm{CO_2} \tag{4.6}$$

$$2\ \mathrm{KHCO_3} \rightarrow \mathrm{K_2CO_3} + \mathrm{H_2O} + \mathrm{CO_2} \tag{4.7}$$

The smaller peak on the EGA curves at ~120°C can be attributed to the $NaHCO_3$ decomposition, since according to the literature [96], $NaHCO_3$ decomposes at 130°C, while the peak at ~195°C would then signify the $KHCO_3$ decomposition, which was reported to have its maximum at 160°C [96].

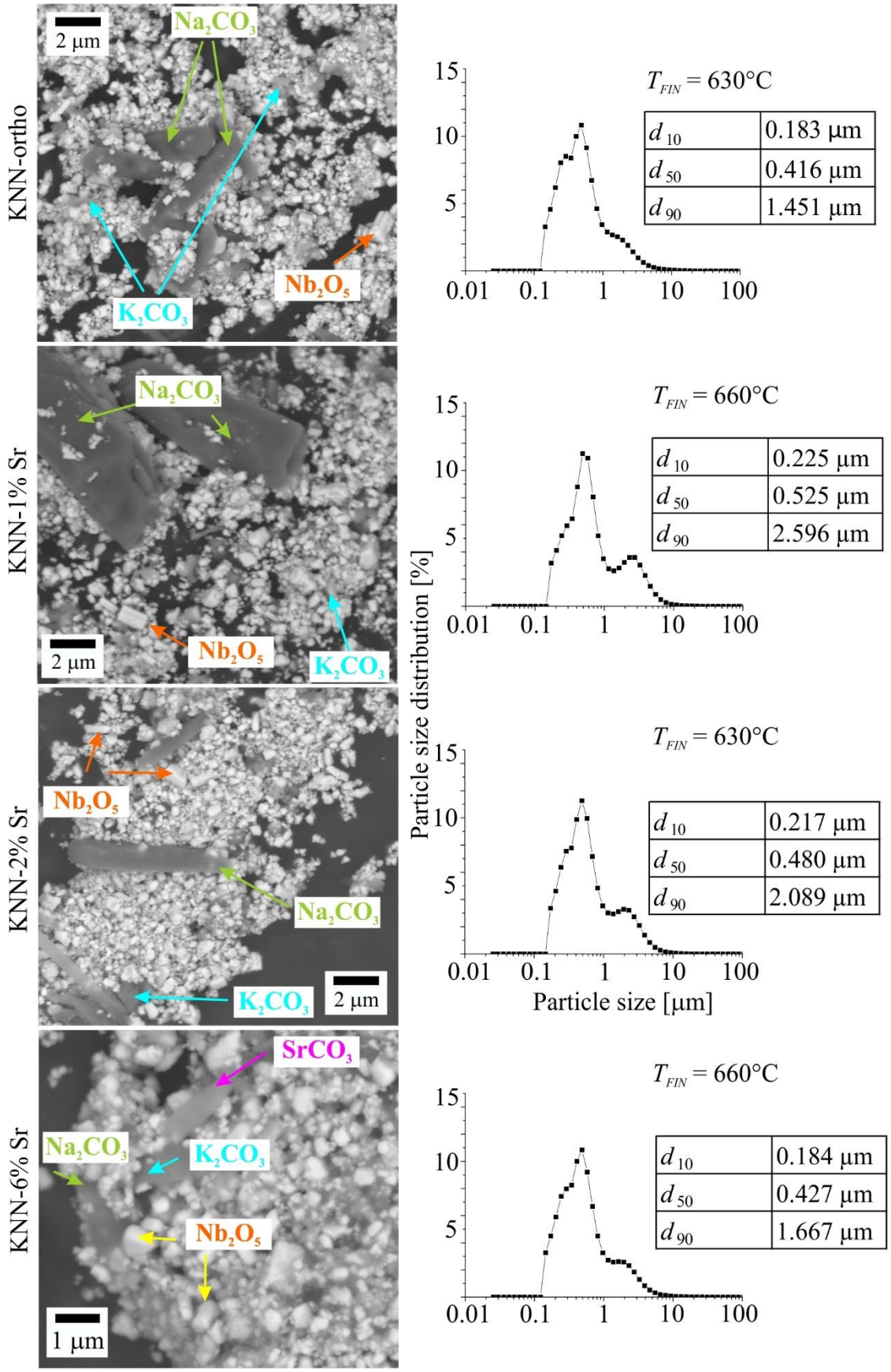
As is written in Section 3.1, the alkali carbonates in the anhydrous form were used for the solid-state synthesis of the prepared samples. After drying, the carbonates were weighed in a drybox, since otherwise, they quickly adsorb the atmospheric humidity. K_2CO_3 is more humidity-sensitive than Na_2CO_3, which is also demonstrated by the XRD patterns of the potassium and sodium carbonates which were measured in ambient air in Figure 4.1 and Figure 4.2; therefore, the K_2CO_3 is expected to contain more hydrogen carbonate compared to the Na_2CO_3. This corresponds well with the EGA peaks' intensities and supports the attribution of the peak at ~120°C, as the decomposition of $NaHCO_3$ and the one at ~195°C as $KHCO_3$.

The higher value of the total mass losses between room temperature and 750 °C can therefore be explained by the fact that the mass loss also accounts for the loss of H_2O adsorbed from the ambient air. The lower value of the mass loss between 200 and 750 °C then suggests that the CO_2 necessary for the formation of hydrogen carbonates actually originates from the reagents and is then lost below 200°C upon the decomposition of the hydrogen carbonates.

Figure 4.19 also shows a varying T_{FIN} for the different samples. In order to clarify the reason for the T_{FIN} shifts, the SEM-EDXS study of the particles' morphology, together with the granulometric analysis of the homogenized mixtures is presented in Figure 4.21.

In Figure 4.21, the SEM micrographs are in the left-hand column. The largest, grey particles are the carbonates with a particle size of 5–10 µm as seen on the granulometric analyses in Figure 4.21, the middle column. Also, the carbonate particles of the 1–5 µm size are seen on the images. The dark-grey particles are the Na_2CO_3, while the light-grey particles are the K_2CO_3. The fine white particles belong to the Nb_2O_5. $SrCO_3$ particles could be identified in KNN-6% Sr as marked in the Figure 4.21, KNN-6% Sr. Overall, the particle morphologies of all the investigated powders were found to be comparable.

Some differences in the particle size distribution of the homogenized mixtures can be addressed. For example, the KNN-ortho has larger d_{10}, d_{50} and d_{90} (see Figure 4.21, tables in the right-hand column) compared to KNN-1% Sr, which has a significantly higher portion of the particles over 1 µm, and as expected, the larger particle size would result in the T_{FIN} shift to higher temperatures, i.e., 630 and 660°C for KNN-ortho and KNN-1% Sr, respectively. However, this trend is not confirmed for the other samples, i.e., based on the particle size distributions, the KNN-2% Sr would be expected to have a higher T_{FIN} compared to the KNN-6% Sr, and it does not. Finally, neither in the undoped KNN samples, i.e., KNN-ortho and KNN-nm, the particle size distribution cannot be correlated to the changes in T_{FIN}.



The figure continues on the next page

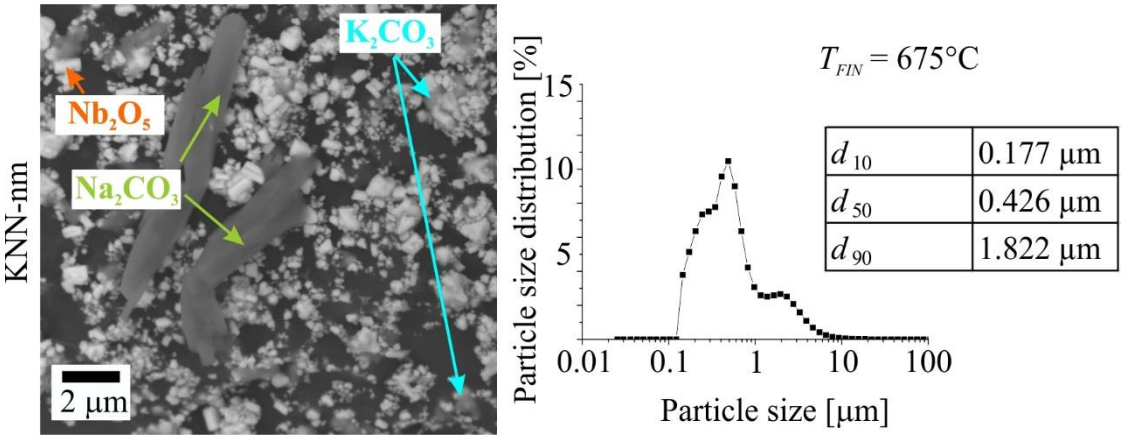


Figure 4.21: Particles morphology and particle size distribution of the homogenized mixtures. From top to bottom: KNN-ortho, KNN-1, 2 and 6% Sr and KNN-nm. The left column: BSE SEM micrographs of the homogenized mixtures. The dark and light grey particles are Na_2CO_3 and K_2CO_3, respectively, the white particles are Nb_2O_5. $SrCO_3$ have the lightest grey contrast and could be detected only for KNN-6% Sr. Middle column: particle size distribution of the homogenized mixtures of the reagents. Right column: d_{10}, d_{50} and d_{90} of the powders. T_{FIN} is marked for each sample.

Based on the literature [19, 20], it is known that the time for completion of the diffusion-controlled reaction between the alkali reagents and niobium pentoxide increases with the increasing particle size of the Nb_2O_5 reagent. Since the five studied samples were prepared within different batches and because the Nb_2O_5 was milled for each batch separately, there are possible differences between the particle-size distributions of the used Nb_2O_5 reagents.

Figure 4.22 presents the granulometric analyses results of the Nb_2O_5 used for the synthesis of KNN-ortho, KNN-1% Sr, KNN-2% Sr, KNN-6% Sr and KNN-nm. The T_{FIN} from Figure 4.19 is marked as well. As expected based on the literature, the highest T_{FIN}, i.e., 675°C, was measured for the KNN-nm, which was prepared from the Nb_2O_5 with by far the largest d_{10}, d_{50} and d_{90}, and a significantly larger portion of the particles above 1 µm compared to the rest of the samples. KNN-1% Sr and KNN-6% Sr had the same T_{FIN}, i.e., 660°C, and they were prepared using the same batch of Nb_2O_5. KNN-ortho as well as KNN-2% Sr were also prepared within the same batch and the same Nb_2O_5 was used for their synthesis, the two samples had the same T_{FIN}, i.e., 630°C. The Nb_2O_5 used for the preparation of the KNN-ortho, KNN-1% Sr, KNN-2% Sr and KNN-6% Sr are more or less comparable.

The other mass loss parameters that vary among the studied samples are the intensity and position of the two main DTG peaks (see Figure 4.19, DTG curves). The KNN-ortho and KNN-2% Sr have basically the same DTG curves. So do the KNN-1% Sr and KNN-6% Sr. The profile of KNN-nm is different to all the other samples.

The differences between the particle size distributions of Nb_2O_5 could also be the reason for the changing intensity of the two main DTG peaks, since the peaks intensity profile is strongly related to the particular batch, just as in the case of the shifting T_{FIN} (see Figure 4.19, intensity profile of the DTG peaks for KNN-1% Sr and KNN-6% Sr, and KNN-ortho with KNN-2% Sr, prepared from the same batch of Nb_2O_5).

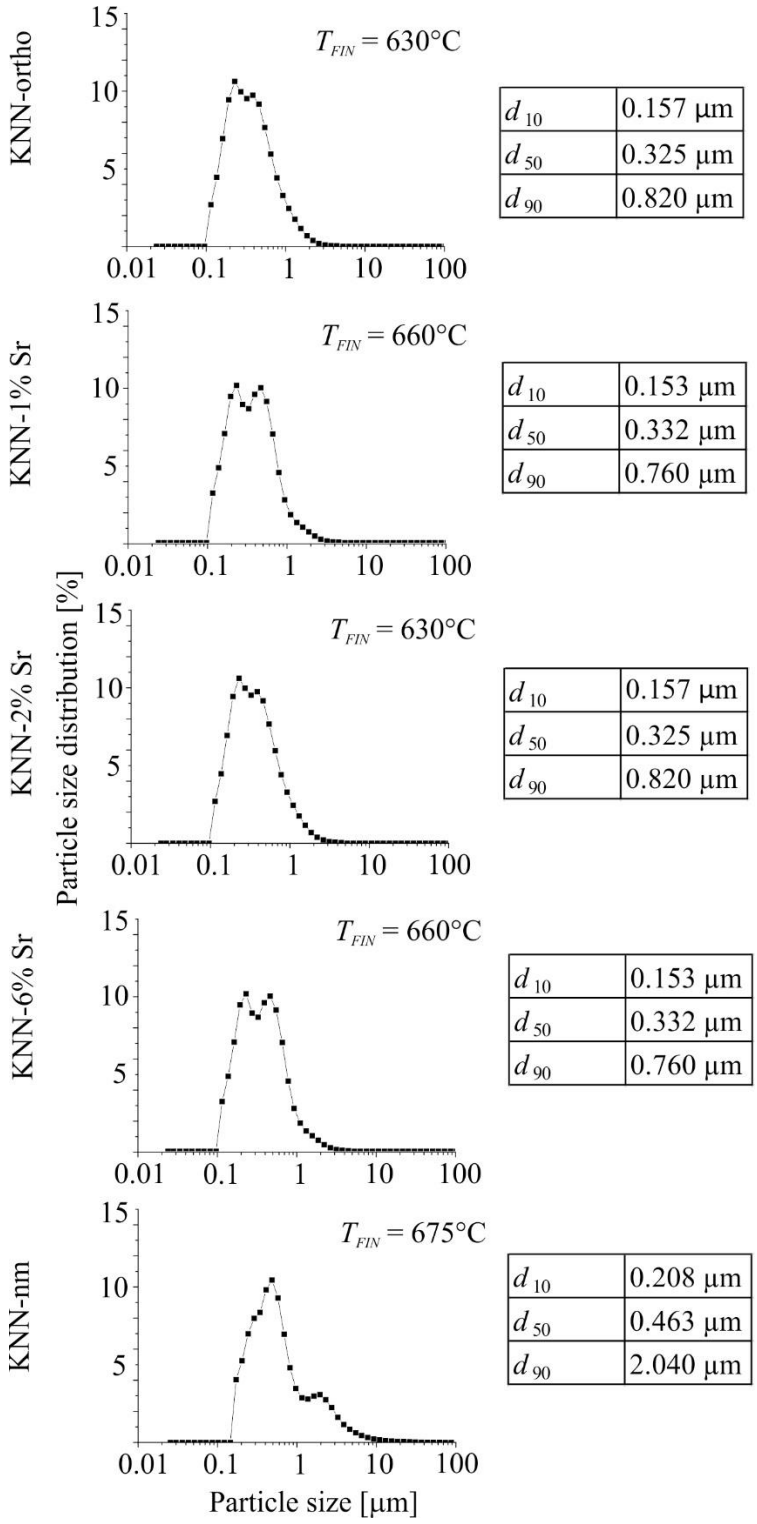


Figure 4.22: Particle size distribution of the Nb_2O_5 used for synthesis in the particular sample. From top to bottom: KNN-ortho, KNN-1% Sr, KNN-2% Sr, KNN-6% Sr and KNN-nm. The left column: particle size distribution of the Nb_2O_5 used for the preparation of the sample. Right column: d_{10}, d_{50} and d_{90} of the Nb_2O_5. The T_{FIN} is marked for each sample.

Figure 4.23 presents the DTA curves of KNN-ortho, KNN-1% Sr, KNN-2% Sr, KNN-6% Sr and KNN-nm. One DTA exothermic peak occurs in the temperature interval between 400 and 540°C, and two DTA exothermic peaks occur in the temperature interval between 540 and the T_{FIN}.

The temperature intervals of the first and the last two exothermic peaks correspond to the temperature intervals of the first and second DTG peaks, respectively (see Figure 4.19). The intensity of the corresponding exothermic peaks on the DTA curves varies in correlation with the varying intensity of the 1st and 2nd DTG peaks. The 1st and 2nd exothermic peaks appear at the approximately same temperatures, i.e., at ~500 °C and ~600 °C, respectively, for KNN-ortho, KNN-1% Sr and KNN-2% Sr and KNN-nm. For the KNN-6% Sr, the 1st peak shifts to as low as 455°C. The 3rd exothermic peak is determined by the T_{FIN} for all the samples.

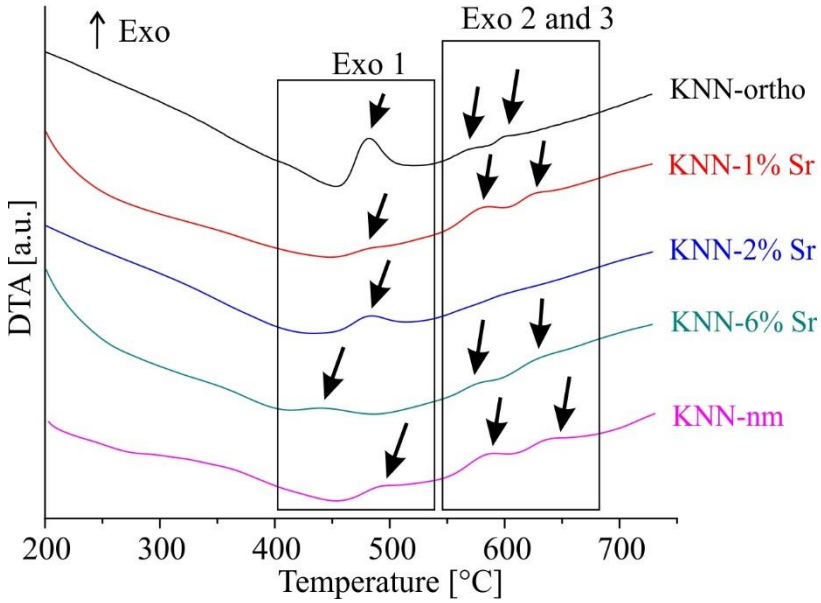


Figure 4.23: DTA of the KNN-ortho, KNN-1% Sr, KNN-2% Sr, KNN-6% Sr, KNN-nm. Arrows mark the positions of the exothermic peaks.

4.2.2 Study of the reaction by *in-situ* high-temperature X-ray diffraction

In order to relate the thermally induced processes that were determined by the thermal analysis with the phase-composition changes of the samples, the *in-situ* high-temperature X-ray diffraction (HT-XRD) of the investigated samples was recorded.

Figure 4.24 presents the HT-XRD spectra of KNN-nm, KNN-1% Sr, KNN-2% Sr and KNN-6% Sr between room temperature and 700°C. At room temperature, the visible peaks of the unreacted powders can be indexed with the orthorhombic Nb_2O_5 (ICDD, PDF: 01-071-0336), except the KNN-6% Sr, where, besides the Nb_2O_5, also the two most intense $SrCO_3$ (ICDD, PDF: 01-084-1778) peaks are seen (refer to Figure 4.24, KNN-6% Sr, marked **s**). Above 400°C, the intensity of the Nb_2O_5 peaks starts decreasing and at 450°C, the {100} and {110} perovskite peak families can be recognized (see Figure 4.24, marked **P**). The phase compositional changes for the samples up to 2% Sr are comparable to the results of the annealing experiment of KNN-ortho (see Figure 4.12, KNN-ortho). The formation of the perovskite phase starts at the same temperature for all the samples, regardless of the Sr content. The perovskite peaks grow with the increasing temperature and the decreasing Nb_2O_5-peaks. Besides the perovskite, a secondary phase can also be detected in KNN-6% Sr (see Figure 4.24, KNN-6% Sr, RT, marked with arrows).

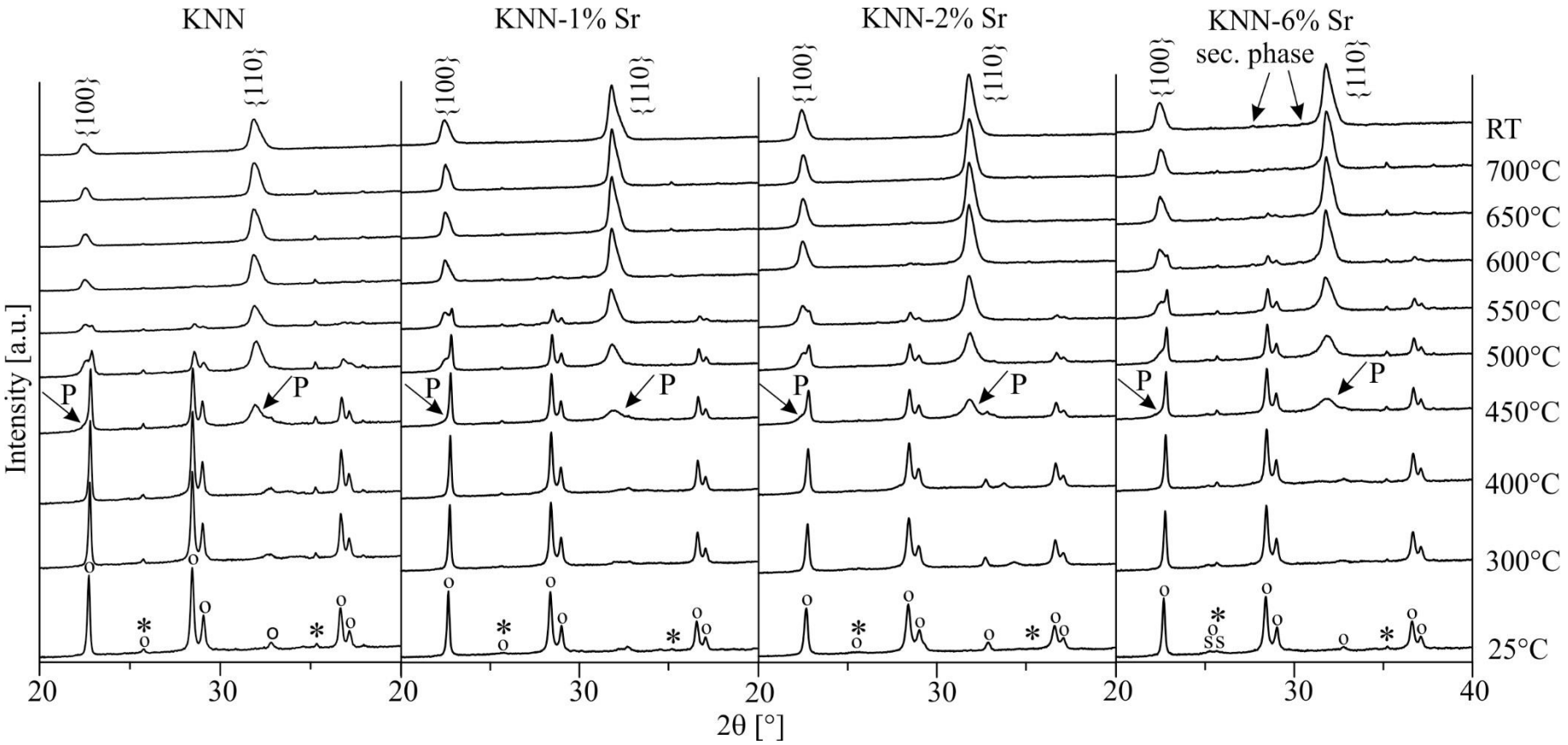


Figure 4.24: In-situ HT-XRD spectra of the KNN-nm, KNN-1% Sr, KNN-2% Sr and KNN-6% Sr. Peak families are indexed with the KNN monoclinic unit cell according to Tellier [32]. Arrows mark the appearance of the perovskite phase **P** and the secondary phase peaks. Nb_2O_5 peaks are marked with **o** and $SrCO_3$ peaks are marked with **s**. The peaks marked with a * denote the Al_2O_3 sample holder.

Figure 4.25 presents the enlarged HT-XRD spectra of the KNN-6% Sr for better visibility of the peaks belonging to the secondary phase. The secondary-phase peaks could be indexed with the tetragonal tungsten bronze polyniobate phase, e.g., $K_6Nb_{10.88}O_{30}$ (ICDD, PDF: 01-087-1856). The peaks are detectable at 600°C, but due to the low resolution of the HT-XRD spectra, it cannot be excluded that the secondary phase appears at even lower temperatures.

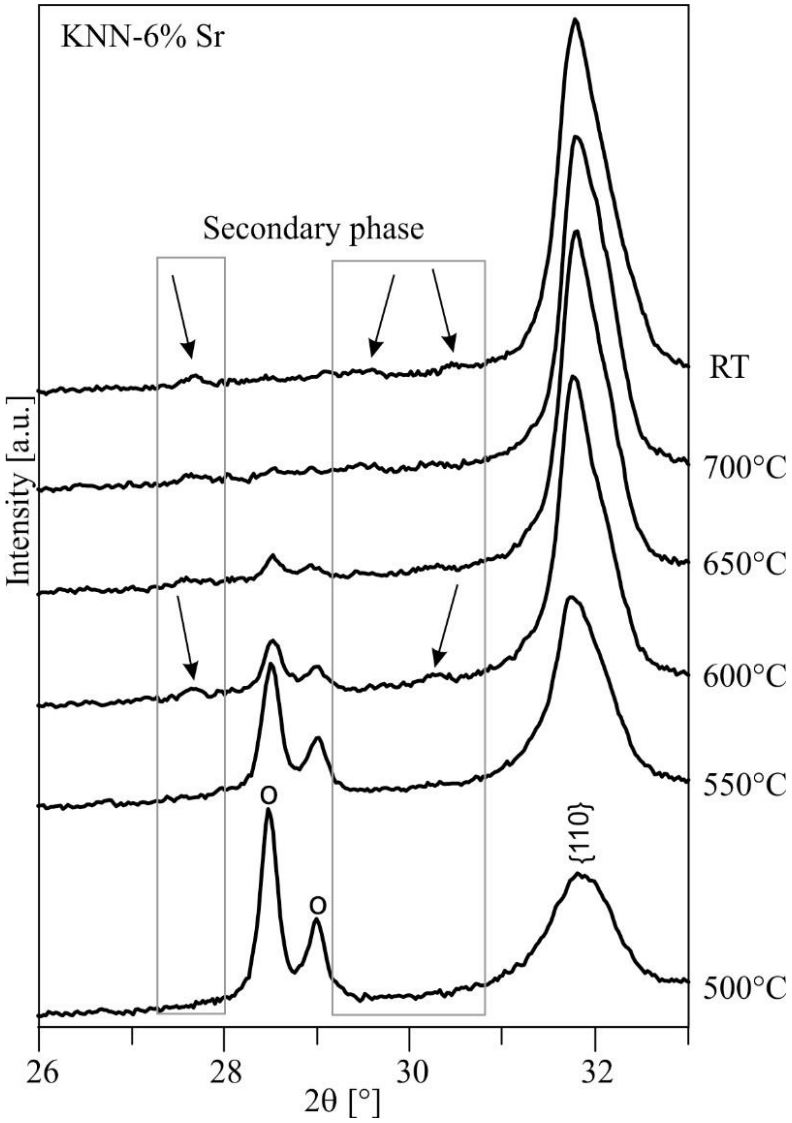


Figure 4.25: Enlarged in-situ HT-XRD spectra of the KNN-6% Sr sample. The tungsten bronze polyniobate secondary phase peaks are marked with arrows. Nb_2O_5 peaks are marked with **o.** Perovskite peak families are indexed with the KNN monoclinic unit cell according to Tellier [32].

A tetragonal tungsten bronze polyniobate secondary phase in KNN was reported to be formed after annealing for 10 h at 1145°C, as a consequence of the alkalines evaporation [55]. However, in the studied Sr-doped KNN samples, the secondary phase was already formed after the first calcination at 800°C (see Figure 4.26) and only for the samples with more than 2% Sr.

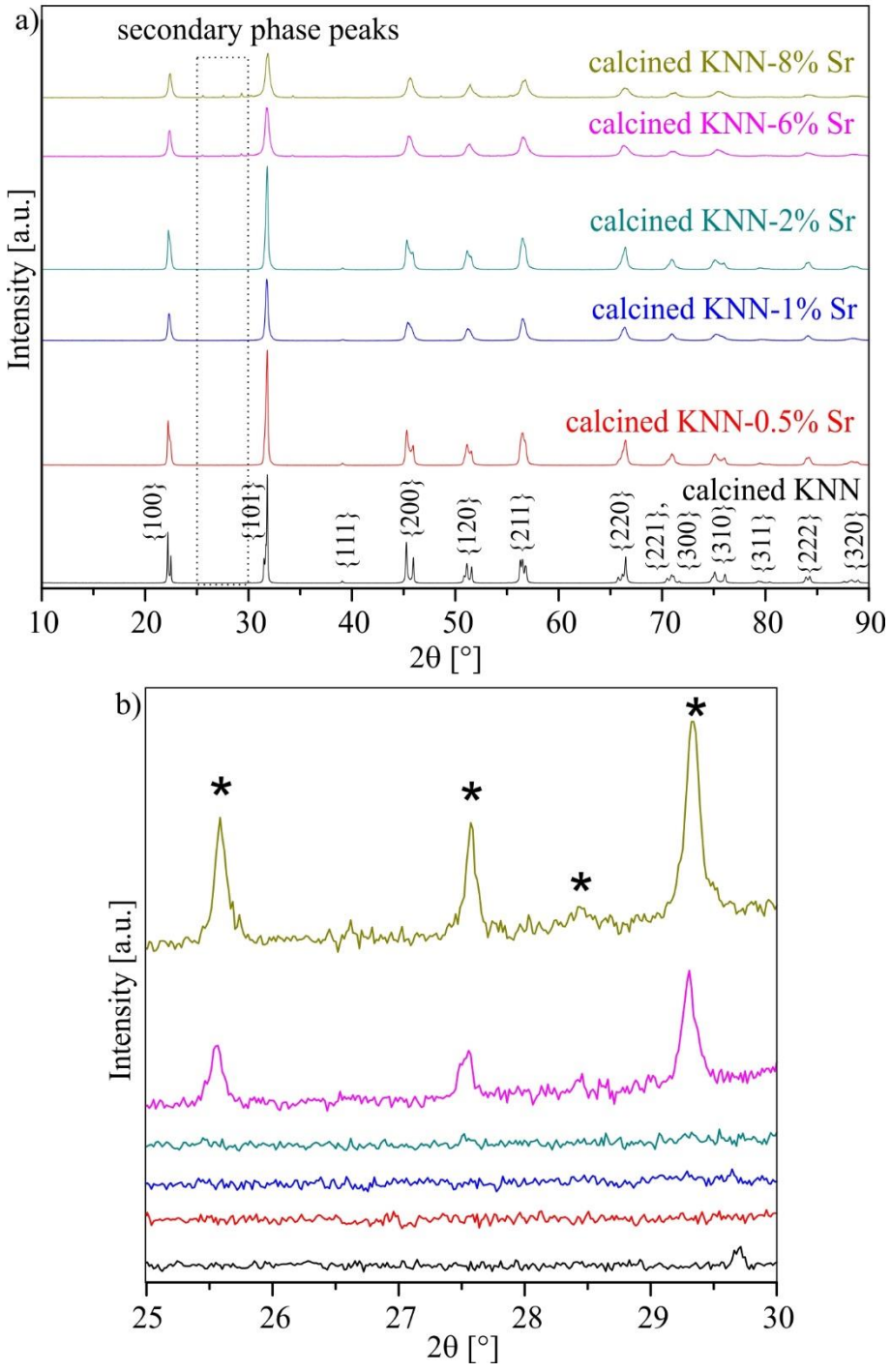


Figure 4.26: XRD of the ceramic powders after the first calcination. a) the whole range of the spectra with the marked peak families, the dashed line marks the area that is magnified in b) to better reveal the peaks of the secondary phase. The secondary-phase peaks are visible for the calcined KNN-6% Sr and the calcined KNN-8% Sr, marked with *.

4.3 The Influence of Sr Doping on the KNN Ceramics

In this section, the effects of Sr doping of KNN on the microstructure and structure of the sintered samples are described. Next, in order to understand the cause of these effects, the compositional homogeneity of the samples is studied. And finally, the investigation of the materials on the atomic level brings an explanation for the observed doping effects.

The samples in this part of thesis are denoted as: KNN, KNN-0.5% Sr, KNN-1% Sr, KNN-2% Sr, KNN-6% Sr, which were all sintered at 1120°C, 2 h in air. Samples with 6 and 8% Sr are also marked as KNN-6% Sr-1140 and KNN-8% Sr-1140, as long as they were sintered at 1140°C, 2 h.

4.3.1 Impact of Sr dopant on the microstructure and crystal structure

At first, the samples of the sintered ceramics were investigated from the point of view of changes of structure and phase composition related to the amount of the Sr-dopant. The results from the conventional XRD analysis together with the synchrotron XRD and the Rietveld refinement of both are presented and discussed together with the microstructural analysis results performed by SEM and TEM.

The XRD of the samples in Figure 4.27 show single-phase perovskites with marked monoclinic unit-cell peaks Figure 4.27a) for the samples up to 2% Sr. The KNN-6% Sr and KNN-8% Sr contain secondary phase, which is marked by stars in Figure 4.27c. These peaks correspond well to one of the polyniobate tetragonal tungsten bronze phases, e.g., $K_6Nb_{10.88}O_{30}$ (ICDD, PDF: 01-087-1856), $K_{5.75}Nb_{10.85}O_{30}$ (ICDD, PDF: 00-038-0297) or $KSr_2Nb_5O_{15}$ (ICDD, PDF: 00-034-0108). The Figure 4.27b shows the decreasing XRD peak splitting with the increasing Sr-concentration. This corresponds to the changing of the cell parameters, i.e., with the increasing Sr-content, the a, c and β decrease, while the b increases (see Table 4.4), which suggests the decrease of the monoclinic unit-cell distortion a/b, i.e., the tendency towards pseudocubic syngony.

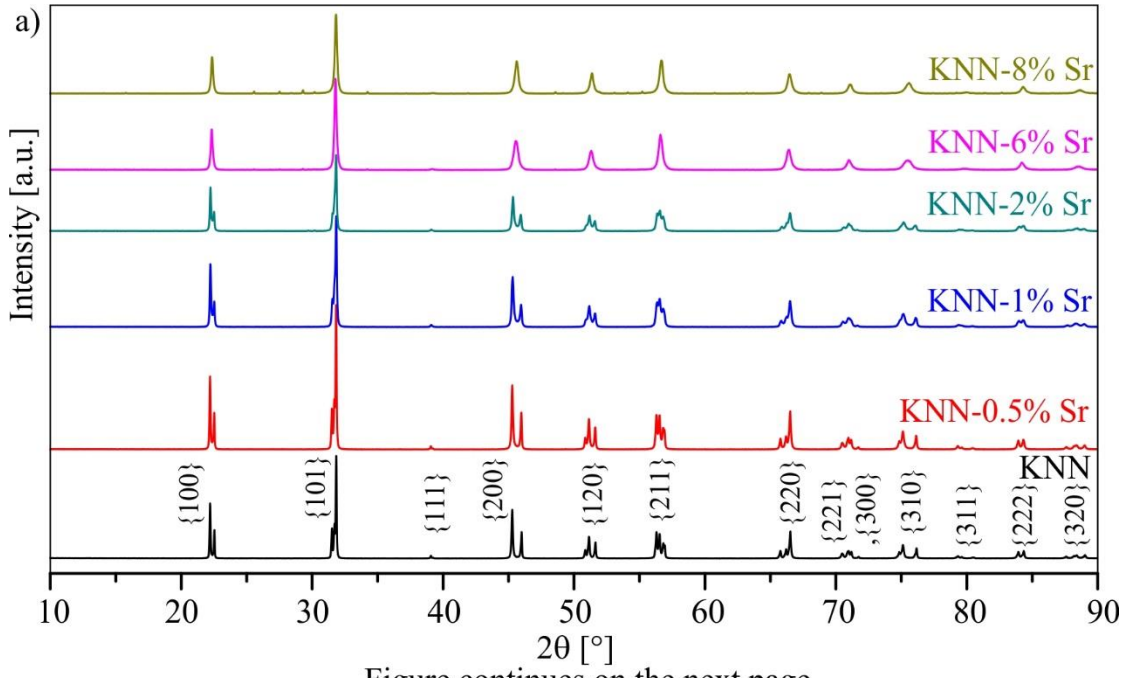


Figure continues on the next page

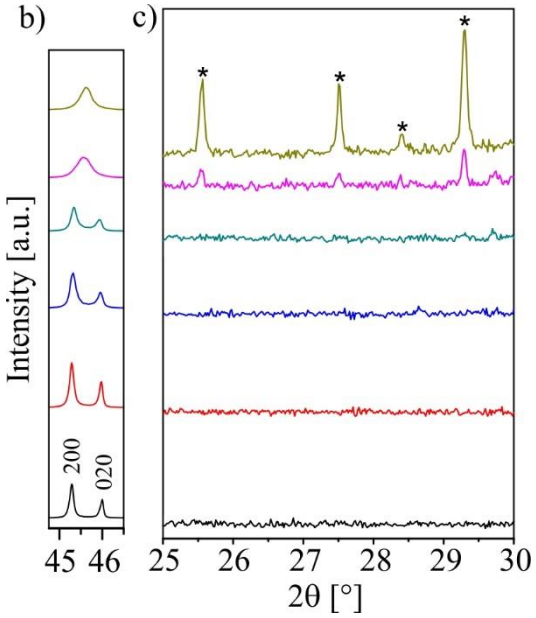


Figure 4.27: XRD spectra of the samples. The diffraction peaks are indexed according to the monoclinic unit cell [32] a) XRD spectra in the range 10–90° 2θ b) focus on the splitting of the {200} peaks family c) XRD spectra in the range 25–30° 2θ with the secondary phase peaks visible for the KNN-6% Sr and KNN-8% Sr. The secondary phase peaks are marked with *****.

In Figure 4.27b, besides the (200) and (020) peaks merging into a single one with the increasing amount of Sr, a gradual peak broadening can be observed as well. From the point of view of the sample's properties, the broadening of the XRD peaks can occur due to the increasing microstrain, decreasing crystallite size or inhomogeneities in the structure or the composition. On the other hand, the XRD peak broadening can also be caused by the limits of the instrumental resolution and such effects become important if the sample has a crystallite size below 100 nm [97].

Table 4.4: Unit-cell parameters of the Sr-doped KNN samples. The values are obtained with the Rietveld refinement of the XRD spectra from Figure 4.27, using the monoclinic unit cell [32]. The R_{wp} factor marks the quality of the fit.

	a (Å)	b (Å)	c (Å)	β (°)	volume (Å^3)	a/b (–)	R_{wp} (%)
KNN	4.00459(8)	3.94535(4)	4.00095(7)	90.3302(8)	63.212(2)	1.015	14.00
KNN-0.5% Sr	4.00375(6)	3.94596(4)	3.99938(7)	90.3228(8)	63.184(2)	1.015	12.55
KNN-1% Sr	4.0025(1)	3.94943(7)	3.9966(1)	90.287(1)	63.175(3)	1.013	13.32
KNN-2% Sr	3.9999(1)	3.95128(7)	3.9943(1)	90.270(2)	63.128(3)	1.012	13.82
KNN-6% Sr	3.9944(1)	3.9533(2)	3.97634(9)	90.184(2)	62.792(3)	1.010	9.65
KNN-8% Sr	3.9867(2)	3.9601(3)	3.9712(2)	90.084(8)	62.696(5)	1.007	13.31

In order to avoid any possible instrumental contribution to the line broadening, a synchrotron XRD was recorded as well. As shown in Figure 4.28a, the peak broadening upon the increasing Sr content is also observed when the samples are measured by the synchrotron XRD.

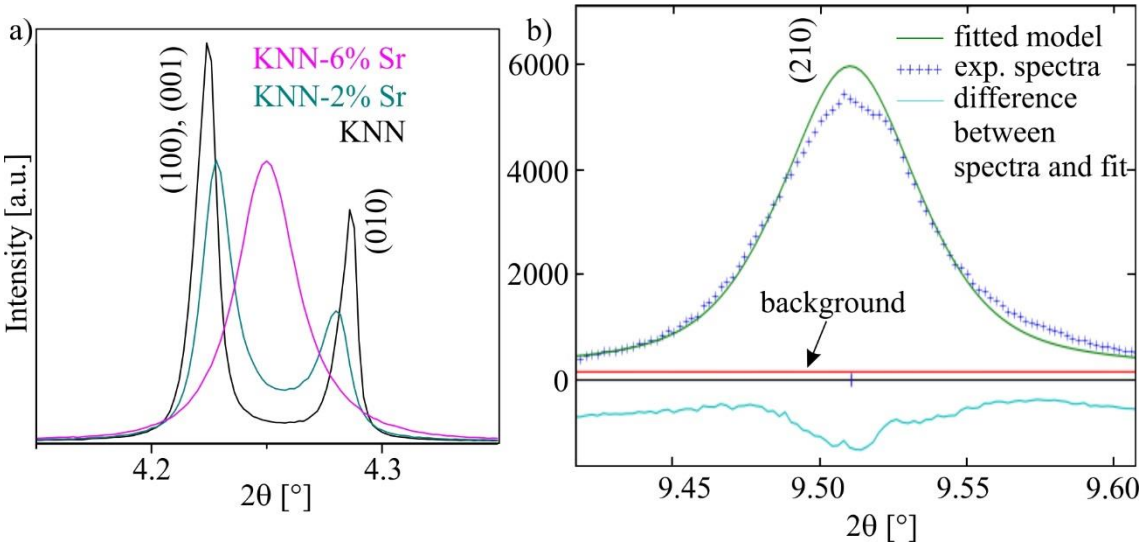


Figure 4.28: Synchrotron XRD spectra of the samples. Please note, that the different 2θ values are due to a different wavelength of the synchrotron radiation compared to the conventional XRD source a) {100} peaks for KNN, KNN-2% Sr and KNN-6% Sr b) the refined model of the KNN-6% Sr XRD spectra at higher 2θ, demonstrating the irregular shape of the (210) peak.

The Rietveld refinement of the synchrotron XRD data was used to determine the microstrain and size of the crystallites in KNN, KNN-2% Sr and KNN-6% Sr. The results are summarized in Table 4.5.

Table 4.5: Rietveld refinement of the synchrotron XRD data. Table sumarizes the used structure and model as well as the results of the crystallite size and microstrain, complemented with the R_{wp} factor describing the quality of fit.

	Syngony	Model	Crystallite size (Å)	Microstrain (–)	R_{wp} (%)
KNN	monoclinic	isotropic	2129(12)	0.000640(1)	~14
KNN-2% Sr	monoclinic	isotropic	1454(7)	0.000940(1)	~14
KNN-6% Sr	cubic	anisotropic	826(4)	0.005160(6)	~20

As shown in Table 4.5, with the increasing amount of Sr dopant, the microstrain increases and the crystallite size decreases. This effect is especially significant for the KNN-6% Sr. Adding the dopant apparently starts to break down the grains into smaller crystallites, i.e., diffraction coherent domains. For the KNN-6% Sr, the crystallite size is extremely low and the microstrain is very high, which signifies a lower crystallinity and therefore means, that the sample contains a lot of crystal disorder.

The MAUD package [82] isotropic model was used for the Rietveld refinement of KNN and KNN-2% Sr, which means the crystallites' shape corresponded the best to the shape of a sphere. The fitting resulted in the R_{wp} ~14 % for KNN and KNN-2% Sr. For KNN-6% Sr, at least a first-order anisotropy had to be introduced, because the crystallite shapes appeared to fit better to the shape of an ellipsoid, so the Popa model for anisotropic broadening available within the MAUD package [82] was used. Despite the modified model, the R_{wp} is relatively high for this sample, i.e., ~20 %, which is evident from the green line denoting the difference between the spectra and the fitted model (see Figure 4.28b). This is because of the irregular peak shape of some of the KNN-6% Sr peaks, as seen in Figure 4.28b. The origin of the irregular peak shape is probably related to the presence of the tetragonal tungsten bronze phase in KNN-6% Sr (see Figure 4.27c).

The Figure 4.29, left-hand column, shows the SEM micrographs of the thermally etched samples with marked average grain size with the values' standard deviation. A gradual, though significant average grain-size decrease, is evident, i.e., from up to ten-microns-sized KNN grains down to few-tens-of-nm-sized grains in the samples with 6 and 8% Sr (see the grains marked

black). The images on the right in Figure 4.29 show the polished surfaces with the BSE detector and such reveal the decrease of the pore-size with the increasing amount of Sr. As marked on the images on the right, all the samples had densities above 90 %TD. The stable values during the Archimedes density measurement confirmed, that samples had closed porosity. The BSE images of the polished KNN-6% Sr-1140 and KNN-8% Sr-1140 reveal the content of a bright-contrast secondary phase (Figure 4.29, KNN-6% Sr-1140 and KNN-8% Sr-1140, inset, marked red), which is present in locally concentrated inclusions in KNN-6% Sr-1140 and in smaller, but more dispersed, inclusions in KNN-8% Sr-1140.

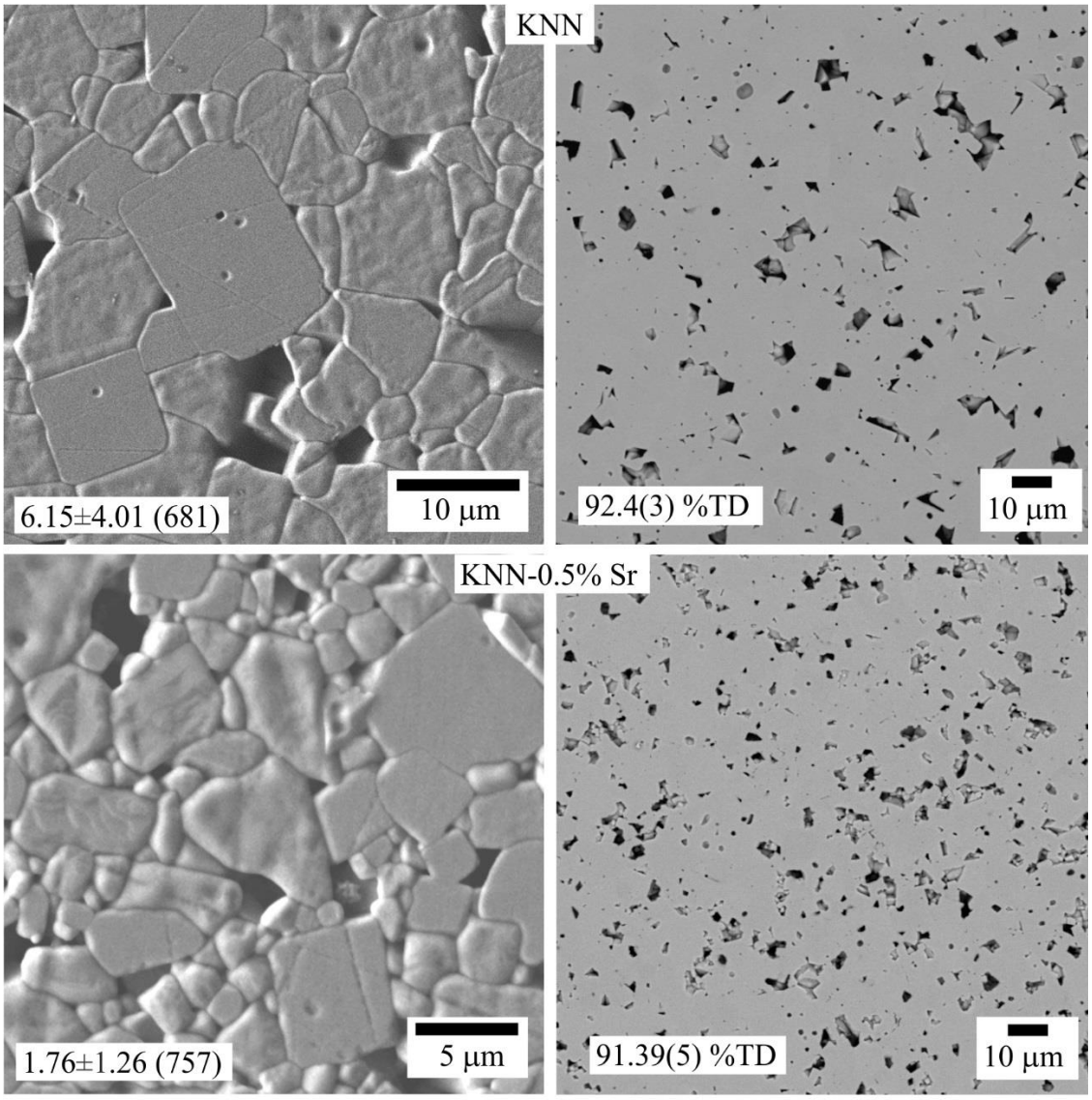


Figure continues on the next page

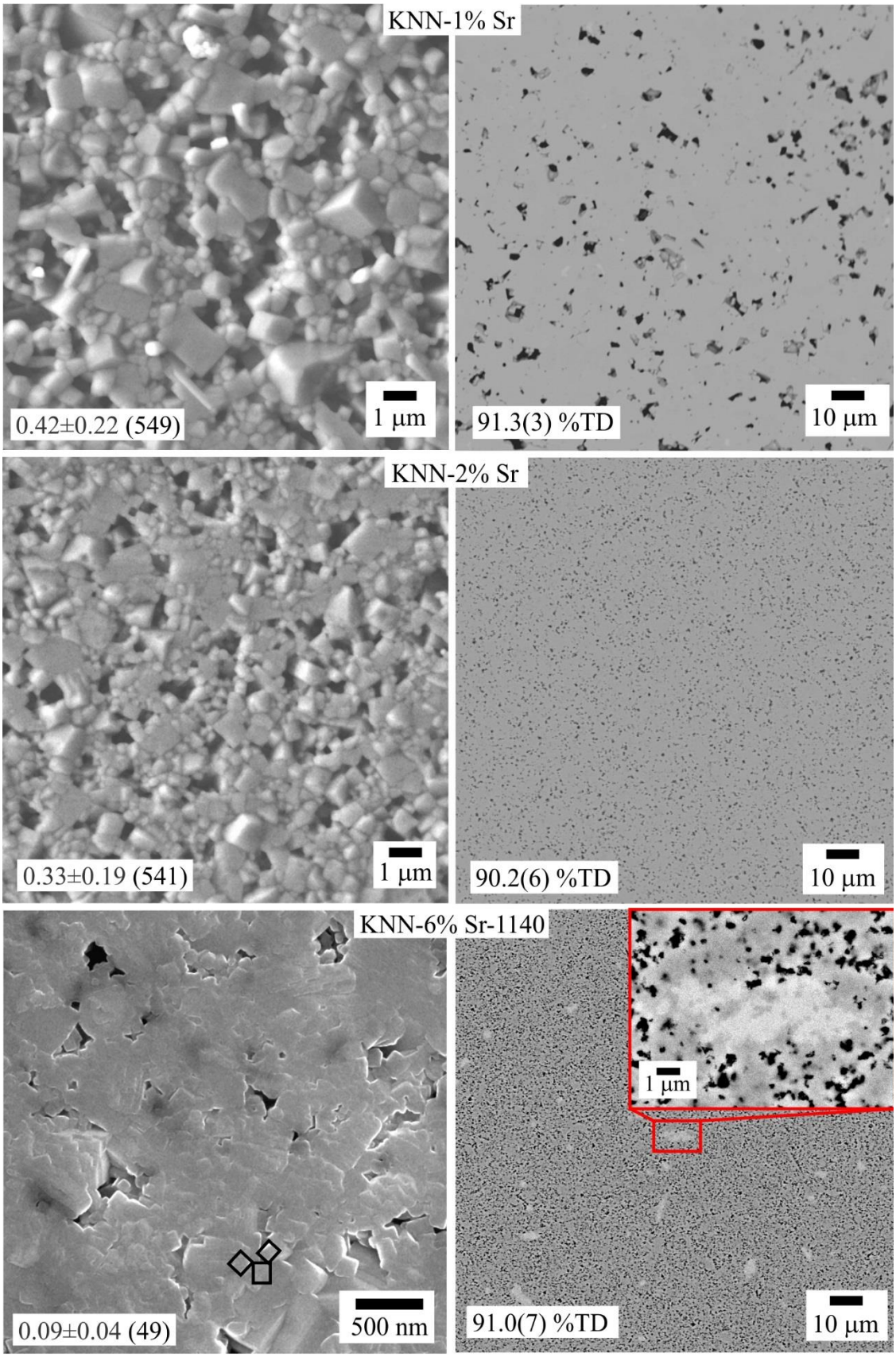


Figure continues on the next page

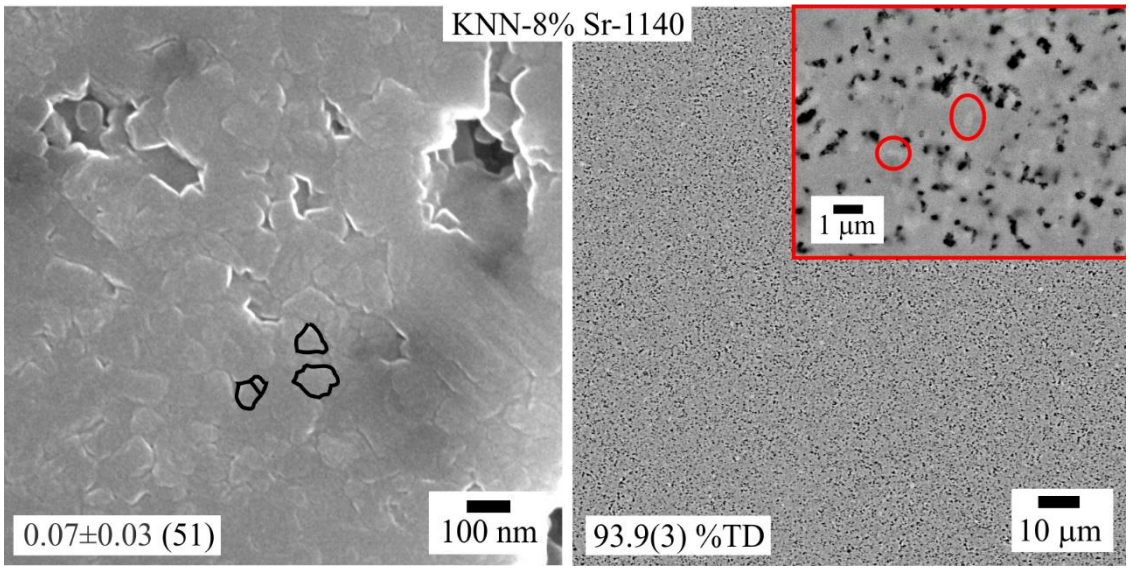


Figure 4.29: SEM micrographs of the KNN, KNN-0.5% Sr, KNN-1% Sr, KNN-2% Sr, KNN-6% Sr-1140 and KNN-8% Sr-1140. For each composition, the image on the left shows an etched sample in SEI mode and the image on the right shows BSE image of the polished sample. The average grain size is marked on the image on the left together with the standard deviation as it was evaluated based on the SEM micrographs for KNN, KNN-0.5% Sr, KNN-1% Sr and KNN-2% Sr and based on the TEM micrographs for KNN-6% Sr and KNN-8% Sr (not shown). For better visibility, the grains of the typical size are marked black in KNN-6 and 8% Sr. The densities are marked on the image on the right. The insets for KNN-6 and 8% Sr show the polyniobate secondary phase with whiter contrast (marked red).

Figure 4.30 presents the TEM micrographs of the samples that were also analysed with the synchrotron XRD analysis (see Table 4.5). The images show the domains in the samples. While the KNN possesses domains of around 200 nm and the KNN-2% Sr contains domains of sizes between 100 and 200 nm, the KNN-6% Sr has monodomain grains.

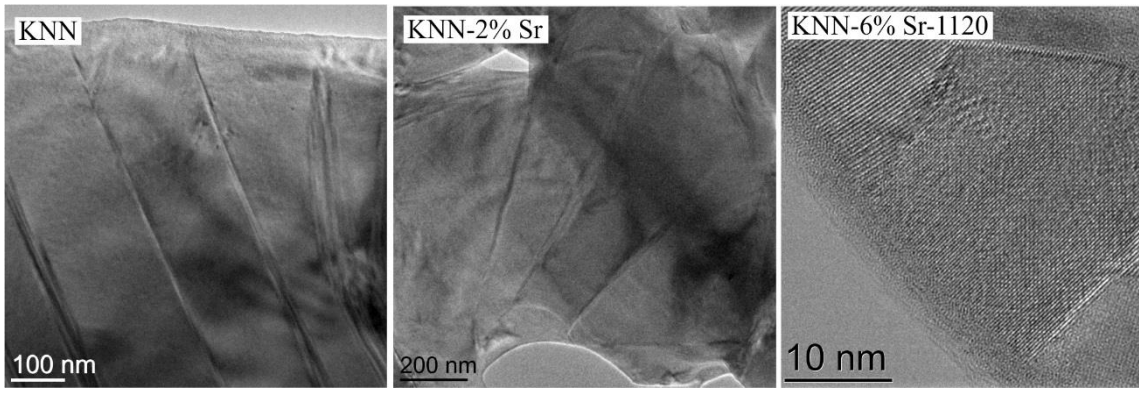


Figure 4.30: TEM micrographs of the KNN, KNN-2% Sr and KNN-6% Sr. The images show the domain structure, with the KNN-6% Sr showing monodomain grains.

As was previously reported by Randall et al. [98], in the grains with the sizes below 1 µm, the grain boundaries cause domain-wall clamping, which is demonstrated in a relative increase in the domain density. The latter results in the domain width and therefore domain variants' reduction. This is consistent with the KNN-6% Sr-1140, where the grain size is of the order of tens of nm (Figure 4.29), as well as the crystallite (Table 4.5) and domain sizes (Figure 4.30).

Since all the effects discussed above are interconnected, the structural and microstructural changes upon Sr-doping are summarized in Figure 4.31. The decrease of the monoclinic unit-cell distortion and the grain-size decrease with the increasing content of Sr are in agreement with

what was previously reported [77]. Also, the increasing amount of Sr results in a crystallite size decrease together with an increase of the microstrain.

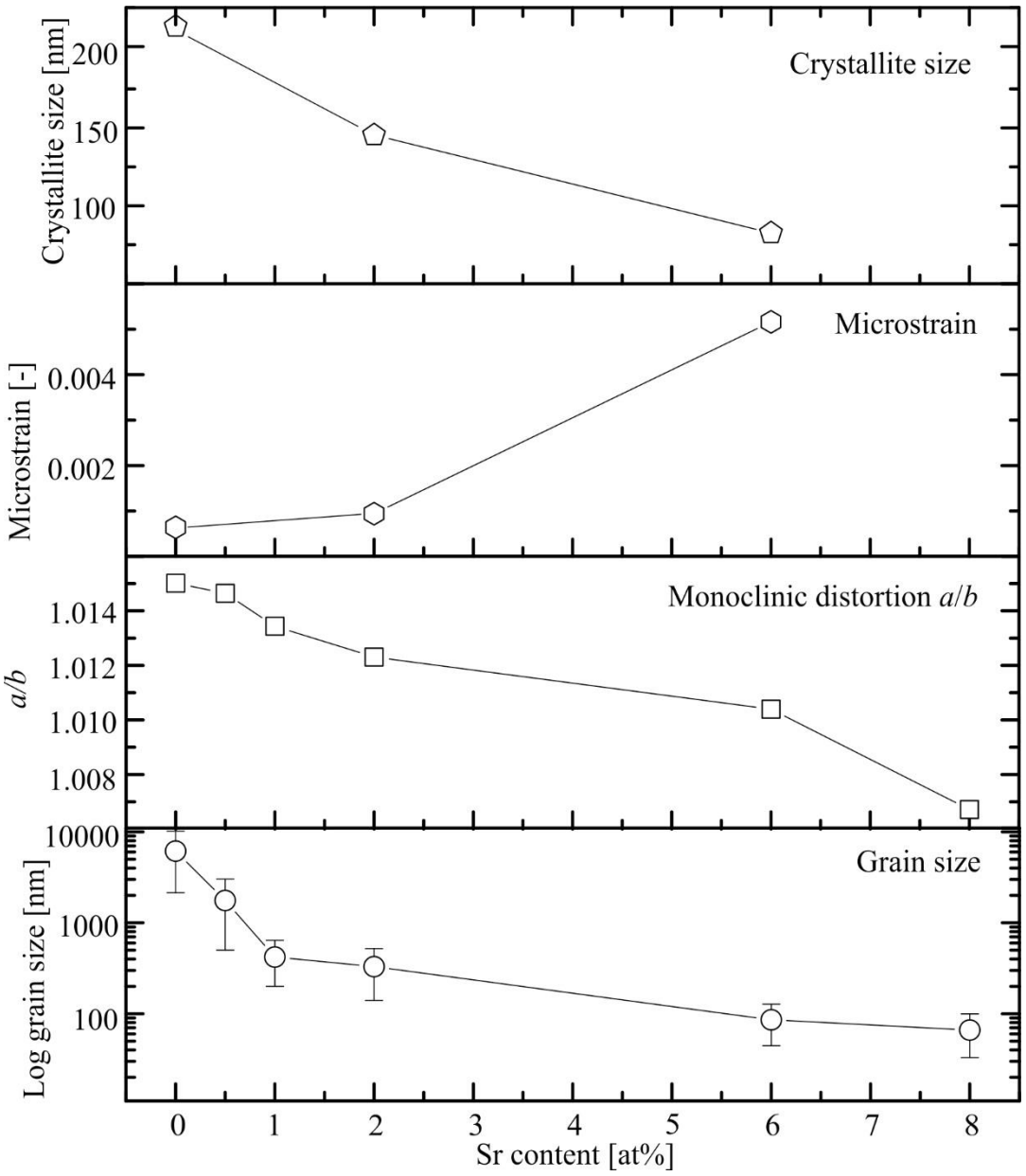


Figure 4.31: Structural and microstructural changes in KNN with increasing Sr-content. The error bars for the monoclinic distortion a/b, microstrain and crystallite size are less than 1% and therefore are hidden within the symbols. The error bars for the grain size show the standard deviation. The lines between the symbols are guide to the eye.

To further analyse the secondary phase with white contrast from Figure 4.29, KNN-6% Sr-1140 and KNN-8% Sr-1140, SEM-EDXS analyses of the phase were performed. Figure 4.32 presents the EDXS spectra of the secondary phase and the matrix area analysed in KNN-6% Sr-1140. The secondary phase is poor in Na (see the intensity of the Na K$\alpha_{1,2}$ line in Figure 4.32) while relatively rich in Nb, similar to the secondary phase identified in undoped KNN by Jenko et. al. [29]. Moreover, this phase appears to have a depletion of Sr compared to the matrix (see the intensity of the Sr Lα_1 line in Figure 4.32).

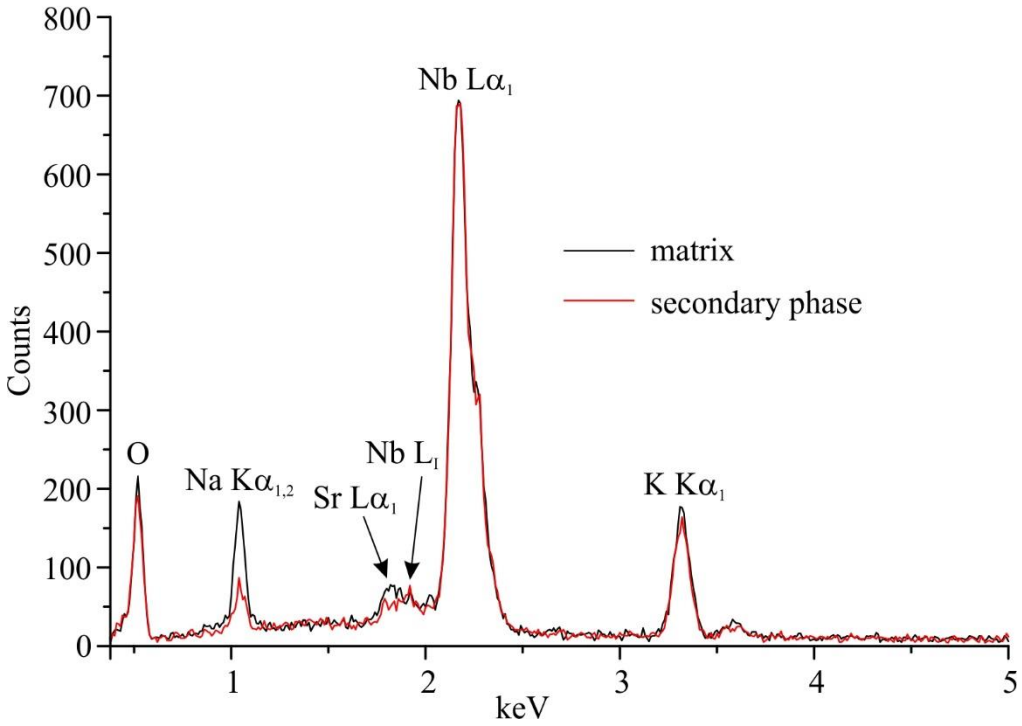


Figure 4.32: EDXS spectra of the matrix and secondary phase in KNN-6% Sr-1140. The spectra of the secondary phase is the analysis of the white-contrast area marked in red in Figure 4.29, KNN-6% Sr-1140.

In order to correctly understand the spectra in Figure 4.32, it is necessary to discuss the following methodological specifics of the SEM-EDXS method in combination with the analysed materials.

When using SEM for the electron-probe microscopic analysis, there is a limitation in the interaction volume for the field-emission SEM at 15 keV, which is around a 3.8 µm interaction depth [33], which results in much larger interaction volume than a single matrix grain of an average size of the order of tens of nm. The analysed area of the matrix in the KNN-8% Sr-1140 therefore includes many matrix grains together with the grain boundaries and similarly, the analysis of the secondary phase might include some of the matrix grains (see Figure 4.29, KNN-8% Sr-1140, image on the right, inset). In order to precisely determine the composition of the secondary phase, the EDXS on the TEM was employed, since, due to a narrow probe and thin specimen, it allows a precise selection of the analysed phase in the analysed area.

Figure 4.33 presents the KNN-6% Sr-1140 having a relatively large crystal of the secondary phase (Figure 4.33, red arrow) among the matrix grains. The elemental ratio of the K:Na:Sr:Nb:O was determined to be 4.2 : 1.8 : 0.0 : 11.7 : 32.3. The A/B ratio was therefore 0.51, which best corresponds to the polyniobate tetragonal tungsten bronze phase $K_{5.75}Nb_{10.85}O_{30}$ (ICDD, PDF: 00-038-0297) (the A/B ratio is 0.53) with some Na included. The amount of Sr detected in the secondary phase by the TEM-EDXS quantitative analysis was well below the detection limit.

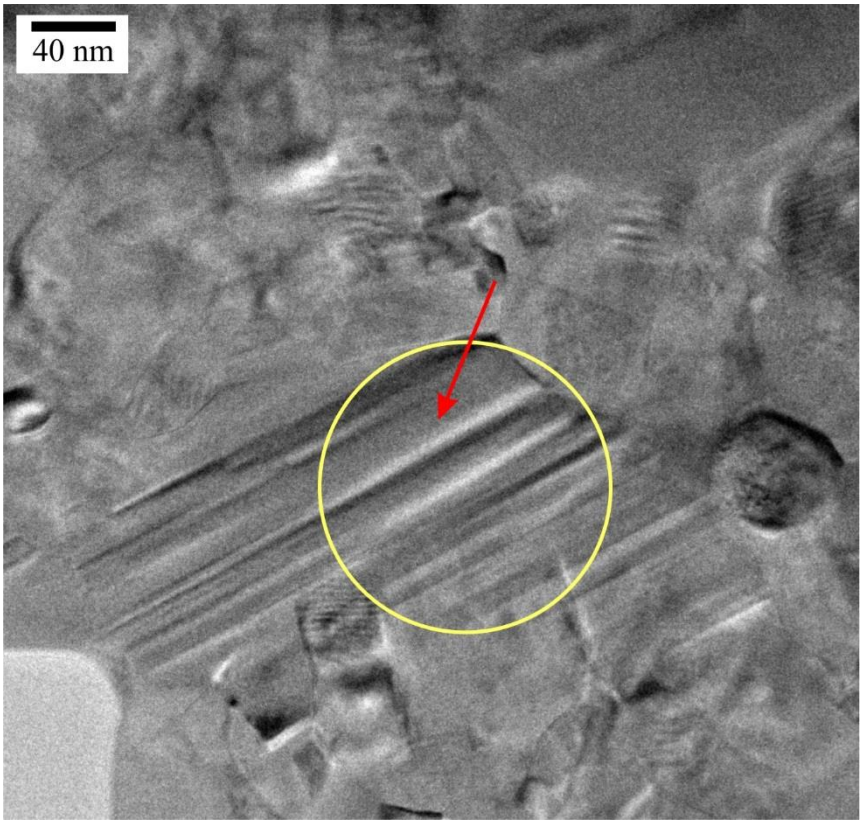


Figure 4.33: TEM micrograph of the KNN-6% Sr-1140. The secondary-phase crystal is marked with a red arrow. The yellow circle marks the area of the EDXS analysis.

A similar phase in KNN was reported to be formed after long-term annealing at high temperatures, as a consequence of the alkalines evaporation [55]. However, as was shown in Figure 4.24, KNN-6% Sr, the secondary phase forms already during annealing at 650°C and forms only for the samples with more than 2% Sr (Figure 4.26). The secondary phase in KNN was also reported to form upon the A-site donor doping [76, 77, 99] and was suggested to be a consequence of reaching the solubility limit of the dopant in the ceramics [99]. However, as was proved by the TEM-EDXS analysis, Sr is present in the secondary phases in a negligible amount.

In order to better understand the influence of Sr-doping on the structural changes and the influence of the secondary phase on the structure, Raman spectroscopy was performed on the KNN, KNN-0.5% Sr, KNN-2% Sr and KNN-8% Sr. Figure 4.34 presents the Bose-Einstein-corrected Raman spectra, which were measured at 80 K, with a Raman modes assignment. While the modes below 200 cm^{-1} are assigned as translational modes of K^+/Na^+ cations, i.e., A-site modes [75, 100, 101], the modes above 200 cm^{-1} are the internal vibrational modes of NbO_6 octahedra [34, 75]. According to Kakimoto et al. [75], the ν_1, ν_2 and ν_5 modes are breathing or bending modes of the NbO_6 octahedra and modes ν_3 and ν_4 are stretching and bending modes of the Nb-O bond.

As seen in Figure 4.34, the spectral signature considerably changes with the increasing Sr-content, i.e., the spectra broadens and there is an appearance of a central mode, which is an indication of a dynamic disorder typical for the proximity of a cubic phase. The gradual tendency of the KNN samples towards the pseudocubic syngony with the increasing Sr-content is also demonstrated in the decreasing monoclinic distortion a/b obtained with the Rietveld refinement of the XRD spectra (Table 4.4). Modes ν_1 and ν_5 at ~600 cm^{-1} and ~270 cm^{-1}, respectively, undergo slight blue-shifting upon increasing Sr-content, which suggests increased chemical pressure on the NbO_6 octahedra upon the A-site substitution with Sr. This phenomenon is in agreement with the increased intensity of the A-site mode at ~100 cm^{-1}, which has also been assigned by Kakimoto et al. [75] to the increasing A-site substitution effects in KNN doped with Li. In the samples discussed in this thesis, these effects are significant, but show a

consistent trend with the Sr-content only up to 2% Sr for both Raman and XRD spectra (see also Figure 4.34, Figure 4.27a,b). For the KNN-8% Sr (Figure 4.34, KNN-8% Sr), the intensity of the mode at ~100 cm^{-1} decreases again and the modes ν_1 and ν_5 shift back.

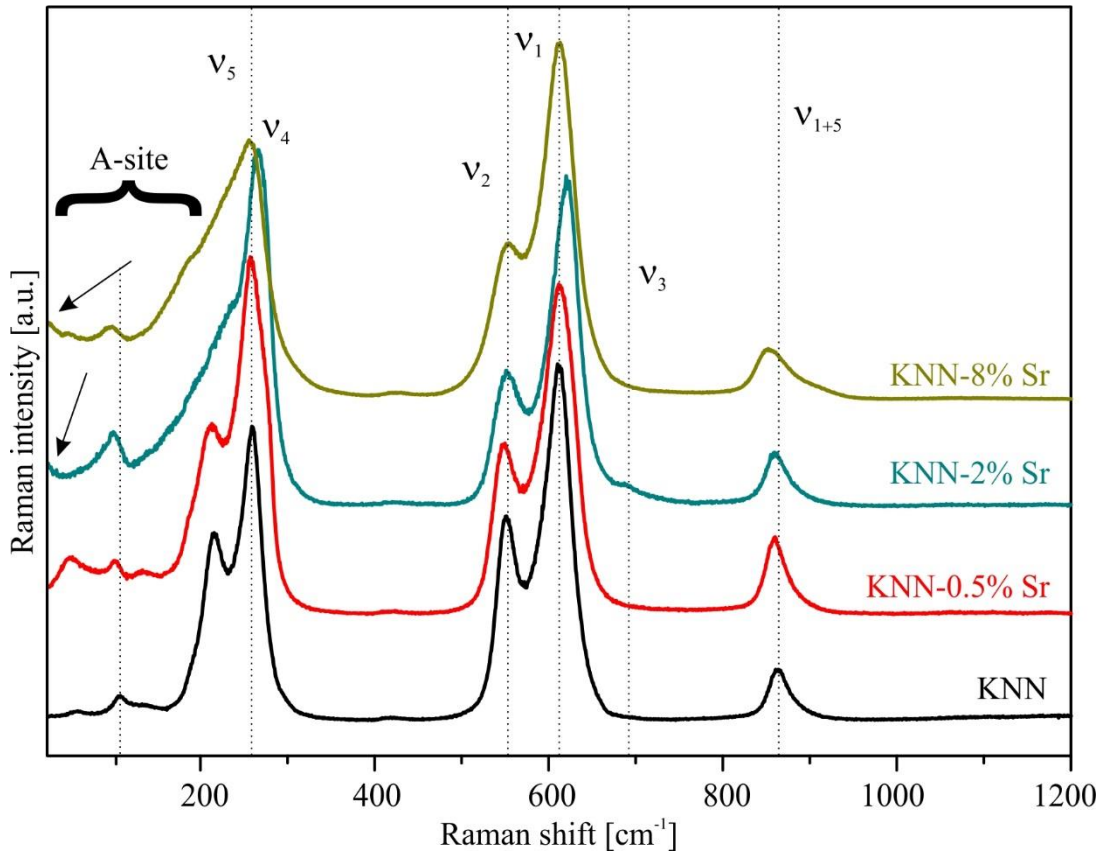


Figure 4.34: Raman spectra measured at 80 K for KNN, KNN-0.5% Sr, KNN-2% Sr, KNN-8% Sr. Arrows mark the central mode. The ν_{1-5} mode assignments are marked above the spectra.

The formation of the secondary phase in the KNN-8% Sr would cause both a release in the chemical pressure and an additional broadening of the Raman spectra (see Figure 4.34), which would reduce the relative intensity of the A-site modes in the Raman spectra. Also, it should be taken into account, that the tetragonal tungsten bronze structure with *P4/mbm* symmetry has up to 44 Raman-active modes [102], compared to the 33 Raman-active modes of the monoclinic KNN at room temperature [34]. The modes number increase is related to the superposition of a relatively small amount of the secondary polyniobate tungsten bronze phase on the spectrum of the monoclinic KNN. Therefore, the spectrum of the polyniobate tungsten bronze phase is not visible and it contributes only to the modes' broadening observed for the samples with more than 2% Sr.

Figure 4.35 shows the Raman spectra of the KNN, KNN-2% Sr and KNN-8% Sr as a function of temperature. The typical sequence of phase transitions can be identified in the undoped KNN: rhombohedral (R) to monoclinic (M) around -95°C and M to tetragonal (T) around 185°C. These transitions are evident from the shifts of the ν_1 to ν_5 modes, at ~600 and ~250 cm^{-1}, respectively (see Figure 4.35, vertical lines) [39, 103]. The transition to the cubic phase occurs around 395°C and is seen as the disappearance of all the modes and the appearance of two broad features at 250 and 600 cm^{-1}, which underline the presence of lattice disorder allowing Raman activity in the high-temperature phase. The low-temperature transition around -175°C has not been previously reported. Considering that the R-M transition should display a very broad hysteresis [39], the observed spectral changes are probably related to the short-range nucleation of monoclinic islands within the rhombohedral phase.

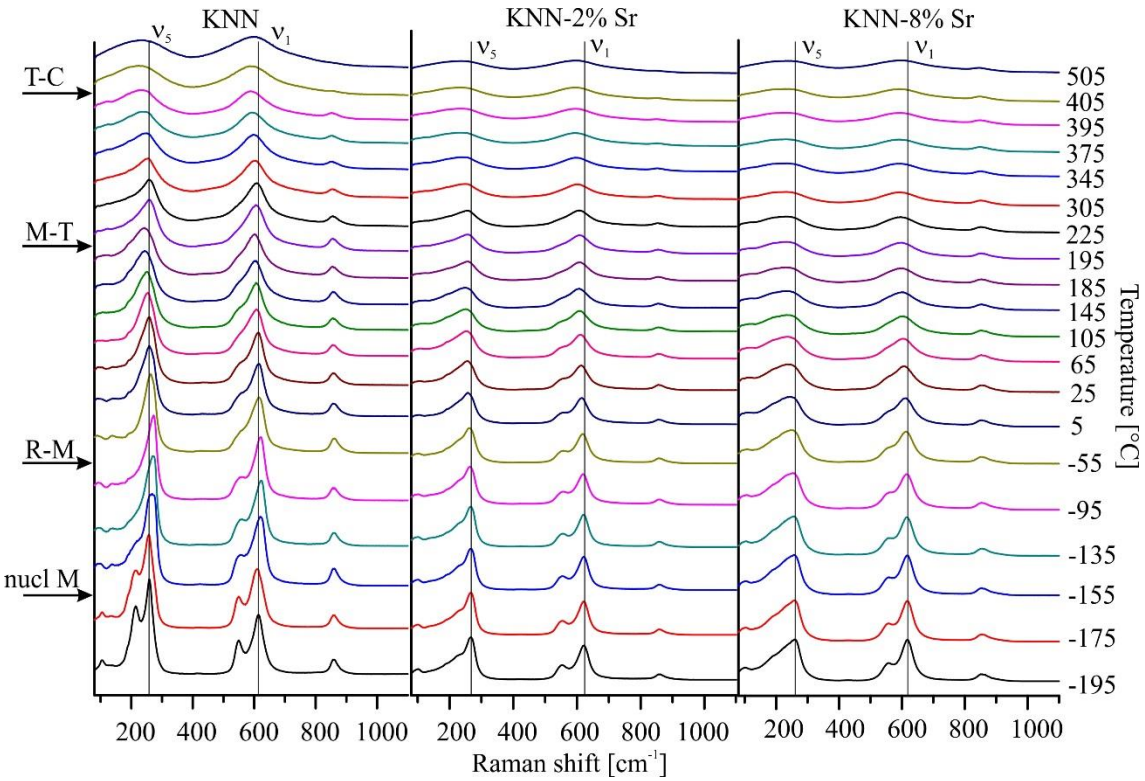


Figure 4.35: Temperature-dependent Raman spectra for KNN, KNN-2% Sr and KNN-8% Sr. Phase-transition temperature intervals are marked with arrows. T is for tetragonal, M is for monoclinic, R is for rhombohedral and nucl M refers to the nucleation of the monoclinic clusters within the rhombohedral phase. Vertical lines mark the ν_1 and ν_5 modes.

The effect of the A-site substitution is also evident in the function of temperature, i.e., the phase transitions become diffuse with the increasing Sr-content. This occurs in the material with 2% Sr as a broadening of the thermal range of the phase transitions. In the KNN-8% Sr, the phase transitions are diffuse and the transition temperatures are barely distinguishable. Notably, in this composition the $\nu_1 + \nu_5$ mode at ~850 cm^{-1} does not disappear in the cubic phase, which means that a fraction of the tetragonal material is still present at higher temperatures.

Based on the samples' formulation, i.e., $K_{0.5-2y}Na_{0.5-2y}Sr_yNbO_3$, one A-site vacancy is introduced per atom of Sr. The A/B ratio is therefore lower than in the undoped KNN, i.e., lower than 1. Lowering of the A/B ratio in KNN can be compensated by the formation of a polyniobate tetragonal tungsten bronze phase [55, 104]. It should also be noted that the Sr ion has been reported to form a single-phase cubic perovskite Sr_xNbO_3 at as low A/B ratio as 0.72 [105].

4.3.2 Study of the local structure around Sr atom

In the following section, the samples without the secondary phase, i.e., KNN-0.5% Sr, KNN-1% Sr and KNN-2% Sr, were analysed with the Sr K-edge EXAFS analysis. This analysis provides us with an additional view into the local structure around the Sr atoms and thus gives an insight in to the structural changes on the atomic level all over the sample, when introducing Sr in the KNN lattice.

The measured EXAFS spectra (Figure 4.36a) are analysed with the IIFFEFIT package [83] using the FEFF6 code [84] in which the photoelectron scattering paths are calculated *ab initio* from a presumed distribution of neighbouring atoms. The EXAFS model is based on the crystallographic data of the cubic $KNbO_3$ with the *Pm*−3*m* space group (a = 4.002 Å) [32, 106], centered on the K-site and adapted by replacing the central K with Sr and by exchanging half of K neighbour atoms for Na. In this crystal structure the K atoms are coordinated by 12 oxygen atoms at 2.830 Å, 8 Nb atoms at 3.466 Å, and on average 3 K and 3 Na atoms at 4.002 Å.

The first six scattering paths in the R-range up to 4.3 Å are included in the FEFF model: the four single-scattering paths (O, Nb, K and Na) and two triple-scattering paths (-Nb-O-, and -O-O-). Each neighbour element shell is described by two variable parameters: the radius of the shell and the width of the path distribution (Debye–Waller factor) σ^2. The coordination numbers N for each coordination shell are kept fixed at their crystallographic values. In addition, a common shift of the photoelectron zero-energy ΔE_0 and amplitude reduction factor S_0^2 are varied. The same parameters are used for a description of the two multiple-scattering paths. The number of independent free parameters in the fit is reduced by introducing some constraints between the fit parameters of scattering paths: the overall relative expansion coefficient, to describe the variation of the coordination shell radius, except for the Nb shell, where an independent displacement was allowed, and the Debye model to describe Debye–Waller parameters of the Nb, Na and K neighbour shells.

To improve the statistical validity of the fits, all three EXAFS spectra are fitted together in a single combined variation step. In the basic calculation a common set of parameters is used for all three spectra: subsequently, some parameters and their combinations were allowed different values for the three spectra. Regularly, such splitting of the fitting parameters produces very close values in all the spectra, showing that the spectra are, apart from the amount of statistical noise, essentially the same. For all the samples, the quality of fit is convincing as the conventional measure of the quality of fit the R-factor is 0.008, which confirms, that the model of the structure is appropriate (Figure 4.36b). Best fits are obtained in the k range from 2.8 to 10.5 Å^{-1} and the R range from 1.4 to 3.8 Å with S_0^2 = 0.88 ± 0.07 and ΔE_0 = –1.7 ± 0.06 eV.

The values of the structural parameters are quite similar between the samples, certainly within their estimated error ranges, suggesting negligible differences between the samples in the neighbourhood of the dopant atom. This is expected in the measured range of Sr-concentrations. Each Sr atom affects its site in the same way, and they are sufficiently diluted that their interaction can be neglected.

The Table 4.6 presents the results of the fitting of the EXAFS model to the measured Sr K-edge spectra. The coordination numbers of the fitted EXAFS model for all neighbour shells as well as their radii correspond to the crystallographic values for the ABO_3 perovskite A-site (see Table 4.6). Compared to the initial model, the closest neighbours, the 12 O atoms, are at a slightly larger average distance 3.00(2) Å, but the large width parameter ($\sigma^2_{\text{Sr-O}}$ = 0.017 ± 0.004 Å^2) indicates that they are randomly distributed over a broader range of distances around the average value. The distance to the Nb atoms is only changed by 0.03 Å to 3.49 ± 0.02 Å, while the alkali atoms K and Na are pushed away by as much as 0.3 Å to 4.37 ± 0.06 Å. Their width parameters are within the expected limits $\sigma^2_{\text{Sr-Nb}}$= 0.005 Å^2, $\sigma^2_{\text{Sr-K}}$ = 0.009 Å^2, $\sigma^2_{\text{Sr-Na}}$ = 0.013 Å^2), corresponding to crystal Debye temperature of 393 ± 32 K.

Table 4.6: Results of the EXAFS model. The common parameters of the nearest coordination shells around the Sr atom in all KNN-0.5% Sr, KNN-1% Sr and KNN-2% Sr samples: atomic species, coordination number N, distance r and Debye-Waller factor σ^2. The uncertainty of the last digit of r is given in parentheses.

	N	r [Å]	σ^2[Å^2]
O	12	3.00(2)	0.017
Nb	8	3.49(2)	0.005
K	3	4.37(6)	0.09
Na	3	4.37(6)	0.013

It can be concluded that the local structure around the Sr atoms in KNN-0.5% Sr, KNN-1% Sr and KNN-2% Sr is cubic ABO_3, with Sr at the A-site. The mechanism of the charge compensation of the structure, either vacancies at the metal sites or insertion of additional O atoms, cannot be detected since 1% changes in the coordination numbers are involved.

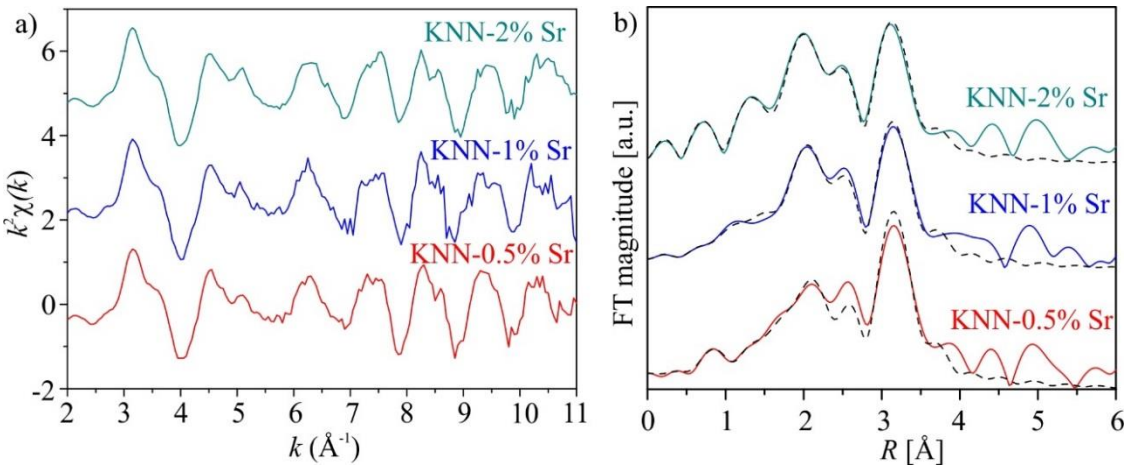


Figure 4.36: EXAFS analysis of the KNN, KNN-0.5% Sr and KNN-2% Sr. The spectra are vertically stacked for clarity a) k^2-weighted EXAFS spectra b) Fourier-transform magnitudes of the k^2-weighted EXAFS spectra (solid coloured lines) together with the best-fit EXAFS model (black dashed lines) calculated in the k-range from 2.8 to 10.5 Å^{-1} and the R-range from 1.4 to 3.8 Å.

4.3.3 Compositional analysis

In this section the chemical composition of the Sr-doped KNN ceramics on the micro-scale is studied, to confirm whether the samples have the nominal composition. The undoped KNN is used systematically, as a reference.

For the verification of the elemental composition, the SEM-WDXS was used, since it brings up to 10-times-better energy-resolution compared to the SEM-EDXS [107]. WDXS thus, when using a standard, provides a precise quantification for the Sr, even in the samples with the lowest amounts of dopant. Nevertheless, the interaction depth of the electron beam with the sample remains the same as for SEM-EDXS, i.e., 3.8 µm, because the standard acceleration voltage used for quantification by SEM-WDXS is also 15 keV. Therefore, only undoped KNN and KNN-1% Sr could be analysed by WDXS without including the grain boundaries, due to the existing grains with sizes above 3.8 µm (Figure 4.29, KNN-1% Sr).

Results from the compositional analysis obtained with standard SEM-WDXS are presented in Table 4.7. The results show, that the at% of elements in the analysed samples are well around the nominal values when taking into account the standard deviation for all the analysed elements (see Table 4.7) and that the standard deviations are similar for doped, as well as the undoped compositions.

Table 4.7: Results from the SEM-WDXS analysis.

		KNN	KNN-1% Sr
K [at%]	Nominal	0.50	0.49
	Experimental	0.51±0.03	0.50±0.03
Na [at%]	Nominal	0.50	0.49
	Experimental	0.50±0.03	0.50±0.03
Sr [at%]	Nominal	-	0.01
	Experimental	-	0.010±0.001
Nb [at%]	Nominal	1.00	1.00
	Experimental	1.02±0.01	1.02±0.01
O [at%]	Nominal	3.00	3.00
	Experimental	2.96±0.02	2.96±0.02

The Figure 4.37 presents the results from the TEM-EDXS quantitative analysis of KNN-1% Sr and KNN-2% Sr, which gives information about the compositional homogeneity of the analysed samples on the nano-level. Since the composition of KNN-1% Sr was previously confirmed as nominal by the standard SEM-WDXS (see Table 4.7), the values were used as an internal standard for the TEM-EDXS quantification of the elements in KNN-1% Sr. The values obtained by the quantification of TEM-EDXS analysis of the KNN-2% Sr were recalculated using the correcting factors for KNN-1% Sr, as a standard sample containing Sr. Figure 4.37 therefore presents the variation of the values of K, Na, Sr and Nb among several analysed spots of ~ 50 nm in diameter within KNN-1% Sr and KNN-2% Sr.

The results in Figure 4.37 show that the K/Na ratio varies among the analysed spots. The scattering of the values for the particular element is similar for KNN-1% Sr and KNN-2% Sr (see Figure 4.37, bands).

Based on the results presented in Figure 4.37, it is difficult to identify any systematic relation between variations of the particular elements from their nominal values. Overall, no concentration gradient, which would suggest a core-shell structure, can be identified within the grains, and at the same time, the deviation from the nominal value for all the elements does not change with the increasing amount of Sr.

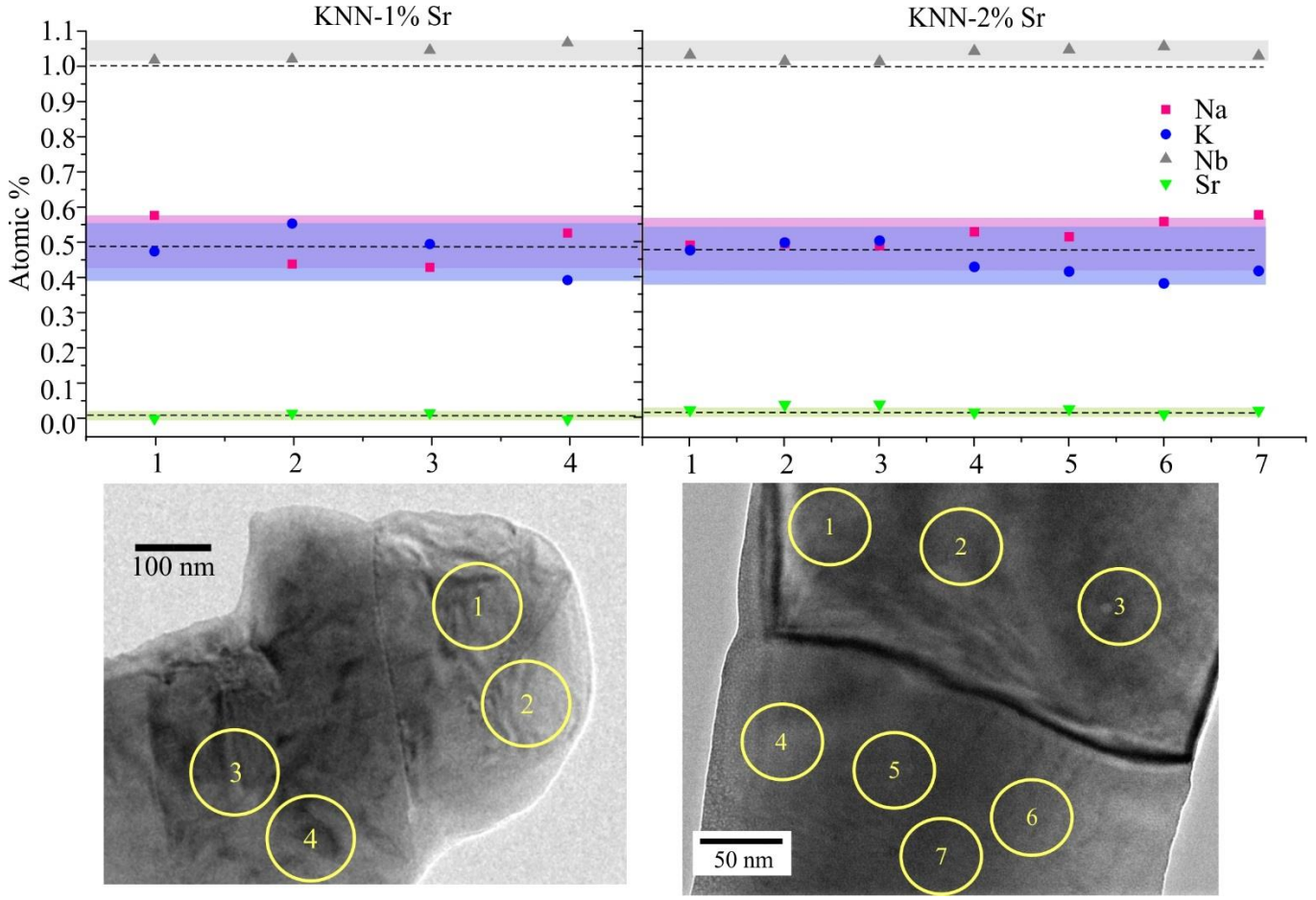


Figure 4.37: TEM-EDXS of KNN-1% Sr and KNN-2% Sr. Upper graphs show the results from the quantitative analysis with the applied correction factor, bands mark the scattering of the obtained experimental values for KNN-1% Sr. Dashed black lines mark the nominal values. Bottom images show the analysed areas.

4.3.4 Grain boundaries investigation on atomic level

The compositional homogeneity of the regions close to the grain boundaries was investigated in the samples with the most pronounced effect of grain-size decrease, i.e., KNN-6% Sr and KNN-8% Sr.

A suitable technique for identifying the differences in the elemental composition near the grain boundary compared to the grains cores proved to be the EDXS line scan with ARM. The Figure 4.38 shows the line scan analysis performed in the KNN-6% Sr of the region close to the grain boundary. The results give comparable elemental levels along all the analysed area.

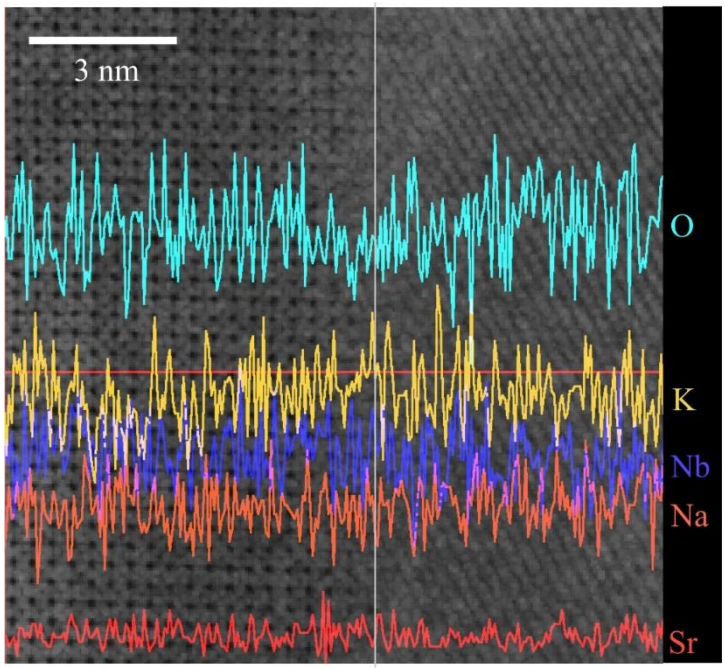


Figure 4.38: Line-scan analysis of KNN-6% Sr. ARM bright-field micrograph with EDXS line scan of the grain-boundary region. The grain boundary is marked with a vertical white line.

Additionally, all the samples were investigated for a possible segregation of Sr, Na, K or Nb near a grain boundary by the HRTEM. The grain boundaries were found to be clean at the nano level, as demonstrated in the examples of KNN-2% Sr and KNN-6% Sr in Figure 4.39. Therefore, no segregation of Sr or any other elements was found with the HRTEM in any of the prepared samples.

Since no significant compositional inhomogeneities in the grain-boundary region were found, the existence of a remarkable compositional gradient or even a segregation of the dopant near the grain boundary were ruled out as reasons for inhibiting the grain growth in the doped samples. Therefore, the grain boundaries were investigated at the atomic level for other phenomena that would limit the grain-boundary mobility.

The theory of the coincidence site lattice explains that the relation between the number of lattice points in the unit cell of a coincidence site lattice (CSL) and the number of lattice points in a unit cell of the lattice being generated is called sigma (Σ). Sigma can also be described as the unit-cell volume of the CSL. Sigma is also related to the grains' misorientation, which is one of the factors that influences the grain-boundary mobility.

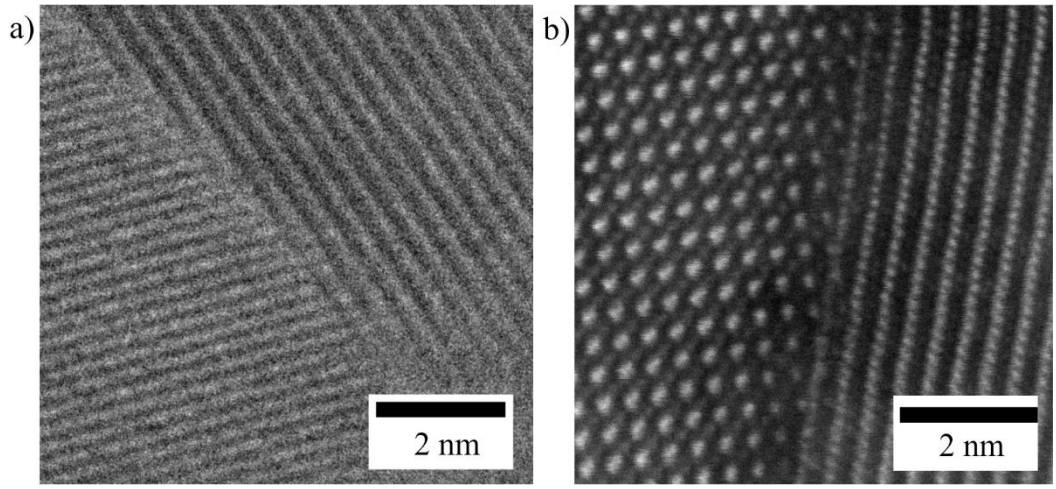


Figure 4.39: HRTEM micrographs of the KNN-2% Sr and KNN-6% Sr a) HRTEM of the KNN-2% Sr b) HAADF-STEM image of the KNN-6% Sr.

Figure 4.40 shows an ARM study of a high-angle grain boundary that was found between two grains with relatively large sizes, i.e., ~200 nm and ~80 nm (see Figure 4.40a) in the KNN-6% Sr. This grain boundary was determined as the $\Sigma 5$ boundary (see the 5 sides of the pentagon marked in white in Figure 4.40b) with the angle close to 37°, which are typical for high-angle grain boundaries.

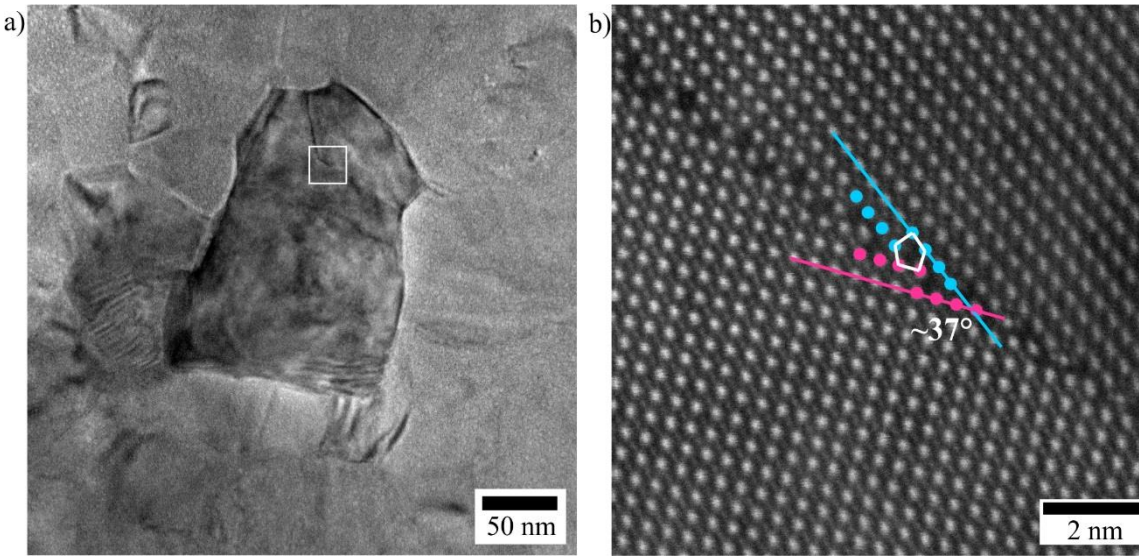


Figure 4.40: ARM study of a grain boundary in KNN-6% Sr a) ARM TEM micrograph of two relatively large neighbouring grains divided by a grain boundary, the marked area is enlarged in b) HAADF-STEM micrograph of a clean high-angle grain boundary with Σ = 5, ~37°.

Figure 4.41, on the other hand, presents a low-angle grain boundary between two relatively fine grains, sized ~20 nm and ~70 nm (see Figure 4.41a) in KNN-6% Sr-1140. The inset in Figure 4.41b shows the misorientation angle between the two grains, which was measured as 2.84° (see Figure 4.41b, inset).

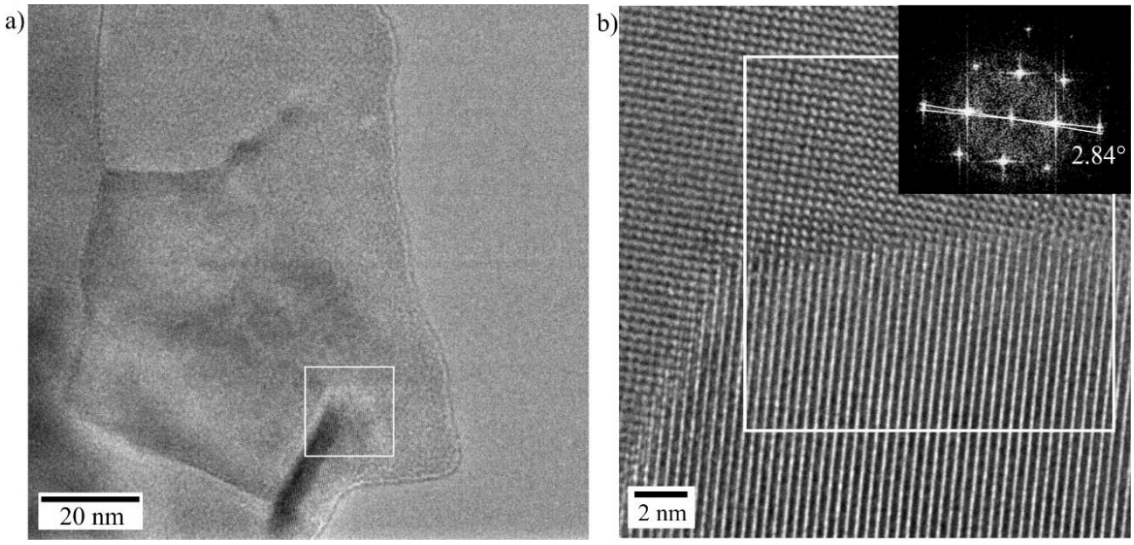


Figure 4.41: TEM study of a grain boundary in KNN-6% Sr-1140 a) TEM image of an area with fine grains with the square marking the area for the HRTEM in b) HRTEM of the low-angle grain boundary present between fine grains. Inset presents the FFT of the area marked in white with the angle between the two grains.

Figure 4.42 presents another example of a low-angle grain boundary with a misorientation angle of 2.34° (Figure 4.42, inset). Similar grain boundaries were found by TEM and ARM in a prevailing amount in the samples with grains that had sizes below 100 nm, i.e., KNN-6% Sr and KNN-8% Sr. On the other hand, only one case of a high-angle grain boundary was identified in all these samples, i.e., the one which is presented in Figure 4.40.

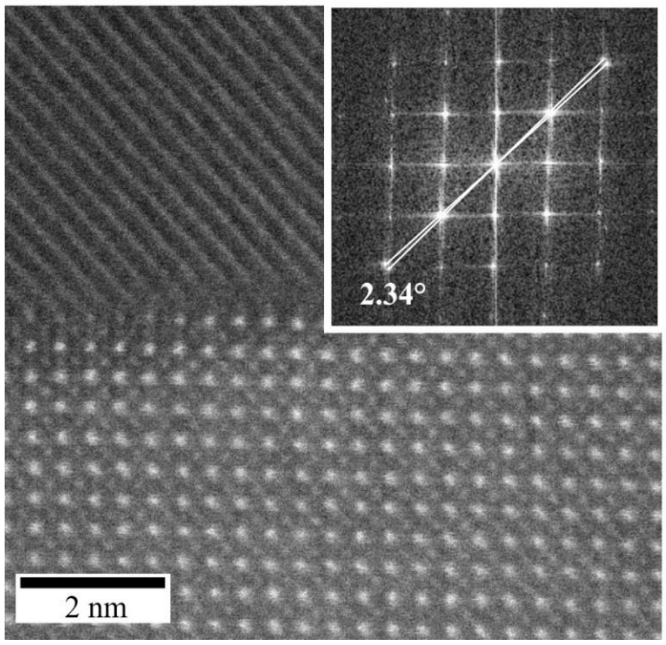


Figure 4.42: HAADF-STEM micrograph of a grain boundary in KNN-6% Sr. The image shows another low-angle grain boundary. The inset presents the FFT of the grain boundary area with the measured misorientation angle.

From the results of the investigation of the grain boundaries in the KNN-6% Sr at the atomic level, presented in Figure 4.40, Figure 4.41 and Figure 4.42, it is clear that the grain-size inhibition is related to the presence of the low-angle grain boundaries, which are known to have very low

mobility. As Doherty et al. explain in their review on the recrystallization of metal alloys [108] the new grains arise from the deformed regions of the microstructure, while keeping the orientation of the deformed state. Although this phenomenon is well studied in metals, the recrystallization of plastically deformed regions has been described for ceramics as well [109].

Figure 4.42 shows a HRTEM micrograph of an area with subgrains, which was commonly found in KNN-6% Sr-1140. The area is divided into several subgrains, which recrystallize from a parent structure and are divided by dislocation grain boundaries (see Moiree patterns dividing particular subgrains in Figure 4.43).

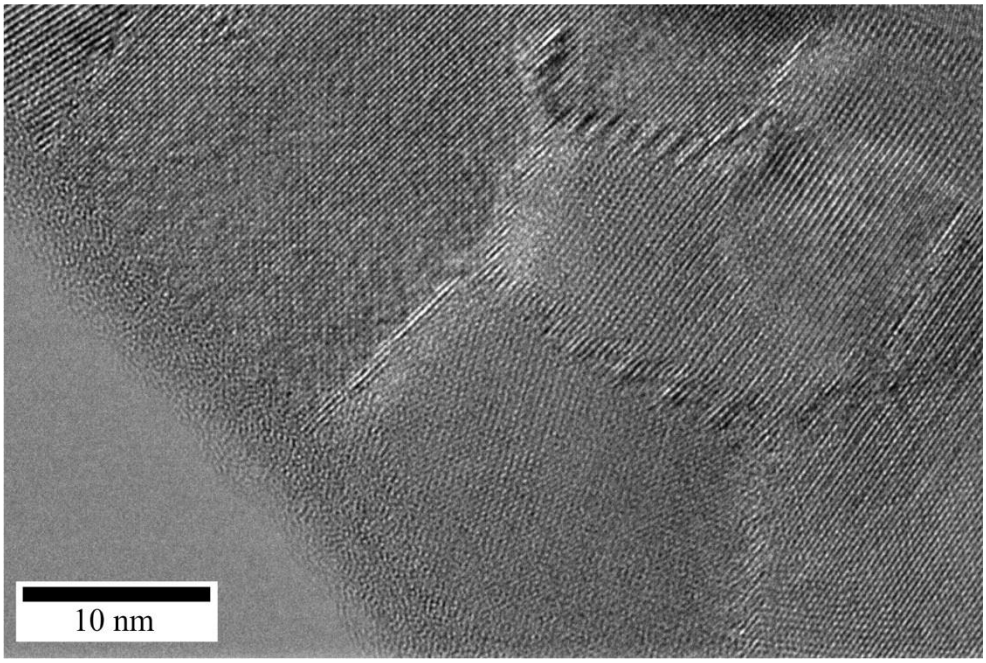


Figure 4.43: HRTEM micrograph of subgrains in KNN-6% Sr-1140.

As was demonstrated by the Rietveld refinement of the synchrotron XRD spectra (Table 4.5) and confirmed by the Raman analysis (Figure 4.34), the microstrain and lattice disorder are increasing with the increasing Sr content. Such disorder would locally cause deformation and eventually would result in the formation of subgrains. Further, the more Sr is introduced, the more the deformed regions are formed, which would be proportional to the number of the formed subgrains. Since the subgrains were found to have only a small misorientation with their neighbours (Figure 4.41b, Figure 4.42), the grain-boundary mobility between two such subgrains is too small for either of the grains to grow.

The existence of the low-angle grain boundaries also additionally explains the peak broadening of the XRD spectra (Figure 4.27b). The XRD detects the average crystal structure of the KNN-6% Sr or KNN-8% Sr as cubic, because the amount of Sr is large enough to have a major impact on the structure in the sample. At the same time, the XRD peak broadening can be related to the presence of lattice imperfections which are demonstrated as low-angle grain boundaries. The disorder related to the low-angle grain boundaries can also be understood as a crystal which is broken into smaller, incoherently diffracting domains and as such result in a broadened diffraction peak.

Figure 4.44 presents another kind of a boundary, which was found in KNN-8% Sr-1140. It is a grain boundary between a secondary phase (Figure 4.44a, left grain) and the perovskite (Figure 4.44a, right grain). The zone axis of both phases is the [001] direction. The grain on the right is a regular perovskite KNN with the cell parameters determined as: a = 0.4147 nm, b = 0.4144 nm, γ = 90.06°. The KNN unit cell was indexed according to the Tellier et al. monoclinic unit cell [32] with arbitrarily selected parameters. The left grain, on the other hand, could be identified as the polyniobate secondary phase with a tetragonal tungsten-bronze structure, which corresponds to the already discussed $K_{5.75}Nb_{10.85}O_{30}$ (ICDD, PDF: 00-038-0297) secondary phase found in the KNN-6% Sr and KNN-8% Sr by XRD (Figure 4.27c) and its composition was verified by TEM-EDXS

(Figure 4.33). The unit-cell parameters of the phase's PDF card are therefore the following: a = b = 1.2579 nm, $\alpha = \beta = \gamma = 90°$, while the measured unit-cell parameters obtained from Figure 4.44 are: a = 1.3120 nm, b = 1.2987 nm, γ = 90.54° (arbitrarily selected). With a closer look, there is a gradual transition between the left and right grains, which is demonstrated in the gradual modification of the structure from a perovskite phase to the tetragonal tungsten bronze (see the insets in Figure 4.44a), unlike in the model of the two neighbouring phases viewed in the [001] direction presented in Figure 4.44b.

The unit-cell parameters determined from the HAADF-STEM ARM micrograph additionally confirm the structure of the secondary phase in the KNN-6% Sr and KNN-8% Sr at the atomic level as the tetragonal tungsten bronze $K_{5.75}Nb_{10.85}O_{30}$. As previously discussed, this phase is formed to compensate for the decreasing A/B ratio in KNN [55, 104]. The gradual structural adaptation of the perovskite phase to the tetragonal tungsten bronze phase (Figure 4.44a, insets) can therefore be related to the gradient of the A-site vacancies, which is increasing with the distance from the perovskite phase. To make this possible, the diffusion of the A-site vacancies must be employed so the doped system can release the chemical pressure in the perovskite structure, as discussed in the results from the Raman spectroscopy (Figure 4.34) and compensate for the defects caused by doping.

The compensation of Sr together with the A-site vacancies, which are introduced based on the samples formula, is different in the samples with the Sr content up to 2% and above. In the samples up to 2% Sr, the A-site vacancies and Sr atoms would be adapted in the perovskite structure. The fact that the samples up to 2% Sr are single phase perovskites and the A-site vacancies are not concentrated in isolated areas to form a secondary phase, gives additional proof of the initially assumed existence of the A-site vacancies as point defects, likely associated with the Sr atoms in the structure. Above 2% Sr, secondary phase formation to compensate the introduced A-site vacancies would be favourable. As was discussed above, Sr was not found to be segregated in a separate phase, neither was it detected in the polyniobate secondary phase with a tetragonal tungsten-bronze structure. Based on the changing cell parameters (Table 4.4), Sr also builds in the perovskite lattice for the KNN samples with 6 and 8% Sr, which were not analysed by EXAFS. This explanation fully supports the presence of the increasing lattice disorder and microstrain (Table 4.5), and thus the formation of the low-angle grain boundaries (Figure 4.41 and Figure 4.42) or fine grains (Figure 4.29) in the KNN samples with 6 and 8% Sr.

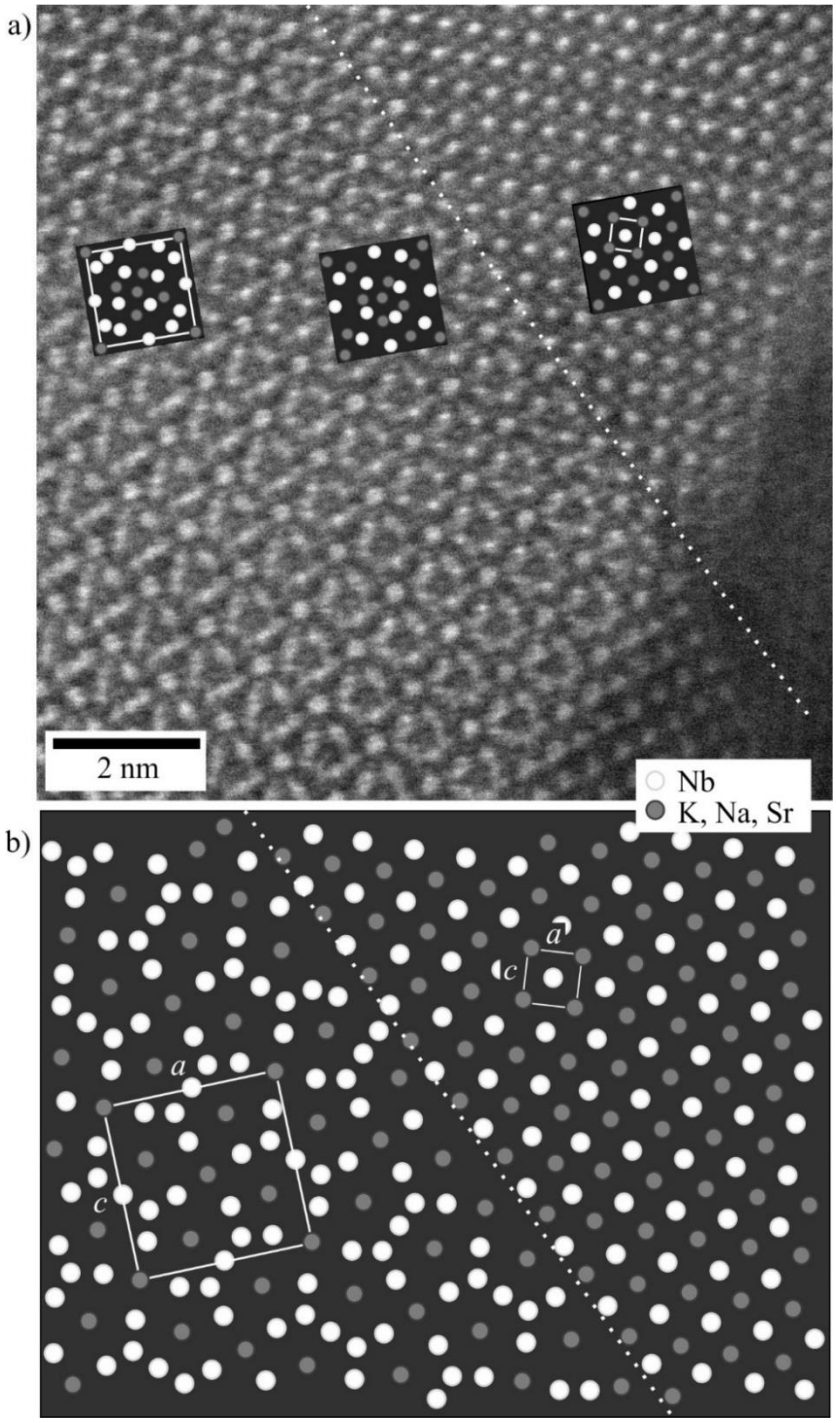


Figure 4.44: ARM study of a grain boundary in KNN-8% Sr-1140 a) HAADF-STEM image showing a grain-boundary region between the grain of a secondary phase (left) and a perovskite grain (right). Atoms with the brightest contrast correspond to Nb, while the darker contrast is attributed to the A-site atoms, i.e., K, Na or Sr. For better visibility, the insets present the re-drawn structures at different distances from the grain boundary. b) A structural model of both the secondary phase (left) and a perovskite phase (right) with marked unit cells. The grain boundary between the phases is marked with a dotted white line.

Chapter 5

Summary and Conclusions

This work addresses the reproducibility of KNN solid-state synthesis, the influence of the Sr dopant on the solid-state synthesis of KNN and the effect of Sr on the final ceramics' microstructure and crystal structure.

5.1 The Influence of the Niobium Pentoxide Reagent on the KNN Solid-State Synthesis and Sintering

In the first part of this thesis, the influence of the niobium pentoxide polymorphic form on the solid-state synthesis and sintering of the potassium sodium niobate solid solution was investigated.

Two batches of KNN were prepared by solid-state synthesis at 800°C, using milled orthorhombic and milled monoclinic Nb_2O_5. After milling, the granulometric analysis, specific surface area measurement and morphology analysis by SEM confirmed the comparable particle-size distributions of both of the Nb_2O_5 reagents. However, XRD and HRTEM analyses of the monoclinic Nb_2O_5 revealed that milling caused a transformation of 47% of the monoclinic Nb_2O_5 to its orthorhombic polymorph and that the newly introduced orthorhombic phase was present in the form of nanocrystals attached to the surface of larger, micron-sized monoclinic Nb_2O_5 particles.

The milled orthorhombic Nb_2O_5 reacted with the potassium and sodium carbonates to form a stoichiometric $K_{0.5}Na_{0.5}NbO_3$. On the other hand, the milled monoclinic Nb_2O_5 reacted with carbonates to form an inhomogeneous mixture of solid solutions with the varying Na:K ratios. This powder could be homogenized by additional annealing at 950°C.

The starting A-site inhomogeneity of the KNN powder prepared from the milled monoclinic Nb_2O_5 significantly influenced its sintering behaviour and sintering at 1120°C resulted in mechanically unstable ceramics with extremely large grains. The sintering of the powder additionally homogenized at 950°C under the same conditions resulted in ceramics with a uniform grain size; however, the high-temperature annealing caused particle coarsening and consequently decreased the sinterability as compared to the finer KNN powder, obtained from the milled orthorhombic Nb_2O_5.

This study shows that the starting particle size distribution and polymorphic form of the as-received Nb_2O_5 reagents play a crucial role in determining the A-site homogeneity of the potassium sodium niobate solid solution. This point is important for achieving a higher reproducibility of the KNN processing.

5.2 Study of the Solid-State Synthesis of KNN Doped by Strontium

In the second part, the solid-state synthesis of KNN and KNN doped with Sr was studied by the TG and DTA complemented with EGA and HT-XRD. The TG, DTA and EGA results showed, that the potassium and sodium carbonates react with the air moisture to form hydrogen carbonates and hydrates during manipulation with the powders. When heated, the decomposition of the formed hydrogen carbonates takes place below 200°C.

During the reaction of the potassium, sodium and strontium carbonates with niobium pentoxide observed in the temperature interval between 200 and 750°C, all the samples exhibit the main mass loss, which is characterized by the evolution of CO_2, in two peaks with the same onset: the first at 400°C and the second at 540°C. The end of the reaction varies, but this was not correlated to the Sr content, but to the differences in the Nb_2O_5 particle size distribution as the main factor influencing the temperature span of the reaction.

The DTA curves are similar for the KNN, KNN-1% Sr and KNN-2% Sr, while the KNN-6% Sr has a modified DTA curve, which could be related to the formation of the secondary phase in this sample.

The perovskite phase was detected by the HT-XRD at 450°C in all the samples, regardless the Sr content. The secondary-phase peaks could be detected by the HT-XRD in KNN-6% Sr at 600°C. Therefore, the only difference in the solid-state synthesis of KNN caused by the Sr doping was found to be the fact, that at above 2% Sr, the secondary phase is formed, which modifies the course of the reaction.

5.3 The Influence of the Sr Doping on the KNN Ceramics

In the third part, the already-reported effects of the Sr dopant on the structure and microstructure were confirmed, i.e., with the increasing amount of Sr, there was a tendency to decrease the monoclinic distortion, the segregation of a secondary phase above 2% Sr and a decrease of the grainsize.

The analysis of KNN-0.5% Sr, KNN-1% Sr and KNN-2% Sr with EXAFS proved that the Sr dopant occupies the perovskite A-sublattice and locally modifies the KNN monoclinic structure to cubic and that Sr is homogenously distributed in the investigated samples. Neither EXAFS, nor TEM found any Sr segregation on the nano level. These samples are confirmed by XRD as single-phase perovskites, while the Raman spectroscopy reveals an increasing effect of the increasing Sr content on the Raman modes associated with the A-site. At the same time, Raman shows an increasing disorder of the NbO_6 octahedra, which is demonstrated as the increasing chemical pressure.

In the samples above 2% Sr, i.e., KNN-6% Sr and KNN-8 % Sr, the chemical pressure is released by forming a potassium-rich polyniobate tungsten-bronze phase, structurally and compositionally similar to $K_{5.75}Nb_{10.85}O_{30}$, as shown by the XRD analysis, EDXS and Raman. The lattice disorder and the microstrain increase significantly in the samples with the secondary phase, as shown by Raman spectroscopy and Rietveld refinement of the synchrotron XRD spectra, respectively.

Introducing Sr into the A-sublattice as well as accounting for the A-site vacancies causes defects in the perovskite lattice, which are compensated for in different ways with the compositions up to 2% Sr and higher. The increasing disorder in the KNN-6% Sr and KNN-8% Sr results in the recrystallization of subgrains with a size of the order of tens of nm, as shown by the TEM studies on the atomic level. The neighbouring subgrains are divided by low-angle grain boundaries, with a strongly limited grain-boundary mobility, which consequently stops the grains from growing. The size of the individual grains thus reduces to the crystallite size in KNN-6% Sr and KNN-8% Sr.

References

[[1] J. Holterman and P. Groen, "Piezoelectricity in everyday life," in *An Introduction to Piezoelectric Materials and Components*, Apeldoorn: Stichting Applied Piezo, 2012.

[2] Acmite Market Intelligence, "Global Piezoelectric Device Market - Market report," 2014.

[3] EU Directive 2002/95/EC, "Waste Electrical and Electronic Equipment (WEEE)," *Official Journal of the European Union*, vol. 46, pp. 24-38, 2003.

[4] EU Directive 2002/95/EC, "Restriction of the Use of Certain Hazardous Substances in electrical and Electronic Equipment (RoHS)," *Official Journal of the European Union*, vol. 46, pp. 19-23, 2003.

[5] J. Rödel, K. G. Webber, R. Dittmer, W. Jo, M. Kimura, and D. Damjanovic, "Transferring lead-free piezoelectric ceramics into application," *Journal of the European Ceramic Society,* vol. 35, pp. 1659-1681, 2015.

[6] Y. Saito, H. Takao, T. Tani, T. Nonoyama, K. Takatori, T. Homma, T. Nagaya, and M. Nakamura, "Lead-free piezoceramics," *Nature,* vol. 432, pp. 84-87, 2004.

[7] B. Jaffe, W. R. Cook, and H. Jaffe, "Piezoelectric properties of (K, Na)NbO_3," The role of defects and diffusion in reaction and sintering," and "Structure of (K, Na)NbO_3 solid solutions," in *Non-metallic solids, Piezoelectric ceramics*, J. P. Roberts and P. Popper, Eds, London: Academic press, 1971.

[8] G. Shirane, R. Newnham, and R. Pepinsky, "Dielectric Properties and Phase Transitions of $NaNbO_3$ and (Na,K)NbO_3," *Physical Review,* vol. 96, pp. 581-588, 1954.

[9] L. Egerton and D. M. Dillon, "Piezoelectric and Dielectric Properties of Ceramics in the System Potassium—Sodium Niobate," *Journal of the American Ceramic Society,* vol. 42, pp. 438-442, 1959.

[10] H. Birol, D. Damjanovic, and N. Setter, "Preparation and characterization of $(K_{0.5}Na_{0.5})NbO_3$ ceramics," *Journal of the European Ceramic Society,* vol. 26, pp. 861-866, 2006.

[11] H. Du, Z. Li, F. Tang, S. Qu, Z. Pei, and W. Zhou, "Preparation and piezoelectric properties of $(K_{0.5}Na_{0.5})NbO_3$ lead-free piezoelectric ceramics with pressure-less sintering," *Materials Science and Engineering: B,* vol. 131, pp. 83-87, 2006.

[12] M. Kosec and D. Kolar, "On activated sintering and electrical properties of $NaKNbO_3$," *Materials Research Bulletin,* vol. 10, pp. 335-339, 1975.

[13] J. Acker, H. Kungl, and M. J. Hoffmann, "Influence of Alkaline and Niobium Excess on Sintering and Microstructure of Sodium-Potassium Niobate ($K_{0.5}$ $Na_{0.5}$)NbO_3," *Journal of the American Ceramic Society,* vol. 93, pp. 1270-1281, 2010.

[14] B. Malic, H. Razpotnik, J. Koruza, S. Kokalj, J. Cilensek, and M. Kosec, "Linear Thermal Expansion of Lead-Free Piezoelectric $K_{0.5}Na_{0.5}NbO_3$ Ceramics in a Wide Temperature Range," *Journal of the American Ceramic Society,* vol. 94, pp. 2273-2275, 2011.

[15] D. Kolar, "Hitrost kemijskih reakcij (kinetika)," in *Tehnična keramika, I. knjiga*, S. Pejovnik and F. Randl, Eds., Ljubljana: Zavod Republike Slovenije za šolstvo in šport, 1993.

[16] B. Malic, D. Jenko, J. Bernard, J. Cilensek, and M. Kosec, "Synthesis and sintering of (K,Na)NbO_3 based ceramics," in *Solid-State Chemistry of Inorganic Materials IV Symposium*, Warrendale, PA, USA, 2003.

[17] J. Pavlič, B. Malič, and T. Rojac, "Microstructural, structural, dielectric and piezoelectric properties of potassium sodium niobate thick films," *Journal of the European Ceramic Society,* vol. 34, pp. 285-295, 2014.

[18] L. K. Templeton and J. A. Pask, "Formation of $BaTiO_3$ from $BaCO_3$ and TiO_2 in Air and in CO_2," *Journal of the American Ceramic Society,* vol. 42, pp. 212-216, 1959.

[19] B. Malic, D. Jenko, J. Holc, M. Hrovat, and M. Kosec, "Synthesis of sodium potassium niobate: A diffusion couples study," *Journal of the American Ceramic Society,* vol. 91, pp. 1916-1922, Jun 2008.

[20] D. Jenko, "Synthesis of (K,Na)NbO_3 Ceramics," PhD thesis, Faculty of Natural Science, University of Ljubljana, Ljubljana, 2006.

[21] A. Safari and M. Hejazi, "Lead-free KNN-based piezoelectric materials," in *Lead-Free Piezoelectrics*, S. Priya and S. Nahm, Eds., New York: Springer, 2012

[22] B. Malič, D. Jenko, M. Starowicz, J. Bernard, and M. Kosec, "Processing and characterization of (K,Na)NbO_3 based piezoceramics," in *International conference on microelectronics, devices and materials,* Lipica, Slovenia, 2002.

[23] S. Tashiro and K. Ishii, "Grain Size and Piezoelectric Properties of (Ba, K, Na)NbO_3 Lead-Free Ceramics," *Journal of the Ceramics Society of Japan,* vol. 114, pp. 386-391, 2006.

[24] M. T. Buscaglia, M. Bassoli, V. Buscaglia, and R. Alessio, "Solid-State Synthesis of Ultrafine $BaTiO_3$ Powders from Nanocrystalline $BaCO_3$ and TiO_2," *Journal of the American Ceramic Society,* vol. 88, pp. 2374-2379, 2005.

[25] E. Hollenstein, M. Davis, D. Damjanovic, and N. Setter, "Piezoelectric properties of Li- and Ta-modified ($K_{0.5}Na_{0.5}$)NbO_3 ceramics," *Applied Physics Letters,* vol. 87, pp. 182905-3, 2005.

[26] F. Holtzberg, A. Reisman, M. Berry, and M. Berkenblit, "Chemistry of the Group VB Pentoxides. VI. The Polymorphism of Nb_2O_5," *Journal of the American Chemical Society,* vol. 79, pp. 2039-2043, 1957.

[27] H. Schäfer, R. Gruehn, and F. Schulte, "Die Modifikationen des Niobpentoxids," *Angewandte Chemie,* vol. 78, pp. 28-41, 1966.

[28] E. Kuznetsova, L. Reznichenko, O. Razumovskaya, and L. Shilkina, "The polymorphism of niobium pentoxide and the properties of alkali metal niobates for ferroelectric piezoceramics," *Technical Physics Letters,* vol. 27, pp. 189-192, 2001.

[29] D. Jenko, A. Bencan, B. Malic, J. Holc, and M. Kosec, "Electron microscopy studies of potassium sodium niobate ceramics," *Microscopy and Microanalysis,* vol. 11, pp. 572-580, 2005.

[30] Y. Zhen and J.-F. Li, "Abnormal Grain Growth and New Core–Shell Structure in (K,Na)NbO_3-Based Lead-Free Piezoelectric Ceramics," *Journal of the American Ceramic Society,* vol. 90, pp. 3496-3502, 2007.

[31] Y. Shiratori, A. Magrez, and C. Pithan, "Particle size effect on the crystal structure symmetry of $K_{0.5}Na_{0.5}NbO_3$," *Journal of the European Ceramic Society,* vol. 25, pp. 2075-2079, 2005.

[32] J. Tellier, B. Malic, B. Dkhil, D. Jenko, J. Cilensek, and M. Kosec, "Crystal structure and phase transitions of sodium potassium niobate perovskites," *Solid State Sciences,* vol. 11, pp. 320-324, 2009.

[33] A. Benčan, E. Tchernychova, M. Godec, J. Fisher, and M. Kosec, "Compositional and Structural Study of a ($K_{0.5}Na_{0.5}$)NbO_3 Single Crystal Prepared by Solid State Crystal Growth," *Microscopy and Microanalysis,* vol. 15, pp. 435-440, 2009.

[34] M. Asif Rafiq, P. Supancic, M. E. Costa, P. M. Vilarinho, and M. Deluca, "Precise determination of phonon constants in lead-free monoclinic ($K_{0.5}Na_{0.5}$)NbO_3 single crystals," *Applied Physics Letters,* vol. 104, p. 011902, 2014.

[35] R. López-Juárez, O. Novelo-Peralta, F. González-García, F. Rubio-Marcos, and M.-E. Villafuerte-Castrejón, "Ferroelectric domain structure of lead-free potassium-sodium

niobate ceramics," *Journal of the European Ceramic Society,* vol. 31, pp. 1861-1864, 2011.

[36] Y. Cao, K. Zhu, H. Zheng, J. Qiu, and H. Gu, "Synthesis of potassium sodium niobate powders using an EDTA/citrate complexing sol–gel method," *Particuology,* vol. 10, pp. 777-782, 2012.

[37] C. Wang, Y.-D. Hou, H.-Y. Ge, M.-K. Zhu, and H. Yan, "Growth of $(Na_{0.5}K_{0.5})NbO_3$ single crystals by abnormal grain growth method from special shaped nano-powders," *Journal of the European Ceramic Society,* vol. 30, pp. 1725-1730, 2010.

[38] J. Attia, L. Bellaiche, P. Gemeiner, B. Dkhil, and B. Malic, "Study of potassium-sodium-niobate alloys: A combined experimental and theoretical approach," *J. Phys. IV France,* vol. 128, pp. 55-60, 2005.

[39] H. J. Trodahl, N. Klein, D. Damjanovic, N. Setter, B. Ludbrook, D. Rytz, and M. Kuball, "Raman spectroscopy of $(K,Na)NbO_3$ and $(K,Na)_{1-x}Li_xNbO_3$," *Applied Physics Letters,* vol. 93, p. 262901, 2008.

[40] D. M. Smyth, "Extrinsic nonstoichiometry," and "Barium titanate," in *The Defect Chemistry of Metal Oxides*, Y. Xi, Ed., Xi 'an Jiatong University Press, 2006.

[41] M. N. Rahaman and R. Manalert, "Grain boundary mobility of $BaTiO_3$ doped with aliovalent cations," *Journal of the European Ceramic Society,* vol. 18, pp. 1063-1071, 1998.

[42] F. D. Morrison, D. C. Sinclair, and A. R. West, "Electrical and structural characteristics of lanthanum-doped barium titanate ceramics," *Journal of Applied Physics,* vol. 86, pp. 6355-6366, 1999.

[43] Z. Valdez-Nava, S. Guillemet-Fritsch, C. Tenailleau, T. Lebey, B. Durand, and J. Y. Chane-Ching, "Colossal dielectric permittivity of $BaTiO_3$-based nanocrystalline ceramics sintered by spark plasma sintering," *Journal of Electroceramics,* vol. 22, pp. 238-244, 2008.

[44] M. Ganguly, S. K. Rout, T. P. Sinha, S. K. Sharma, H. Y. Park, C. W. Ahn, and I. W. Kim, "Characterization and Rietveld Refinement of A-site deficient Lanthanum doped Barium Titanate," *Journal of Alloys and Compounds,* vol. 579, pp. 473-484, 2013.

[45] J.-i. Itoh, D.-C. Park, N. Ohashi, I. Sakaguchi, I. Yashima, H. Haneda and J. Tanaka, "Oxygen Defects Related to Electrical Properties of La-doped $BaTiO_3$," *Japanese Journal of Applied Physics,* vol. 41, p. 3798, 2002.

[46] S. Urek, M. Drofenik, and D. Makovec, "Sintering and properties of highly donor-doped barium titanate ceramics," *Journal of Materials Science,* vol. 35, pp. 895-901, 2000.

[47] D. Hennings and G. Rosenstein, "Temperature-Stable Dielectrics Based on Chemically Inhomogeneous $BaTiO_3$," *Journal of the American Ceramic Society,* vol. 67, pp. 249-254, 1984.

[48] Y. Park and H. G. Kim, "The microstructure analysis of cerium-modified barium titanate having core-shell structured grains," *Ceramics International,* vol. 23, pp. 329-336, 1997.

[49] M. Hammer and M. J. Hoffmann, "Sintering Model for Mixed-Oxide-Derived Lead Zirconate Titanate Ceramics," *Journal of the American Ceramic Society,* vol. 81, pp. 3277-3284, 1998.

[50] Z. Li, G. Xu, Y. Li, A. Sun, L. Duan, J. Jiang, and P.Cui, "Dielectric and piezoelectric properties of ZnO and SnO_2 co-doping $K_{0.5}Na_{0.5}NbO_3$ ceramics," *Physica B: Condensed Matter,* vol. 405, pp. 296-299, 2010.

[51] J. Du, G.-Z. Zang, X.-J. Yi, D.-F. Zhang, and Z.-F. Huang, "Effects of $W_{2/3}Bi_{1/3}$ substitute on piezoelectric properties of KNN-based ceramics," *Materials Letters,* vol. 70, pp. 23-25, 2012.

[52] N. Marandian Hagh, B. Jadidian, and A. Safari, "Property-processing relationship in lead-free (K, Na, Li) NbO_3-solid solution system," *Journal of Electroceramics,* vol. 18, pp. 339-346, 2007.

[53] F. Rubio-Marcos, P. Marchet, T. Merle-Méjean, and J. F. Fernandez, "Role of sintering time, crystalline phases and symmetry in the piezoelectric properties of lead-free KNN-modified ceramics," *Materials Chemistry and Physics,* vol. 123, pp. 91-97, 2010.

[54] S. H. Moon, J. H. Choi, K. W. Chae, J. Seog Kim, and C. I. Cheon, "The effect of pre-annealing on the microstructure of (K,Na)NbO_3 ceramics," *Ceramics International,* vol. 39, pp. 2431-2436, 2013.

[55] Y. Wang, D. Damjanovic, N. Klein, and N. Setter, "High-Temperature Instability of Li- and Ta-Modified (K,Na)NbO_3 Piezoceramics," *Journal of the American Ceramic Society,* vol. 91, pp. 1962-1970, 2008.

[56] Y. Zhen and J.-F. Li, "Normal Sintering of (K,Na)NbO_3-Based Ceramics: Influence of Sintering Temperature on Densification, Microstructure, and Electrical Properties," *Journal of the American Ceramic Society,* vol. 89, pp. 3669-3675, 2006.

[57] M.-S. Kim, D.-S. Lee, E.-C. Park, S.-J. Jeong, and J.-S. Song, "Effect of Na_2O additions on the sinterability and piezoelectric properties of lead-free 95($Na_{0.5}K_{0.5}$)NbO_3–5$LiTaO_3$ ceramics," *Journal of the European Ceramic Society,* vol. 27, pp. 4121-4124, 2007.

[58] J.-F. Li, Y. Zhen, B.-P. Zhang, L.-M. Zhang, and K. Wang, "Normal sintering of (K, Na)NbO_3-based lead-free piezoelectric ceramics," *Ceramics International,* vol. 34, pp. 783-786, 2008.

[59] H. E. Mgbemere, M. Hinterstein, and G. A. Schneider, "Structural phase transitions and electrical properties of (K_xNa_{1-x})NbO_3-based ceramics modified with Mn," *Journal of the European Ceramic Society,* vol. 32, pp. 4341-4352, 2012.

[60] Y. Guo, K.-i. Kakimoto, and H. Ohsato, "Dielectric and piezoelectric properties of lead-free ($Na_{0.5}K_{0.5}$)NbO_3–$SrTiO_3$ ceramics," *Solid State Communications,* vol. 129, pp. 279-284, 2004.

[61] M. U. Farooq and J. G. Fisher, "Growth of ($K_{0.5}Na_{0.5}$)NbO_3–$SrTiO_3$ lead-free piezoelectric single crystals by the solid state crystal growth method and their characterization," *Ceramics International,* vol. 40, pp. 3199-3207, 2014.

[62] A. Kupec and B. Malič, "Structural and dielectric properties of the lead-free (1−x)$K_{0.5}Na_{0.5}NbO_3$–x$SrTiO_3$ thin films from solutions," *Journal of Alloys and Compounds,* vol. 596, pp. 32-38, 2014.

[63] K.-H. Cho, H.-Y. Park, C.-W. Ahn, S. Nahm, K. Uchino, S.-H. Park, H.-G. Lee, and H.-J. Lee, "Microstructure and Piezoelectric Properties of 0.95($Na_{0.5}K_{0.5}$)NbO_3–0.05$SrTiO_3$ Ceramics," *Journal of the American Ceramic Society,* vol. 90, pp. 1946-1949, 2007.

[64] M. Kosec, V. Bobnar, M. Hrovat, J. Bernard, B. Malic, and J. Holc, "New lead-free relaxors based on the $K_{0.5}Na_{0.5}NbO_3$–$SrTiO_3$ solid solution," *Journal of Materials Research,* vol. 19, pp. 1849-1854, 2004.

[65] M. Matsubara, T. Yamaguchi, W. Sakamoto, K. Kikuta, T. Yogo, and S.-i. Hirano, "Processing and Piezoelectric Properties of Lead-Free (K,Na) (Nb,Ta) O_3 Ceramics," *Journal of the American Ceramic Society,* vol. 88, pp. 1190-1196, 2005.

[66] S. Su, R. Zuo, X. Wang, and L. Li, "Sintering, microstructure and piezoelectric properties of CuO and SnO_2 co-modified sodium potassium niobate ceramics," *Materials Research Bulletin,* vol. 45, pp. 124-128, 2010.

[67] H. Takao, Y. Saito, Y. Aoki, and K. Horibuchi, "Microstructural Evolution of Crystalline-Oriented ($K_{0.5}Na_{0.5}$)NbO_3 Piezoelectric Ceramics with a Sintering Aid of CuO," *Journal of the American Ceramic Society,* vol. 89, pp. 1951-1956, 2006.

[68] S.-L. Yang, C.-S. Hong, C.-C. Tsai, Y.-C. Liou, and S.-Y. Chu, "Effects of modified-process on the microstructure, internal bias field, and activation energy in CuO-doped NKN ceramics," *Journal of the European Ceramic Society,* vol. 32, pp. 1643-1650, 2012.

[69] D. Lin, K. W. Kwok, and H. L. W. Chan, "Piezoelectric and ferroelectric properties of $K_xNa_{1-x}NbO_3$ lead-free ceramics with MnO_2 and CuO doping," *Journal of Alloys and Compounds,* vol. 461, pp. 273-278, 2008.

[70] I.-Y. Kang, I.-T. Seo, Y.-J. Cha, J.-H. Choi, S. Nahm, T.-H. Sung, and J.-H. Paik, "Low temperature sintering of ZnO and MnO_2-added $(Na_{0.5}K_{0.5})NbO_3$ ceramics," *Journal of the European Ceramic Society,* vol. 32, pp. 2381-2387, 2012.

[71] S.-H. Park, C.-W. Ahn, S. Nahm, and J.-S. Song, "Microstructure and Piezoelectric Properties of ZnO-added $(Na_{0.5}K_{0.5})NbO_3$ Ceramics," *Japanese Journal of Applied Physics,* vol. 43, p. L1072, 2004.

[72] R. Zuo, J. Rödel, R. Chen, and L. Li, "Sintering and Electrical Properties of Lead-Free $Na_{0.5}K_{0.5}NbO_3$ Piezoelectric Ceramics," *Journal of the American Ceramic Society,* vol. 89, pp. 2010-2015, 2006.

[73] X. Vendrell, J. E. García, X. Bril, D. A. Ochoa, L. Mestres, and G. Dezanneau, "Improving the functional properties of $(K_{0.5}Na_{0.5})NbO_3$ piezoceramics by acceptor doping," *Journal of the European Ceramic Society,* vol. 35, pp. 125-130, 2015.

[74] J. Rani, P. K. Patel, N. Adhlakha, H. Singh, K. L. Yadav, and S. Prakash, "Mo6+ Modified $(K_{0.5}Na_{0.5})NbO_3$ Lead Free Ceramics: Structural, Electrical and Optical Properties," *Journal of Materials Science & Technology,* vol. 30, pp. 459-465, 2014.

[75] K.-i. Kakimoto, K. Akao, Y. Guo, and H. Ohsato, "Raman Scattering Study of Piezoelectric $(Na_{0.5}K_{0.5})NbO_3$ -$LiNbO_3$ Ceramics," *Japanese Journal of Applied Physics,* vol. 44, p. 7064, 2005.

[76] B. Malic, J. Bernard, J. Holc, D. Jenko, and M. Kosec, "Alkaline-earth doping in $(K,Na)NbO_3$ based piezoceramics," *Journal of the European Ceramic Society,* vol. 25, pp. 2707-2711, 2005.

[77] B. Malic, J. Bernard, J. Holc, and M. Kosec, "Strontium doped $K_{0.5}Na_{0.5}NbO_3$ based piezoceramics," *Ferroelectrics,* vol. 314, pp. 149-156, 2005.

[78] R. D. Shannon, "Revised effective ionic radii and systematic studies of interatomic distances in halides and chalcogenides," *Acta Crystallographica Section A,* vol. 32, pp. 751-767, 1976.

[79] M. D. Maeder, D. Damjanovic, and N. Setter, "Lead Free Piezoelectric Materials," *Journal of Electroceramics,* vol. 13, pp. 385-392, 2004.

[80] S. J. Reed, "Density, pore structure, and specific surface area," in *Principles of Ceramics Processing, 2nd Edition*: Wiley-Interscience, 1995.

[81] V. Petříček, M. Dušek, and L. Palatinus, "Crystallographic Computing System JANA2006: General features," *Zeitschrift für Kristallographie - Crystalline Materials,* vol. 229, pp. 345-352, 2014.

[82] M. Ferrari and L. Lutterotti, "Method for the simultaneous determination of anisotropic residual stresses and texture by x-ray diffraction," *Journal of Applied Physics,* vol. 76, pp. 7246-7255, 1994.

[83] B. Ravel and M. Newville, "ATHENA, ARTEMIS, HEPHAESTUS: data analysis for X-ray absorption spectroscopy using IFEFFIT," *Journal of Synchrotron Radiation,* vol. 12, pp. 537-541, 2005.

[84] J. J. Rehr, J. Mustre de Leon, S. I. Zabinsky, and R. C. Albers, "Theoretical x-ray absorption fine structure standards," *Journal of the American Chemical Society,* vol. 113, pp. 5135-5140, 1991.

[85] D. Wilcox, B. Dove, D. McDavid, and D. Greer, "Image Tool for Windows," Version 3.0 ed. San Antonio: University of Texas Health Science Center, 2002.

[86] L. K. Frevel and H. W. Rinn, "Powder Diffraction Standards for Niobium Pentoxide and Tantalum Pentoxide," *Analytical Chemistry,* vol. 27, pp. 1329-1330, 1955.

[87] T. Rojac, "Mehanokemijska sinteza $NaNbO_3$," PhD thesis, Fakulteta za kemijo in kemijsko tehnologijo, Univerza v Ljubljani, Ljubljana, 2007.

[88] M. Senna and H. Kuno, "Polymorphic Transformation of PbO by Isothermal Wet Ball-Milling," *Journal of the American Ceramic Society,* vol. 54, pp. 259-262, 1971.

[89] S. S. Chandratreya, R. M. Fulrath, and J. A. Pask, "Reaction Mechanisms in the Formation of PZT Solid Solutions," *Journal of the American Ceramic Society,* vol. 64, pp. 422-425, 1981.

[90] B. Malic, J. Bernard, A. Bencan, and M. Kosec, "Influence of zirconia addition on the microstructure of $K_{0.5}Na_{0.5}NbO_3$ ceramics," *Journal of the European Ceramic Society,* vol. 28, pp. 1191-1196, 2008.

[91] J. A. Hedvall, *Solid state chemistry. Whence, where and whither*. Amsterdam: Elsevier, 1966.

[92] P. D. Garn and T. S. Habash, "Solid state reactions. A rigorous test of the Hedvall effect," *The Journal of Physical Chemistry,* vol. 83, pp. 229-231, 1979.

[93] P. K. Gallagher and D. W. Johnson, "Solid-state reactivity in the system sodium carbonate-calcium carbonate," *The Journal of Physical Chemistry,* vol. 86, pp. 295-297, 1982.

[94] C. Herring, "Some Theorems on the Free Energies of Crystal Surfaces," *Physical Review,* vol. 82, pp. 87-93, 1951.

[95] M. Kosec, B. Malič, A. Benčan, and T. Rojac, "KNN-Based Piezoelectric Ceramics" in *Piezoelectric and acoustic materials for transducer applications*, A. Safari and E. K. Akdogan, Eds., New York: Springer, 2008.

[96] G. Liptay, *Atlas of thermoanalytical curves*. Budapest: Akademiai Kiado, 1974.

[97] R. Jenkins, *Introduction to X-ray Powder Diffractometry* vol. 138: John Willey & Sons, Inc., 1996.

[98] C. A. Randall, N. Kim, J.-P. Kucera, W. Cao, and T. R. Shrout, "Intrinsic and Extrinsic Size Effects in Fine-Grained Morphotropic-Phase-Boundary Lead Zirconate Titanate Ceramics," *Journal of the American Ceramic Society,* vol. 81, pp. 677-688, 1998.

[99] Z. S. Ahn and W. A. Schulze, "Conventionally Sintered $(Na_{0.5},K_{0.5})NbO_3$ with Barium Additions," *Journal of the American Ceramic Society,* vol. 70, pp. C-18-C-21, 1987.

[100] S. Pin, F. Piccinelli, K. Upendra Kumar, S. Enzo, P. Ghigna, C. Cannas, A. Musinu, G. Mariotto, M. Bettinelli, and A. Speghini, "Structural investigation and luminescence of nanocrystalline lanthanide doped $NaNbO_3$ and $Na_{0.5}K_{0.5}NbO_3$," *Journal of Solid State Chemistry,* vol. 196, pp. 1-10, 2012.

[101] D. C. Harris and M. D. Bertolucci, *Symmetry and Spectroscopy: An Introduction to Vibrational and Electronic Spectroscopy*: Dover Publications, 1978.

[102] A. Glazer, "VIBRATE! A program to compute irreducible representations for atomic vibrations in crystals," *Journal of Applied Crystallography,* vol. 42, pp. 1194-1196, 2009.

[103] N. Klein, E. Hollenstein, D. Damjanovic, H. J. Trodahl, N. Setter, and M. Kuball, "A study of the phase diagram of $(K,Na,Li)NbO_3$ determined by dielectric and piezoelectric measurements, and Raman spectroscopy," *Journal of Applied Physics,* vol. 102, pp. 1-8, 2007.

[104] R. H. Mitchell, "Non-stoichiometric perovskites: A-site vacant and oxygen defect structures," in *Perovskites: modern and ancient*. Almaz Press - Thunder Bay, 2002.

[105] B. Hessen, S. A. Sunshine, T. Siegrist, and R. Jimenez, "Crystallization of reduced strontium and barium niobate perovskites from borate fluxes," *Materials Research Bulletin,* vol. 26, pp. 85-90, 1991.

[106] A. Kodre, J. Tellier, I. Arčon, B. Malič, and M. Kosec, "Extended x-ray absorption fine structure study of phase transitions in the piezoelectric perovskite $K_{0.5}Na_{0.5}NbO_3$," *Journal of Applied Physics,* vol. 105, p. 113528, 2009.

[107] J. Goldstein, D. Newbury, D. Joy, C. Lyman, P. Echlin, E. Lifshin, L. Sawyer, and J. Michael, "X-ray spectral measurement: EDS and WDS," in *Scanning electron Microscopy and X-ray Microanalysis, Third edition*. New York: Kluwer academic/Plenum Publishers, 2003.

[108] R. D. Doherty, D. A. Hughes, F. J. Humphreys, J. J. Jonas, D. J. Jensen, M. E. Kassner, W. E. King, T. R. McNelley, H. J. McQueen, and A. D. Rollett, "Current issues in

recrystallization: a review," *Materials Science and Engineering: A,* vol. 238, pp. 219-274, 1997.

[109] W. D. Kingery, H. K. Bowen, and D. R. Uhlmann, "Grain growth, sintering, and vitrification," in *Introduction of Ceramics, Second Edition*, New york: John Wiley & Sons, 1976.

Bibliography

Journal articles

J. Hreščak, A. Benčan, T. Rojac and B. Malič, "The influence of different niobium pentoxide precursors on the solid-state synthesis of potassium sodium niobate," *Journal of the European ceramic society*, vol. 33, no. 15-16, pp. 3065-3075, 2013.

B. Malič, J. Koruza, J. Hreščak, J, Bernard, K. Wang, J.G. Fisher, A. Benčan, "Sintering of lead-free piezoelectric sodium potassium niobate ceramics," *Materials*, vol. 8, no. 2, pp. 8117-8146, 2015.

Published scientific conference contributions

J. Hreščak, A. Benčan, T. Rojac, B. Malič, "The role of different niobium pentoxide precursors in the solid-state synthesis of potassium sodium niobate," in the *Proceedings of 6th Jožef Stefan International Postgraduate School Students' Conference*, pp. 236-245, Ljubljana, Slovenia: Mednarodna podiplomska šola Jožefa Stefana, 2014.

Published scientific conference contributions - invited talks

B. Malič, J. Hreščak, J. Pavlič, A. Benčan, T. Rojac, "Tailoring the properties of sodium potassium niobate lead-free piezoceramics in bulk and film forms," in *5th International Congress on Ceramics*, Beijing, China, 2014.

B. Malič, J. Koruza, J. Hreščak, J. Bernard, G. Dražić, A. Benčan, "How to understand sintering of sodium potassium niobate ceramics?," in *Electronic Materials and Applications 2016*, Orlando, FL, USA, The American Ceramic Society, 2016

A. Benčan, J. Walker, J. Hreščak, G. Trefalt, J. Jouin, J. Pavlič, Y. Seo, K. Webber, J. Rodel, G. Dražić, D. Damjanović, T. Rojac, B. Malič, "The role of characterization in processing of electro-ceramics from precursor powders to final products," in *Tokyo Institute of Technology*, Tokyo, Japan, 2014.

A. Benčan, J. Hreščak, T. Rojac, H. Uršič, J. Walker, M. Makarovič, G. Dražić, B. Malič, "Insights into the structure of lead-free piezoelectrics in atomic scale," in *Sastanak ekcije za keramiku Sprskog hemijskoh društva 2015*, Beograd, Srbija, 2015.

Published Scientific Conference Contributions – abstracts

J. Hreščak, J. Koruza, A. Benčan, M. Kosec, "Synthesis, sintering and characterisation of strontium doped $K_{0.5}Na_{0.5}NbO_3$ ceramics," in *The Ninth Students' Meeting and Application of Ceramics, and The Second Early Stage Researchers Workshop, COST MP0904*, Novi Sad, Serbia, Faculty of Technology, University of Novi Sad, 2011.

J. Hreščak, A. Benčan, T. Rojac, B. Malič, M. Kosec, "The influence of addition of strontium to $K_{0.5}Na_{0.5}NbO_3$ ceramics," in *Electroceramics XIII*, Enschede, The Netherlands, University of Twente, Twente, The Netherlands, 2012.

A. Benčan, J. Hreščak, B. Malič, M. Kosec, "Structural and microstructural analysis of $K_{0.5}Na_{0.5}NbO_3$ ceramics doped with strontium," in *Microscopy & Microanalysis 2012, 70th Annual Meeting of the Microscopy Society of America, 46th Annual Meeting of the Microanalysis Society, 45th Annual Meeting of the International Metallographic Society*, Phoenix, Arizona, USA, Microscopy and microanalysis, 2012.

J. Hreščak, A. Benčan, B. Malič, T. Rojac, M. Kosec, "Influence of the different Nb2O5 polymorphs on the solid state synthesis and sintering of $K_{0.5}Na_{0.5}NbO_3$," in *Slovenski kemijski dnevi 2012*, Portorož, Slovenia, FKKT, Maribor, 2012

J. Hreščak, A. Benčan, T. Rojac, B. Malič, "The influence of the polymorphic form of niobium pentoxide on the solid-state synthesis of potassium sodium niobate," in *4th Edition of Electroceramics Conference*, Bucharest, Romania, 2014

J. Hreščak, B. Malič, A. Benčan, "Compositional and structural analysis of the Sr-doped $K_{0.5}Na_{0.5}NbO_3$ lead-free ceramics," in *AdSTEM 2014, European Workshop on Quantitative STEM Imaging, EELS and EDXS*, Piran, Slovenia. Department for Nanostructured Materials, Jožef Stefan Institute, Ljubljana, Slovenia, 2014.

J. Hreščak, A. Benčan, T. Rojac, B. Malič, "The role of the niobium pentoxide precursor in the solid-state synthesis of potassium sodium niobate," in *8th Young Researchers' Day*, Ljubljana, Slovenia, Institut Jožef Stefan, Ljubljana, Slovenia, 2014

J. Hreščak, T. Rojac, B. Malič, A. Benčan, "The role of the niobium pentoxide precursor in the homogeneity and densification of the potassium sodium niobate lead-free ceramics," in *22. mednarodna konferenca o materialih in tehnologijah*, Portorož, Slovenija. Inštitut za kovinske materiale in tehnologije, Ljubljana, Slovenia, 2014.

J. Hreščak, J. Walker, G. Dražić, D.O. Alikin, A.P. Turygin, T. Rojac, B. Malič, V. Ya. Shur, A.L. Kholkin, A. Benčan, "Domain structure investigation in Sr-doped potassium sodium niobate lead-free piezoelectric ceramics," in *IEEE International Symposium on Applications of Ferroelectric, International Symposium on Integrated Functionalities and Piezoresponse Force Microscopy Workshop*, Singapore, 2015.

J. Hreščak, M. Deluca, I. Arčon, A. Kodre, T. Rojac, B. Malič, A. Benčan, "Influence of Sr addition on the structure and compositin of $K_{0.5}Na_{0.5}NbO_3$," in *9th Young researchers' day*, Ljubljana, Slovenia, Institut Jožef Stefan, Ljubljana, Slovenia, 2015.

A.P. Turygin, D. Alikin, D. Chezganov, J. Hreščak, J. Walker, T. Rojac, V. Ya. Shur, A.L. Kholkin, "Investigation of lead free ferroelectric ceramics by electron backscattered diffraction & piezoresponse force microscopy," in *12th Multinational Congress on Microscopy*, Eger, Hungary, 2015

J. Hreščak, J. Cilenšek, B. Malič, A. Benčan, "The effect of strontium doping on solid-state synthesis of $K_{0.5}Na_{0.5}NbO_3$ studied by thermal analysis and hightemperature X-ray diffraction," in *3rd Central and Eastern European Conference on Thermal Analysis and Calorimetry*, Ljubljana, Slovenia, Central and Eastern European Committee for Thermal Analysis and Calorimetry, 2015.

A.P. Turygin, D.O. Alikin, D.S. Chezganov, D.V. Zayats, J. Hreščak, J. Walker, G. Dražić, T. Rojac, B. Malič, V.Ya. Shur, A.L. Kholkin, A. Benčan, "Domain structures and local switching in Sr-doped potassium sodium niobate lead-free piezoelectric ceramics," in *13th International Symposium on Electric and Magnetic Fields*, Porto, Portugal, 2015.

D. Alikin, A.P. Turygin, J. Hreščak, J. Walker, D.V. Zayats, V. Ya. Shur, A.L. Kholkin, "Domain study in Sr-doped potassium sodium niobate lead-free piezoelectric ceramics," in *Modern Nanotechnology International Workshop*, Ekaterburg, Russia, 2015

J. Hreščak, M. Deluca, I. Arčon, A. Kodre, T. Rojac, B. Malič, A. Benčan, "Influence of strontium addition on the structure and composition of $K_{0.5}Na_{0.5}NbO_3$ ceramics in *Piezo 2015: Electroceramics for End-Users VIII*, Maribor, Slovenia, 2015